DEVELOPMENT OF A MULTILAYERED SKIN MODEL USING 3D PRINTING AND MICROFLUIDIC SYSTEMS

A THESIS SUBMITTED TO
THE GRADUATE SCHOOL OF NATURAL AND APPLIED SCIENCES
OF
MIDDLE EAST TECHNICAL UNIVERSITY

BY

FUNDA CAN

IN PARTIAL FULFILLMENT OF THE REQUIREMENTS
FOR
THE DEGREE OF MASTER OF SCIENCE
IN
BIOTECHNOLOGY

SEPTEMBER 2021

Approval of the thesis:

DEVELOPMENT OF A MULTILAYERED SKIN MODEL USING 3D PRINTING AND MICROFLUIDIC SYSTEMS

submitted by **FUNDA CAN** in partial fulfillment of the requirements for the degree of **Master of Science** i**n Biotechnology, Middle East Technical University** by,

Prof. Dr. Halil Kalıpçılar
Dean, Graduate School of **Natural and Applied Sciences** _____

Prof. Dr. Candan Gürakan
Head of the Department, **Biotechnology** _____

Prof. Dr. Ayşen Tezcaner
Supervisor, **Engineering Sciences, METU** _____

Dr. Menekşe Ermiş Şen
Co-Supervisor, **Center of Excellence in Biomaterials and Tissue Engineering, METU** _____

Examining Committee Members:

Prof. Dr. Vasıf Hasırcı
Medical Engineering, Acıbadem Mehmet Ali Aydınlar University _____

Prof. Dr. Ayşen Tezcaner
Engineering Sciences, METU _____

Assoc. Prof. Dr. Pınar Yılgör Huri
Biomedical Engineering, Ankara University _____

Assoc. Prof. Dr. İrem Erel Göktepe
Chemistry, METU. _____

Assoc. Prof. Dr. Çağdaş Devrim Son
Biological Sciences, METU _____

Date: 10.09.2021

I hereby declare that all information in this document has been obtained and presented in accordance with academic rules and ethical conduct. I also declare that, as required by these rules and conduct, I have fully cited and referenced all material and results that are not original to this work.

Name Last name : Funda Can

Signature :

ABSTRACT

DEVELOPMENT OF A MULTILAYERED SKIN MODEL USING 3D PRINTING AND MICROFLUIDIC SYSTEMS

Can, Funda
Master of Science, Biotechnology
Supervisor : Prof. Dr. Ayşen Tezcaner
Co-Supervisor: Dr. Menekşe Ermiş Şen

September 2021, 186 pages

This study aims to develop an *in vitro* tri-layered (epidermis, dermis, and hypodermis) skin model by combining 3D printing and microfluidics approaches for a high-throughput drug screening system for skin penetration tests and also develop a bioink that can be printed at room temperature. Human keratinocytes (KC) were seeded on 3D printed poly-lactide-caprolactone (PLC) scaffolds for epidermis fabrication. For dermis, mesenchymal stem cells (ADSC): human dermal fibroblasts (DF) (1:3); and for hypodermis, adipocytes predifferentiated from ADSC: DF (3:1) were loaded to GelMA polymer solution solutions, 3D printed, and UV crosslinked. Air-liquid interface (ALI) culturing was used for keratinocyte stratification of the epidermis layer and characterized in vitro by E-cadherin cell adhesion markers. The stemness of ADSCs was shown by CD105 positivity. Cocultures were established and brought together in a microbioreactor for a dynamic culture setup. Cell viability in dynamic culture was similar to static culture results. The penetration assay using dexamethasone-fluorescein isothiocyanate (Dex-FITC) was performed on a tri-layered, two-layered (dermis

and hypodermis), and also cell-free constructs on a skin-on-a-chip model. The epidermis layer provided drug penetration delay in 3-layered chips. Dex was shown to be taken up by cells within an hour and released for another hour. Results indicated that our microbioreactor system can be used for an advanced drug penetration assay.

In the second part of the thesis, a bioink composed of methacrylated hyaluronic acid (HAMA), alginate, GelMA and IrgaCure developed and successfully printed without cooling. Prepolymer solution was ionically pre-crosslinked with calcium chloride (CaCl2), printed, photocrosslinked, then post-crosslinked with CaCl2 solution. The final hydrogel was a tunable viscoelastic interpenetrating network composed of CaCl2 crosslinked alginate and photocrosslinked HAMA-GelMA. All cell types showed good viability in the bioprints..

Keywords: Skin, 3D Printing, *In Vitro* Skin Model, Microfluidics Device

ÖZ

3 BOYUTLU YAZICI VE MİKROAKIŞKAN CİHAZ KULLANILARAK ÇOK KATLI DERİ MODELİ GELİŞTİRİLMESİ

Can, Funda
Yüksek Lisans, Biyoteknoloji
Tez Yöneticisi: Prof. Dr. Ayşen Tezcaner
Ortak Tez Yöneticisi: Dr. Menekşe Ermiş Şen

Eylül 2021, 186 sayfa

Bu çalışma, cilt penetrasyon testleri için yüksek verimli bir ilaç tarama sistemi için, 3D baskı ve mikroakışkan yaklaşımlarını birleştirerek in vitro üç katmanlı (epidermis, dermis ve hipodermis) bir cilt modeli geliştirmeyi ve aynı zamanda baskı yapılabilen bir biyomürekkep geliştirmeyi ve ayrıca oda sıcaklığında basılabilen bir biyomürekkep geliştirmeyi amaçlamaktadır. İnsan keratinositleri (KC), epidermis üretimi için 3D baskılı poli-laktid-kaprolakton (PLC) iskelelerine ekildi. Dermis için mezenkimal kök hücreler (ADSC): insan dermal fibroblastları (DF) (1:3); ve hipodermis için, önceden farklılaştırılmış adiposit ADSC: DF'den (3:1) GelMA polimer çözeltisine eklendi, 3D basıldı ve UV çapraz bağlandı. Epidermis tabakasının keratinosit tabakalaşması için hava-sıvı arayüzü (ALI) kültürü kullanıldı ve in vitro olarak E-cadherin hücre yapışma belirteçleri ile karakterize edildi. ADSC'lerin kök hücreliliği, CD105 pozitifliği ile gösterilmiştir. Dinamik kültür için kokültürler, mikrobiyoreaktörde ortamında bir araya getirilmiştir. Dinamik kültürdeki hücre canlılığı, statik kültür sonuçlarına benzer olduğu görülmüştür. Deksametazon-floresan izotiyosiyanat (Dex-FITC) kullanılarak penetrasyon çalışması üç katmanlı, iki katmanlı (dermis ve

hipodermis) ve ayrıca hücresiz çip üstü deri üzerinde gerçekleştirildi. Epidermis tabakası, 3 katmanlı çiplerde ilaç penetrasyonunun gecikmesini sağlamıştır. Dex'in hücreler tarafından bir saat içinde alındığı ve bir saat sonra da serbest bırakıldığı gösterildi. Sonuçlar, mikrobiyoreaktör sistemimizin gelişmiş bir ilaç penetrasyon testi için kullanılabileceğini gösterdi.

Tezin ikinci bölümünde, soğutmadan metakrilatlanmış hyaluronik asit (HAMA), aljinat, GelMA, IrgaCure'den oluşan bir biyomürekkep geliştirilmiş ve başarıyla basılmıştır. Jel öncüsü çözelti, basım öncesi kalsiyum klorür ($CaCl_2$) ile iyonik olarak çapraz bağlandı, yazdırıldı, foto çapraz bağlandı, ardından $CaCl_2$ çözeltisi ile basım sonrası çapraz bağlandı. Nihai hidrojel, $CaCl_2$ çapraz bağlı aljinat ve foto çapraz bağlı HAMA-GelMA'dan oluşan ayarlanabilir bir viskoelastik iç içe geçen ağdır. Biyobasımlarda tüm hücre tipleri iyi bir canlılık gösterdi.

Anahtar Kelimeler: Deri, 3B Yazıcı, *In Vitro* Doku Modeli, Mikroakışkan Cihaz

To my beloved family

ACKNOWLEDGMENTS

I want to express gratitude to my supervisor Prof. Dr. Ayşen Tezcaner for guiding the research process, teach the finer details of literature reviewing and show the ways to interpret results. Most importantly, author would like to thank her supervisor for actively listening, carefully and detailed reading, constant morale support and encouragement throughout the process.

I could not thank my co-advisor Dr. Menekşe Ermiş Şen enough for the support for all these years. I could not and would not do it without her. I was very lucky to be the first student of this enthusiast, helpful and understanding scientist. She tirelessly taught me the ways of science and life. Her constructive criticism, encourage to do more and brilliant insight through the research influence me to become the best version of myself and even exceed myself. Without any doubt, her influence on me will last through the years.

I would also like to thank Prof. Dr. Vasıf Hasırcı for his valuable suggestions and comments. His appreciation of hard work, arousing curiosity, endless support, and providing good opportunities significantly contributed to this dissertation and me. I will carry and use those “gold bracelets” wisely.

The friendship and assistance of BIOMATEN members Dr. Ezgi Antmen, Dr. Tuğba Dursun Usual, Dr. Cemile Bektas, Dr. Gozde Eke, Dilara Tamay, Damla Arslantunalı, Dr. Aylin Kömez, Dr. Ali Deniz Dalgıç, Muazzez Ayça Tuncel and Ahmet Engin Pazarçeviren are gratefully acknowledged. Each of them helped me through this journey and has a special place in me.

I am deeply thankful to my partner Egemen Gurallar for sharing all the burden for many years with me and truly be present for me in all good and bad days. His endless love and support made even the most troubling days seem the best day of my life. I am grateful to him for bringing peace and delight into my life.

My special thank is to Dr. Volkan Gülüm. He taught me the balance in life and valuing what is important. The crossing of our paths may be my biggest luck. Everything I am grateful to have now is because of you. You showed me how you can change someone's life completely in a good way by doing the job you love, and I took you as a role model to myself at this.

I want to heartfully thank to my friends Korel Erben, Ali Değermenci and Dilara Savur, Sajida Khalid and Arzu. I am lucky to have such supporting friends who became my family by the time. The times I lost my motivation, they were always believing in me. Also, can't skip thanking Elbakyan for her efforts.

I would want to express my deepest gratitude to my parents Metin Can and Ezel Can. Having them is my biggest blessing in life. Knowing that they will always stand behind me, encourage me to achieve anything I could imagine.

I want to thank BIOMATEN for providing all the tools to become a skilled researcher in the biomaterials field. The opportunities I get there were very valuable for me.

This work is partially funded by Scientific and Technological Research Council of Turkey under grant number TUBİTAK 2210-C.

TABLE OF CONTENTS

LIST OF TABLES

TABLES

LIST OF FIGURES

FIGURES

LIST OF ABBREVIATIONS

ABBREVIATIONS

2D	Two-dimensional
3D	Three-dimensional
ADSCs	Adipose-derived mesenchymal stem cells
ALI	Air-liquid interface
CAD	Computer-aided design
CFD	Computational fluid dynamics
CLSM	Confocal laser scanning microscope
DAPI	4′,6-diamidino-2-phenylindole,
DEX	Dexamethasone
DF	Human dermal fibroblasts
dH_2O	Distilled water
DM	Degree of methacrylation
DMF	Dimethylformamide
DSA	Double-sided adhesive
DSC	Differential scanning calorimetry
ECs	Endothelial cells
ESEM	Environmental scanning electron microscope
EtOH	Ethanol
FBS	Fetal Bovine Serum

FDA	US Food and Drug Administration
FITC-DEX	Fluorescein isothiocyanate conjugated dexamethasone
FTIR	Fourier-transform infrared spectroscopy
G′	Elastic modulus
G″	Shear loss modulus
GelMA	Gelatin methacrylate
HA	Hyaluronic acid
HAMA	Methacrylated hyaluronic acid
HDMECs	Human dermal microvascular endothelial cells
hiNSCs	Human-induced neural stem cells
HUVEC	Human umbilical vein endothelial cells
ID14	Initially differentiated for 14 days
ID7	Initially differentiated for 7 days
IL-2	Interleukin-2
IPSCs	Induced pluripotent stem cells
Irgacure	Photoinitiator 2-hydroxy-4’-hydroxyethoxy- 2 methylpropiophenone 2959
KC	Human keratinocytes
MADM	Mesenchymal stem cell adipogenic differentiation medium
MSCM	Mesenchymal stem cell medium
NMR	Nucleic Magnetic Resonance
P/S	Penicillin-Streptomycin

PBS	Phosphate Buffered Saline
PDMS	Polydimethylsiloxane
PHBV	poly(3-hydroxybutyrate-co-3- hydroxyvalerate)
PLC	poly(lactide-co-Lcaprolactone)
PMMA	polymethyl methacrylate
RGD	Arginine-glycine-aspartic acid
RSPCA	Royal Society for the Prevention of Cruelty to Animals
Tan δ	Loss tangent
TCPS	Tissue culture polystyrene
Tg	Glass transition temperature
Tm	Melting temperature
UV	Ultraviolet
VEGF	Vascular endothelial growth factor
ECVAM	European Center for the Validation of Alternative Methods
SLS	Sodium lauryl sulfate
SC	Steartrimonium chloride
NHLF	Normal human lung fibroblasts
EGM-2	Endothelial growth media
SVN	Synthetic vascular networks
IPN	Interpenetrating polymer network

LIST OF SYMBOLS

SYMBOLS

Wswollen	swollen weight
Wdry	weight of lightly blotted samples
Wo	weight measured after UV exposure
ε	strain
σ	stress
E	Young's Modulus
G′	elastic modulus
G″	loss modulus
tanδ	loss tangent. The ratio of G″ to G′
δ	phase angle of the material.
Re	Reynolds number
Q	volumetric flow rate
Dh	hydraulic diameter of the tube,
ρ	fluid density
μ	dynamic viscosity of the fluid
A	cross-sectional area of the tube

CHAPTER 1

INTRODUCTION

1.1 Functions of the Skin

Skin covers the entire body and is considered the largest organ in the human body. The skin's primary function is to act as a barrier to guard the human body and underlying organs against environmental pathogenic microorganisms, mechanical impacts, and ultraviolet (UV) lights. Skin limits the penetration of foreign substances and prevents the loss of endogenous fluids. Skin plays a vital role in maintaining homeostasis by regulating the blood flow, controlling the body temperature, and synthesize metabolites such as vitamin D. Also, the skin contains sensory receptors that provide the perception of pain, temperature, and light (Humbert et al., 2017; Klenerman, 2015).

1.2 Human Skin Structure

It is composed of about 16 percent of body weight, covers 1.8 m^2 in the average adult human. The thickness of the skin varies from 1.5 to above 4.0 mm in different parts of the body. Skin is composed of multiple layers of tissues, and cells adhere to the underneath structure by connective tissue. Sensory nerve fibers in deeper layers of the skin ensure communication from and to the brain. Human skin comprises mainly three distinct regions (Figure 1.1) from top to bottom, namely epidermis, dermis, and hypodermis (Humbert et al., 2017; Klenerman, 2015).

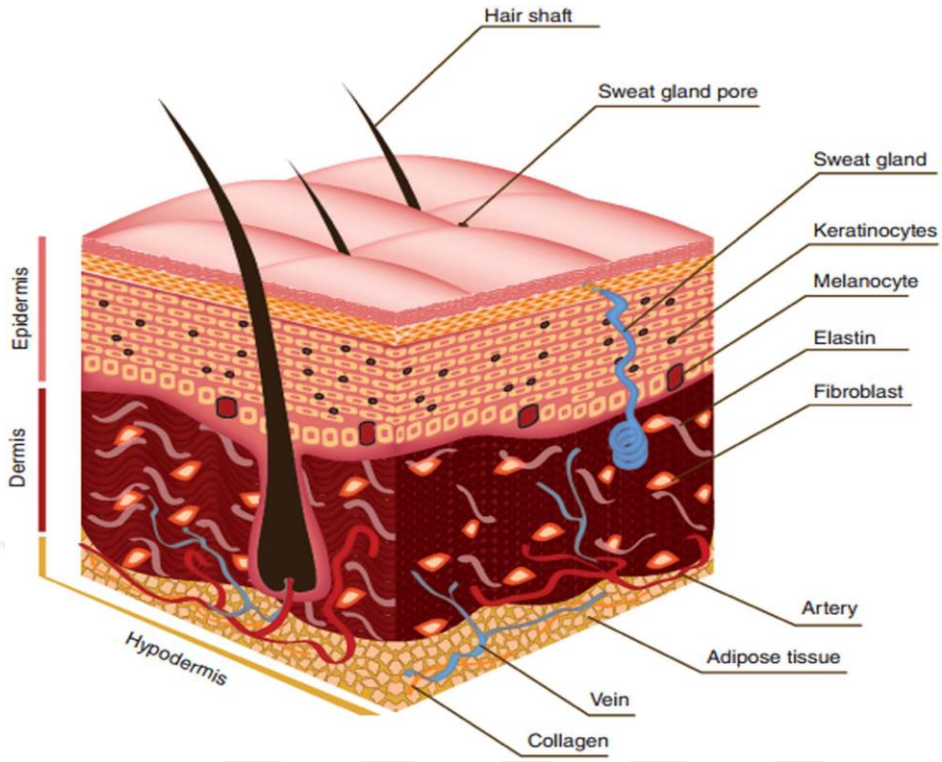

Figure 1.1. Schematic representation of the skin showing the three layers, the skin appendages, and the cellular constituents (Pereira et al., 2013).

1.2.1 **Epidermis**

The epidermis is the outermost layer of the skin. It separates the external environment from the inner body. It doesn't contain any blood vessels within it. The epidermis of the skin has five layers **(Figure 1.2)**. These layers are stratum basale, stratum spinosum, stratum granulosum, stratum lucidum, and stratum corneum, from deep to superficial. Stratum lucidum is found only on thick skin, which is on the soles of the feet and palms of the hand. The epidermis is made up of stratified epithelium. Epidermis basal layer is a single layer of cells that undergo cell division. Some of the cells retain within the basal layer. In contrast, others migrate upward and replace the cells in the upper layers leading to distinct layering in the appearance of the epidermis by altering the cellular content. Keratin production begins in the stratum spinosum. A keratinocyte is a cell that produces and stores the protein keratin. Keratin provides hardness and water-resistance to the

skin. Keratinocytes are the main component of the epidermis. Keratinocytes constitute at least 80% of the cells of the epidermis. Keratin production continues through stratum granulosum, where the cells die by loss of nuclei. The stratum lucidum and stratum corneum are made up of keratinized dead cells that are surrounded by lipids. The keratinocytes in the stratum corneum which are no longer multiplying regularly slough away, replaced by cells from the deeper layers. This migration process of the cells from the basal layer to the surface is called keratinization. (Marieb & Hoehn, 2010)

The epidermis is a dynamic tissue, continually renewing layers, and raises derivative structures such as nails, sweat glands, and pilosebaceous apparatuses. Migration of a basal cell between stratum basale and stratum corneum takes at least 14 days, and the transit through stratum corneum to outermost epidermis needs another 14 days (Burgdorf, 2004).

Three other cell types are dispersed among the epidermis. The first is called the Merkel cell, which stimulates sensory nerves to perceive the feeling of touch. The second is called a melanocyte. Melanocyte is the cell that provides melanin pigment for the skin. Melanin protects the skin from UV radiation damage by giving the skin its color. The third type of cell is called the Langerhans cell. These cells are involved in a variety of T-cell immune responses. They constitute nearly 8% of the total epidermal cells (Kolarsick et al., 2011).

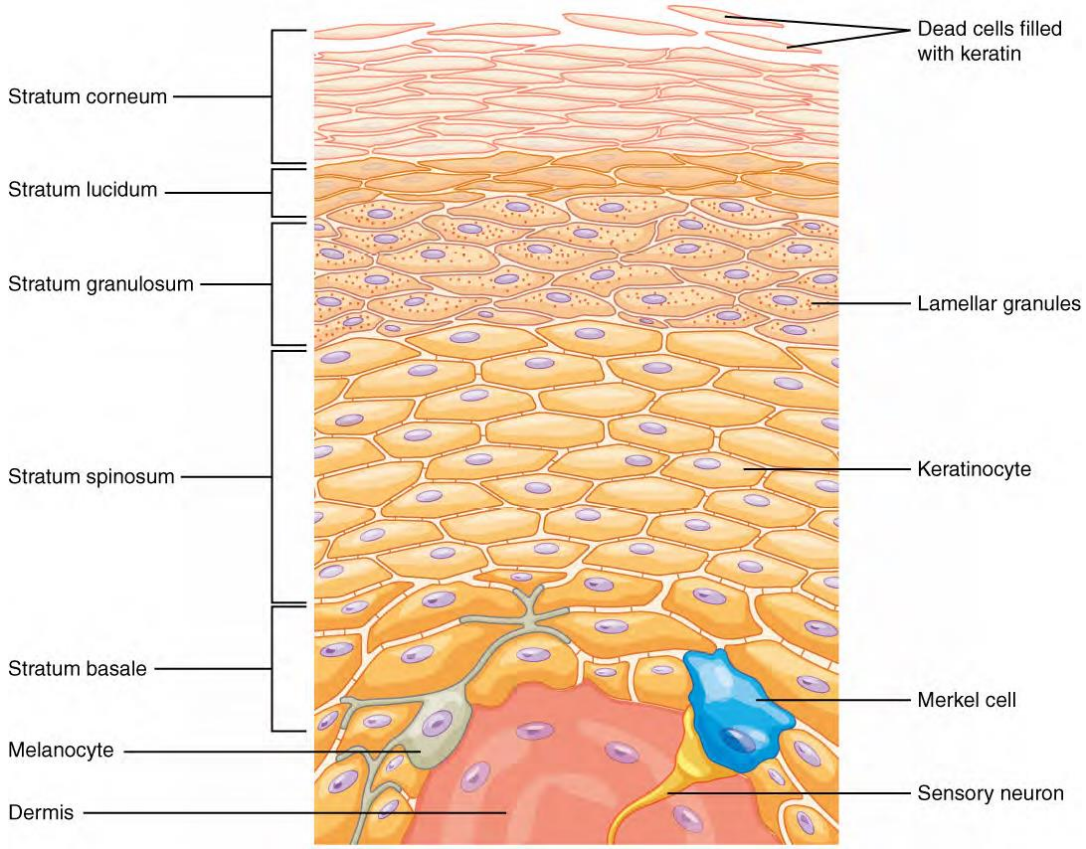

Figure 1.2. Layers of the epidermis: stratum basale, stratum spinosum, stratum granulosum, stratum lucidum, and stratum corneum (Marieb & Hoehn, 2010).

1.2.2 **Dermis**

The dermis comprises fibrous, filamentous, tight connective tissue, and the thickness is 1-2 mm (Humbert et al., 2017). It contains sweat glands, hair follicles, nerves, and an extensive blood and lymph vessels network. The dermis comprises an interconnected mesh of two layers of elastin and collagenous fibers produced by fibroblasts, the primary cell type of dermis. Other cell types of the dermis are macrophages, white blood cells, and mast cells. The dermis provides skin its pliability and elasticity. It has two layers, the thin superficial papillary layer and the deeper reticular layer. These layers do not have distinct boundaries (Figure 1.3). The upper layer of the dermis is tightly connected to the stratum basale of the epidermis. The papillary layer is an areolar connective tissue composed of

intertangled mesh structures of collagen and elastin fibers and intense blood vessels. The papillary layer contains pain receptors and touch receptors. It also has characteristic ridge patterns that are genetically determined and unique for everyone, which gives fingerprints identifying properties. Below the papillary layer, the reticular layer constitutes about 80% of the dermis thickness. The reticular layer is well vascularized. Collagen and elastin fibers provide elasticity and tensile strength by extending into both layers of the dermis. The reticular layer is also rich in nerves and sensory elements (J. Gordon Betts, Kelly A. Young, James A. Wise, Eddie Johnson, Brandon Poe, Dean H. Kruse, Oksana Korol, Jody E. Johnson, Mark Womble, 2013; Klenerman, 2015; Marieb & Hoehn, 2010)

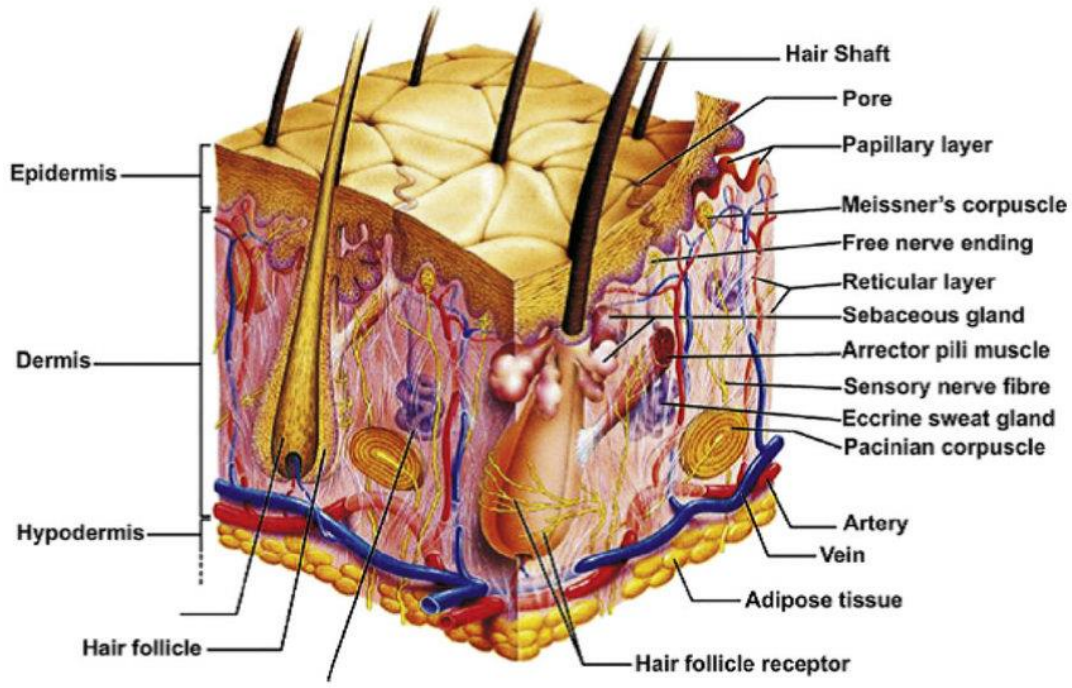

Figure 1.3. Schematic representation of the epidermis, dermis and hypodermis (Vitorino et al., 2015)

1.2.3 **Hypodermis**

The hypodermis is the deepest layer of the skin, and the thickness is 0.1 cm to several centimeters. It connects the skin to the underlying fibrous tissue of the rest of the body. It is also made up of the abundant supply of blood vessels, areolar connective tissue; therefore, it is hard to distinguish the borders of dermis and hypodermis. The hypodermis consists of fat-storing cells called adipocytes, which serve as an energy reserve, insulate the body temperature, and mechanical protection for the underlying structure (Somuncu et al., 2018) .

1.3 Tissue Engineering of Skin

Tissue engineering is an interdisciplinary field of engineering and life sciences to manufacture the biological tissue equivalents to restore, maintain, or improve tissue function (Langer & Vacanti, 1993). Human skin constitutes more than one-tenth of the body. Thus, infection, physical damages such as burns carry immense significance for this large organ (Somuncu et al., 2018). Skin replacement has been a long-awaited objective for modern medicine. Fresh skin allografts date back to 1871 as a clinical method of performing wound coverage (Reverdin & IVY, 1968). For over 30 years, a significant number of attempts have been made to produce a skin substitute that mimics the full function of the human skin by engaging in advanced tissue engineering. There are numerous skin damage types, including thermal trauma, acute and chronic wounds, or surgical operations. The earliest excision of the burned skin followed by immediate grafting has been reported since the 1970s (Janžekovič, 1970; Quinby et al., 1981)**.** The conservative approach to treat first and second- degree wounds was daily washing of the wound, followed by the application of topical antimicrobial. After third-degree burns, wounds were grafted with less widely expanded autografts without cadaver skin. According to Herndon et al., early excision and applying skin graft on patients who have lost the

body skin surface area between 50-98% significantly decreased the mortality compared to the conservative approach (Herndon et al., 1989).

Since the 1980s, an immense amount of work has been done to create a human skin substitute. These skin substitutes have been used as disease modelling test systems or for promoting wound healing. In addition, tissue-engineered skin models are demanded as non-animal test platforms for cosmetic and pharmaceutical, and disease biology research purposes (Abaci et al., 2017; Groeber et al., 2011; MacNeil, 2007; OECD, 2013).

These substitutes have been used for clinical applications and promoting a human-based system for pharmaceutical, and cosmetic research, and toxicology testing of their chemical ingredients. Routine toxicology analyses are conducted to ensure the safety of chemical compounds used in various industries. An ideal evaluation assay to determine the toxicity of the chemical substances on humans would require many human subjects of different sex and races, which is impracticable and immoral (Ng & Yeong, 2019). To date, considerable effort has been made to identify the potentially toxic or skin sensitizing chemicals on animal tests (Ramadan et al., 2016). Animal skins have severe limitations for research purposes such as up to 200 fold higher permeability compared to human skin (Schmook et al., 2001).

Ethical concerns increase for using of animals for pharmaceutical, cosmetic and chemical compounds. Number of animals sacrificed every year has gone up with the progression in medical biotechnology (Doke & Dhawale, 2015). According to the Royal Society for the Prevention of Cruelty to Animals (RSPCA), above 100 million animals are being used each year for research and testing purposes which can cause severe distress and pain to animals (Rossi, 2016). Animal model usage is limited due to ethical doubts. Low similarity of animal skin to the native human skin causes severe alterations between human and animal metabolism. Other differences could be listed as distinct absorption properties and pathways of metabolized chemicals and substances between species. Also, short lifespan of

animals restrains accurate monitoring of disease development. Thus, the outcomes of animal experiments are mostly restricted and debatable (Ng & Yeong, 2019; Sarkiri et al., 2019; Somuncu et al., 2018). Arising regulatory requirements and the ban on animal experiments imply the need for new high throughput test systems of substances (Bernauer et al., 2018; Schmidt et al., 2020). Significant amount of tissue-engineered skin models were developed as an alternative to animal testing. Nevertheless, there is no engineered skin prototype that entirely mimics the skin's structure, composition, and visual appearance (Somuncu et al., 2018).

1.4 Technologies Used in Skin Tissue Engineering

Tissue engineering is essentially fabricating a new functional living tissue using living cells associated with a matrix or scaffold to guide tissue development. Cells must establish functional structures using pre-programmed signaling and information to fabricate a new tissue substitute. Scaffolds can be made of synthetic materials, natural materials, or a combination of both. According to the tissue engineering approach, materials can serve as templates for host cells, and tissue ingrowth or implanted cells can be part of an engineered structure. Progress in the field was accelerated by the discovery of induced pluripotent stem cells (iPSCs). iPSCs can be derived from various somatic stem cell types. Stromal cells have been reprogrammed into a state which can be prodded into becoming many type of human cells and they are called iPCSs. They continue to proliferation *in vitro* and maintain potential to differentiate into many cell types. In addition, human iPSCs eliminate ethical issues, easily accessible, and can be handily produced specifically for patients (Langer & Vacanti, 1993).

1.4.1 Skin Models for Therapeutic Applications

The human skin consist unique features compared to other mammalian counterparts. Differences include presence of adipose tissue, pigmentation and skin

appendages (Suhail et al., 2019). The skin was the first tissue-engineered organ to pass preclinical research and used in clinical applications. The first bioengineered skin models were skin substitutes and emerged as an alternative to skin transplantation-associated problems. These substitutes were developed *in vitro* to mimic human skin. In vitro skin models also serve as functional models that allow more profound insight into cellular interactions (Oualla-bachiri et al., 2020). Skin regeneration research introduces a more permanent alternative to continuous graft replacement and care. Also, they were used for other applications such as *in vitro* human skin models for studying mechanisms underlyings or for pharmaceutical testing (Sarkiri et al., 2019).

In a study, cell-cell and cell-matrix interactions in regulating skin pigmentation were investigated with an *in vitro* skin model (Duval et al., 2012). Not only the presence of melanocytes but also their function was checked with this study. Collagen type I and fibroblasts were mixed for preparing the dermal component. Isolated human keratinocytes and melanocytes (1:1) were co-cultured for a week to form a monolayer culture, raised to the air-liquid interface (ALI), and kept for a week to allow keratinocyte stratification. Various growth factors were used in skin growth medium to stimulate melanocyte differentiation and melanin synthesis. Keratinocytes are known to promote melanocyte stimulation, therefore epidermal growth factor-based keratinocyte growth media were supplied and tested. Number of melanocytes increased but expected melanocyte differentation didn't occur and no melanin was synthesized by the melanocytes. Then, keratinocyte growth factor was added in place of the epidermal growth factor and experiment was repeated. Melanin pigment was seen on day 7, resembling as in the skin structure. Keratinocyte growth factor has been show to upregulate melanin synthesis. This skin model was an example for elucudating the role of melanocyte homeostasis.

Regulatory authorities, customers of the cosmetics industry, and the incompatibility of animal models have supported the establishment of human skin models to serve as predictive tools for toxicology and safety assessment studies. Percutaneous absorption testing is necessary for developing pharmaceutical products for

transdermal applications. The results of toxicological assessments performed with *in vitro* skin models were correlated with in vivo data to enable a reliable predictive model (Ruffner et al., 2016). Skin models provide great understanding of epidermal differentiation, cell proliferation and basement membrane organization (Suhail et al., 2019). Disease models of the skin provide insight into disease mechanisms. In a study, the psoriasis model was developed which exhibited the characteristics of the disease and thus showed the potential of the skin model for developing accurate treatments. Psoriasis, an autoimmune disease associated with hyperproliferation of epidermal keratinocytes, change in epidermal differentiation, and leukocyte infiltration causing the secretion of inflammatory mediators, was recently modeled *in vitro* (Lorthois et al., 2019). In this study, biopsies were taken from psoriatic and non- psoriatic patients. T-cells were isolated from peripheral blood. T cells were then activated using a T cell activation/expansion kit to mimic antigen-presenting cells. Keratinocytes and fibroblasts were also taken from the same donor. The psoriatic skin model was reconstructed as follows. Fibroblasts were seeded on a 12-well plate and cultured for 3 weeks with ascorbic acid to produce their extracellular matrix. After this culturing period, activated T cells were seeded on fibroblast sheets and cultured for another week in the presence of recombinant human interleukin-2 (IL-2). Then, keratinocytes were seeded on top of the sheets and cultured for a week in ascorbic acid and IL-2 containing medium, allowing keratinocytes to proliferate.

Next, sheets were raised, and ALI started for KC differentiation for 21 days. As a control, a non-psoriatic model was built with healthy T cells without activating T-cells. Reconstructed disease model demonstrated different degree of differentiation of KCs, hyperproliferation of basal KCs, and increased secretion of pro-inflammatory factors. Moreover, the disease model responded to a widely used immunosuppressive treatment. This model reflected major pathological features associated with psoriasis and may be helpful for testing new potential immunosuppressive drugs. Although infiltration of T cells into deeper layers was mimicked, the increase of vascular density and angiogenesis during chronic

psoriasis inflammation were neglected in this study. A more realistic model should include vascularization for better disease recapitulation.

Pharmacokinetic studies are necessary to estimate retained drugs in skin layers. The rate and extent of drug permeation after topical application needs to be clear for clinical efficacy studies. Separating the skin layers is crucial for defining rate-limiting factors (Thotakura et al., 2017). Limiting factors for permeation of topical and transdermal drugs include application site and type of the skin, presence of enzymes in the skin structure, drug solubility, and molecular weight. The stratum corneum, the outermost layer of the epidermis, is composed of dead keratinocytes, which forms tight junctions and acts as a permeation barrier for topically drugs. When stratum corneum is impaired as in the psoriasis, barrier function and permeation capability of the skin change (Rapalli & Singhvi, 2021).

For more accurate pharmacokinetic evaluation, effects of the metabolism of the drug by involving dynamic cellular factors, skin furrows, absorption through hair follicles and accurate immune responses must be involved to the skin models (Rapalli & Singhvi, 2021). Mimicking pharmacokinetic properties of transdermal penetration will be a strong tool for therapeutic applications (Briganti et al., 2003; Suhail et al., 2019).

1.4.2 **Conventional Skin Models**

Since the early 1900s, possible allergic reactions to active ingredients and excipients were tested on skin. Topical cosmetic and pharmaceutical excipients have been investigated for potency. Different methods have evolved for testing irritation effects. The use of animals as test subjects was implemented in 1944 by the US Food and Drug Administration (FDA) (Neil et al., 2020). However, the insufficient similarity to native human skin causes severe alterations between human and animal metabolism, making results debatable. In addition, with ethical

concerns, animal models are not suitable candidates for skin models (Ng & Yeong, 2019; Sarkiri et al., 2019; Somuncu et al., 2018).

Excised human skin was used as another alternative skin model for therapeutic applications. However, skin obtained from cadavers or plastic surgery raised ethical concerns. Limited availability and variability of donors prevented the standardization of this method. Also, features from the skin through different body sites related to different epidermis thickness and lipid compositions requires reviewing many parameters to produce a standardized method. Xenografts could not be an alternative skin model owing to different epidermis compositions of animal models and infection risk. Also, most human skin disorders have no counterpart in animals (Abd et al., 2016; Ruffner et al., 2016).

1.4.3 **Bioengineered Skin Models**

Developing bioengineered human skin models aims to mimic natural skin's structural and functional properties and is used as in vitro test systems. Initially, two-dimensional (2D) monolayer cultures were used as testing setups. However, monolayer keratinocyte cultures lacked inherent barrier function, making them unsuitable for routine testing (Botham et al., 1998). Also, monolayer cultures of different cell types fail to mimic cell-cell interactions, metabolic functions, and responses to various stimuli (Ali et al., 2015). Three-dimensional (3D) culture systems drew attention due to the better morphological resemblance of cellular mechanisms of different cell types and organs (Kapałczyńska et al., 2018).

Broadly, 3D scaffolds can be produced using two methods. i. producing a 3D scaffold and cell seeding on it, ii. direct producing 3D cell-laden scaffold in a gellable medium- the bioink. (Murphy & Atala, 2014a). This approach enables using thermoplastic materials such as poly(caprolactone) and poly(lactic acid) so that cells can be introduced after scaffold fabrication (Mondrinos et al., 2006). The second approach is the direct fabrication of cell-laden scaffolds by hydrogel

molding or 3D printing. This approach requires great attention to the fabrication conditions, such as cytocompatibility of material during processing and the shape and size of the extrusion nozzle. Water soluble biomaterials are required for 3D bioprinting. In 3D printing, the bioink is extruded through a printing nozzle and deposits material precisely on the three-axis. Printing optimization is required to find the optimum balance for cell survival and printing precision in order to enhance printing viability, printing pressure, nozzle geometry and diameter, deposition speed. Extensional flow during ejection was found the leading acute cell death reason in syringe needle flow. Viscosity is an important parameter in 3D printing. Bioink viscosity affects fluid-induced shear stress on cells. Shear stress can be reduced by altering the bioink formulation by introducing biocompatible polymers or changing the degree of crosslinking of the polymer (Aguado et al., 2012). Generally, more viscous bioink causes higher shear stress. Thus, having a bioink with lower viscosity is good for extrusion bioprinting applications. These improvements enable tuning bioink properties in terms of cell adherence, viability and metabolism, and mechanical properties.

First skin models contain only fibroblast and keratinocyte cells due to biomaterials' challenging optimization process (Groeber et al., 2011; Randall et al., 2018). Later skin models also include pigmentation (Duval et al., 2012; Szymański et al., 2020), vascularization (Eke, Mangir, Hasirci, MacNeil, et al., 2017; Frueh et al., 2018; Klar et al., 2014; Miyazaki et al., 2019; Oualla-bachiri et al., 2020), nervous system components (Bellas et al., 2012). Although vascularization/ angiogenesis has been studied for a long time, understanding fundamental principles of skin vascularization remains a challenge (Dikici et al., 2020). Living tissues rely on vascular networks that can provide vital oxygen, nutrition, and waste transport. Developing a vascularized skin model for implantation or *in vivo* research is very important. The successful implantation of skin substitutes relies on vascularization. Also, studying the effect of chemical, environmental and mechanical impacts would enlighten cell-cell and nutrition supply mechanisms for better recapitulating the human skin on *in vivo* models. (Zhu et al., 2017).

In a study, the group developed an *in vitro* skin model to study angiogenesis at both cellular and tissue levels (Dikici et al., 2020). A biocompatible polymer of poly(3-hydroxybutyrate-co-3- hydroxyvalerate) (PHBV) was used to fabricate artificial vascular networks via combining electrospinning and 3D printing techniques. PHBV channels were used as structural guides and physical support for endothelial cells (ECs) to create a preformed endothelium-like structure. Then, it was used to study the migratory response and tube forming capability of ECs in response to proangiogenic agents *in vitro*. A synthetic vascular network was designed using CAD software. Alginate was 3D printed as sacrificial material on PHBV. PHBV was electrospun on sacrificial alginate channels and alginate was then removed. PHBV synthetic vascular network channels were cannulated. Elongated hexagonal shaped PHBV SVN scaffolds (length: 30 mm and width: ~18 mm) were used in this study. Two groups were compared. i. Human dermal microvascular endothelial cells (HDMECs) seeded into channels ii. HDMECs seeded into channels, and human dermal fibroblasts were seeded to the outer surfaces of the channels. Samples were supplemented with vascular endothelial growth factor (VEGF) or non-supplemented and cultured for 7 days. HDMECs were evenly distributed within the channels and formed a monolayer, and the outer surface of the PHBV SVN was covered with HDFs. Results showed the presence of dermal cells, and the addition of VEGF increased the mean vessel count (no DF, no VEGF: 27.0 ± 1.3, DF, no VEGF 34.4 ± 1.9, FB+VEGF: 45.6 ± 2.0). They explored HDMESCs were not invading into the dermal layer of the developed model, either supplemented with VEGF or not. In this study, the importance of vascular networks for *in vitro* platforms to investigate the cell-to-cell interactions of complex tissue models was highlighted.

Several readily usable skin models were adopted by cosmetic firms such as EpiSkin (L'oreal, France), SkinEthic (SkinEthic, France) and EpiDerm. They are composed of stratified keratinocytes and used for corrosivity, photocytotoxicity and irritancy. But they lack complexity and barrier property (Alonso et al., 2020). Diffusion cell assays were employed as alternative penetration assay. They consist

of a glass diffusion cell and a membrane. Diffusion through membrane is measured under static or dynamic conditions. For many years diffusion cells were recreated for permeation assay and differences such as pressure change penetration properties completely and they do not reflect any complexity of native human skin (Zsikó et al., 2019). Different chromatography methods were combined to measure the penetration of the skin models. Altough quantitative drug penetration data were obtained from these studies, the efffect of cells metabolism and drug toxicity is neglected (Alonso et al., 2020).

In another study, a three-layered *in vitro* skin model involving immune and nerve components of the hypodermis structure was used to investigate the effect of components on homeostasis (Vidal et al., 2019). More profound knowledge of paracrine signaling within the skin is vital to upgrade the relevance of the skin models. In this study, skin layers were built and compared together and separately to analyze the neuroimmunocutaneous network. Sample groups included i. epidermis and dermis ii. Epidermis, dermis, and hypodermis, iii. hypodermis. Primary neonatal foreskin fibroblasts, primary neonatal keratinocytes, human-induced neural stem cells (hiNSCs), and primary human adipose tissue obtained from abdominoplasty were used in the skin model. Abdominoplasty patients used were obese or morbidly obese to involve inflammation in the skin model. The dermis layer was made up of fibroblast encapsulated collagen and silk hydrogel. Epidermis layer was by produced seeding primary keratinocytes directly on the dermis layers and raised the ALI a week after for keratinocyte differentiation for epidermis layer formation. The hypodermis layer was formed with silk sponge soaked in lipoaspirate. Abdominoplatiy lipoaspirates included adipocyte, pre-adipocyte, endothelial cells and smooth muscle cells and macrophages. Hypodermis layer was cultured for 3 weeks and then, hiNSCs were seeded on a collagen gel. Then, hypodermis layer was placed on top of the collagen gel, incubated for 10 minutes and flipped for another 15 minutes, so both sides were coated in the hiNSC gel. Epidermis and dermis component was put on the hiNSC-

coated hypodermis. Layers remained interfaced throughout 6-weeks culture. Macrophage markers CD68 and CSF1 were used for performing qRT-PCR on cultured hypodermis samples. Subsequently, CD68 and CSF1 at week 3 had 16- and 170-fold increase by week 6. Levels of pro-inflammatory markers namely interleukin-6 and RANTES increased from week 1. Overall pro-inflammatory secretion of the epidermis-dermis component was lower. Adding the hypodermis layer, cytokine activity was higher and increased with time. Epidermis, dermis, hypodermis with nerve groups showed the highest signal at the first week but this signal decreased afterwards. Also, proteomics results showed that the addition of nerve components and hypodermis resulted in expression of higher complex proteins. The apparent interaction between components and their effects on homeostasis were proven. The importance of including other cell types and neuronal components in skin models was validated.

Although research on the development of biofabricated skin models for pre-clinical studies is increasing, the need for the degree of complexity must be determined with experimental outcomes. Increasing the accuracy of clinical responses will allow predicting the effect of potential drug treatments.

The increased need for an artificial skin model accelerated the development of technologies with high automation and standardization with low cost (Mohammadi et al., 2016; Velasco et al., 2018). Complex features such as vascularization or immune components might be crucial to generate a disease model, but their integration into tissue remains challenging (Zhu et al., 2017). 3D printing of cells provided a spatially precise, computer-controlled deposition of cells which enables mimicking the natural human anisotropy of human skin (Tarassoli et al., 2018). Such models can be reinforced with the real-time monitoring and further controlled culturing microenvironment via microfluidic systems to mimic the dynamic design of natural human skin (Mohammadi et al., 2016).

1.4.4 Materials and Their Modifications for Skin Tissue Engineering

Gelatin is a natural polymer and is used extensively in skin tissue applications. Gelatin has a bioactive arginine-glycine-aspartic acid (RGD) sequence (Jason W. Nichol et al., 2010), which provides attachment and growth for different active molecules and cell types. However, the final products of gelatin are not readily usable due to poor physicochemical properties such as thermoreversibility and relatively low melting point (Van Den Bulcke et al., 2000). For this reason, gelatin was modified. The substitution of free amine groups of the gelatin with methacrylic anhydride is called methacrylation. RGD sequences are protected during methacrylation. With the addition of methacryloyl substituent groups, gelatin becomes photocrosslinked by exposure to UV radiation in the presence of a photoinitiator (Rahali et al., 2017). Photocrosslinker amount and photoirradiation duration allow manufacturing tunable.

Polysaccharides such as hyaluronic acid and alginate can also be chemically modified to obtain methacrylated polymers. Hyaluronic acid is a natural extracellular matrix polysaccharide thus has excellent biocompatibility. In addition, it directly interacts with cell surface receptors (Trudel & Massia, 2002). With the modification of methacrylate groups, hyaluronic acid polymerizes by exposure to UV radiation and forms a network structure in the presence of a photo initiator. Methacrylated hyaluronic acid (HAMA) has increased rigidity, becomes resistant to degradation compared to hyaluronic acid hydrogels, and keeps biocompatibility high (Burdick et al., 2005; Poldervaart et al., 2017). Hyaluronic acid is mostly not able to withstand the printing process, and therefore it is usually combined with other biomaterials. Hyaluronic acid is the main component in only a few studies. Hyaluronic acid derivatives were preferred mostly in cartilage tissue engineering as hyaluronic acid shows positive effect on cells in terms of chondrogenic differentaition or activity. Other hyaluronic acid-based bioink applications include studies focused on nerve regeneration, research in obesity, vascular grafts, heart, bone, adipose tissue engineering (Petta et al., 2020).

In a study, Gelatin, GelMA, hyaluronic acid, and HAMA were mixed to build a model for screeaning platform for candidate drugs to treat obesity (Kuss et al., 2018). Gelatin and hyaluronic acid are used as support materials to increase the viscosity, ease of printability and maintain the softness of the bioprinted scaffolds for cell spreading. Brown and white adipose progenitors were encapsulated into hydrogel bioink of different stiffness (soft, stiff, and stiff-porous constructs), 3D bioprinted, and UV crosslinked. Stiffness and structure of bioprinted scaffolds were tuned by changing the photocrosslinking time and printing pattern. Soft hydrogel scaffolds promoted white adipogenesis, while the stiff-porous hydrogel scaffolds provided the optimal condition for promoting brown adipogenesis. The porous samples of both cell types showed increased CCAAT/enhancer-binding protein 2 gene (marker for early stages of adipogenesis) expression and glucose uptake. These results showed the importance of nutrition perfusion and the exchange of metabolic waste for adipogenic differentiation. This study implies the importance and versatility of tunable hydrogels on cell microenvironment and functions. Eke et. al. fabricated a GelMA/HAMA bicomponent hydrogel, loaded with ADSC and stimulated new blood vessel formation *in vivo* compared to cell-free hydrogels (Eke, Mangir, Hasirci, MacNeil, et al., 2017)

Alginate is a natural polysaccharide obtained from marine organisms. Alginate shows excellent potential for tissue engineering due to controllable physicochemical properties and excellent bioactivity. It has been used in tissue engineering for decades since it offers low toxicity, is non-immunogenic, and is mucoadhesive. It is composed of two monomers bonded by glycosidic bonds. Namely, (1-4)-linked β-D-mannuronic acid (M unit) and C-5 epimer α-L-guluronic acid (G unit). These M and G blocks may create homopolymeric, heteropolymeric, or alternating sequences depending on the alginate source (Kadri et al., 2016). Alginate is extensively used because its rheological properties can be modified through pre-crosslinking via divalent cations such as Ca^{+2}, Cu^{+2} (Coates et al., 2013). Methacrylated alginate can be fabricated to avoid dissolving alginate in physiological solutions (Y. Gao & Jin, 2019).

1.4.4.1 **Interpenetrating Polymer Networks**

Interpenetrating polymer network (IPN) is combining the advantages of natural and synthetic polymers. The IPN formation occurs when the second hydrogel network is polymerized in a pre-polymerized hydrogel (Kilic Bektas & Hasirci, 2019; Nakagawa & Ebara, 2020). When only one polymer network is crosslinked, and the other polymer remains linear or branched, it is called semi-IPN (Aminabhavi & Dharupaneedi, 2017).

Alginate can be reversibly ionically crosslinked by the G subunits with divalent cations. MG blocks can also form weaker junctions (Pawar & Edgar, 2012). Alginate hydrogels involve van der Waals, electrostatic forces, and hydrogen interactions (Braccini & Pérez, 2001). However, alginate itself is not suitable for 3D cell encapsulation as it does not have cell binding sites. Bioactive sites of gelatin together with alginate can enhance hydrogel's properties by forming an IPN. Mixing gelatin and alginate and subsequently, alginate encounter calcium cations develop semi-IPN hydrogels. It has been shown that the preparation of IPN of gelatin and alginate allows excellent cellular response and tunable mechanical properties (Kadri et al., 2016; Tamayol et al., 2015). Kadri et al., synthesized IPN hydrogels based on GelMA and alginate polymers by photocrosslinking and ionically crosslinking $CaCl_2$ overnight and functionalized them with liposomes as nanovehicles. The aim of the study was to functionalize alginate/GelMA hydrogels with curcumin-loaded liposomes and to study their effect on the physicochemical properties of the obtained hydrogels to use in drug release studies. The group characterized IPN network in terms of physicochemical properties. Surface energy results showed IPN GelMA/alginate had the highest surface energy indicating that the IPN structure has upgraded the characteristics of the hydrogels. Although the addition of liposomes significantly lowered the surface energy of polymer network, it was still superior to the GelMA or alginate only. To validate, they measured elastic modulus (G') of the polymers, and IPN alginate/GelMA hydrogel showed the highest mechanical stability compared to GelMA and alginate hydrogels.

However, the incorporation of naturally soft liposomes significantly decreased the mechanical strength of IPN hydrogels. Therefore, they showed the importance of the characterization when modulating the final chemical properties of the IPN network (Kadri et al., 2016).

Another group developed an alginate bioink and printed it successfully with pre- and post-crosslinking methods (Hazur et al., 2020). The aim was to develop an alginate based bioink with good printability and enhanced shape fidelity without comprimising cell viability. In this study, they used a pre-crosslinked alginate solution by adding $CaCO_3$ and D-glucono-δ-lactone dropwise. $CaCO_3$ dispersions of 20, 50, and 80 mM were used to characterize the bioinks with different stiffness. After pre-crosslinking, bioink candidates were loaded with NIH/3T3 cells, and 3D printed. After printing, scaffolds were post-crosslinked with 100 mM $CaCO_3$. CLSM images showed, cells could not migrate within the hydrogels. They explained this as the lack of binding sites of bioinert alginate and excessive stiffness or a combination of both. Nevertheless, they reported hydrogel surface was covered with cells, and their viability was more than 90% for 14 days.

1.4.5 **3D Printed Skin Models**

3D bioprinting of human skin research is a high-demand field in the market. World-leading companies such as L'Oreal USA, Procter & Gamble (P&G) seek research collaboration agreements with 3D bioprinting companies and academia in 2015. In Korea, a 3D printing company announced its participation in a government-funded project to develop human skin tissue bioprinting in 2015. There is a growing demand and urgent need for this technology (Vijayavenkataraman et al., 2016).

A classical 3D bioprinting of skin model scheme is as follows: Cell extraction, expansion in vitro, cell loading into a hydrogel, bioprinting, post-processing, in vitro culture (using a bioreactor for tissue maturation in some cases) (Z. Li et al.,

2018; Murphy & Atala, 2014b; Vijayavenkataraman et al., 2016). In addition, modifying hydrogel mechanical properties, the addition of stem cells, biological and chemical interactions of procedure must be evaluated to produce a 3D printed skin.

Commercial cell lines of keratinocytes, hair follicles, mesenchymal stem cells, melanocytes, and endothelial and dermal fibroblasts are available. In addition, other specific cell types are obtained from skin biopsies.

Extrusion bioprinting was offered as more advantageous for tissue engineering than other techniques (McCormack et al., 2020). Skin bioink should mimic the properties of the extracellular matrix.

Cell-loaded advanced biomaterials or polymers (bioinks) have to be optimized for printability, spatial organization, and reproducibility. Synthetic polymers, such as poly (ε-caprolactone) (PCL), poly (lactic acid) (PLA), poly (lactic acid-*co*-glycolic acid) (PLGA), and naturally-derived biomaterials such as type I collagen, modified alginate, gelatin, and hyaluronic acid were evaluated for skin tissue engineering studies. The skin model should include signaling proteins for the healing mechanisms for various medical conditions to mimic the immune response (Perez-Valle et al., 2020). The addition of cytokines and growth factors is a great way to overcome the undesirable results of biomaterials and culture microenvironment. Signaling molecules need to be included in the bioinks to narrowing the disparity with *in vivo* conditions. At the same time, even though it is the best approach, cytokines still need to be verified and discussed for each cell and biomaterial type (Z. Li et al., 2018).

Despite promising developments, bioprinting has yet to see translation into clinical standards due to the use of complex and often custom-built equipment (Sutterby et al., 2020). In spite of their necessities for a functional skin model, oxygen and nutrient distribution, lymphatic and vascular systems are mostly not involved in 3D-printed skin models. Extrusion bioprinting has not met the clinical demand for producing fully functional skin. (Perez-Valle et al., 2020).Furthermore, due to

different cell types' sensitivities, tuning the extrusion pressure is crucial for cell-based bioprinting by controlling shear stress during the printing procedure (T. Gao et al., 2019). **Table 1.1** shows different bioink composition studies.

Table 1.1 . Studies involving different bioink compositions for a 3D printing biomimetic approach

Biomaterial	Cell Types	Bioprinting Conditions	Application	Evaluation	Reference
Fibrinogen, glycerol, gelatin, hyaluronic acid, aprotinin	Epidermis- human heratinocytes :human dark melanocytes (9:1), Dermis- human dermal fibroblast: human follicle dermal papilla cells: human dermal microvascular endothelial cells (6:1:1), Hypodermis-human preadipocytes.	Integrated tissue and organ printer, 3 cartridges for 3 layers, pneumatic pressure extrusion, metal nozzle	Viable cells were delivered directly onto wounds and replaced the missing hypodermis,dermis, and epidermis. Full-thickness wound closure was obtained.	Tested on mice. SEM analysis of morphology, H&E, Massons trichrome staining, Picrosirius red staining, Pan-Cytokeratin and Lamin A+C stain, Mel5, CD146, adiponectin, vimentin, ZO-1, keratin71	(Jorgensen et al., 2020)
$CaCl_2$; Alginate; Collagen, Fibrinogen; Alginate,Fibrinogen	Human umbilical vein endothelial cells transfected with red fluorescent protein, mouse 3T3 fibroblasts transfected with green fluorescent protein	Open source extrusion printer, microfluidic printhead, 3 multi-axial custom-made PDMS nozzles, extrusion printing	Hollow tubular structures containing concentric layers of two different types of cells, embedded hollow channels surrounded by hierarchical gel layers.	Inverted brightfield and fluorescence microscope's live stain images, ImageJ, cell viability.	(Attalla et al., 2019)
Gelatin, collagen I, elastin, fibrinogen, Laminin/ Entactin	Dermis-Neonatal human dermal fibroblasts, Basal layer- Laminin/Entactin, Epidermis-Neonatal Normal Human Epithelial Keratinocytes	Epidermis- pneumatic extrusion; Basal layer: jetting extrusion Dermis: plunger extrusion	Morphologically and physiologically relevant skin equivalent in a multiwell plate form, good barrier function	H&E, ZO-1, claudin I, e-cadherin, Keratin 1, Filaggrin, Keratin 15, Collagen I, Collagen VII, Ki67, MTT, barrier function, permeability	(Derr et al., 2019)
Sodium alginate, $CaCl_2$; Chitosan, genipin, PEG	Keratinocytes, human dermal fibroblast cells	Extruder-based bioprinter, two cartriges, high precision smooth flow tapered nozzle	3D printed constructs for potential skin regeneration after injury.	Rheological analysis, MTT, NMR, SEM, live-dead	(Hafezi et al., 2020)
Gelatin, sodium alginate, neonatal plantar dermis homogenate	Neonatal mice mesenchymal stem cell, neonatal mice keratinocytes, neonatal mice fibroblasts, sweat glands, hair follicles	Extrusion printing within a temperature-controlled chamber	Establishment of SG and HF co-regeneration. Applicable platform to investigate the interaction between sweat glands and hair follicles	Dil stainin, Quantitative real-time PCR, anti-KRT18, anti-KRT19, anti-KRT17, and anti-ALP, scratch assay, SEM	(Y. Zhang et al., 2021)

In the literature, main aims are to preserve printing geometry and to print polymers at room temperature. Heating and cooling steps make production of cell-loaded scaffolds harder. Also, producing room temperature printable bioink is useful for simple bioprinters that do not have temperature sensitive stages or printer cartridges (Aydin et al., 2020). Higher batch-to-batch consistency will potentially increase the scalability of scaffolds. Implementation of room temperature bioprinted scaffolds may have a higher success rate due to shape fidelity and consistency (He et al., 2020).

1.4.6 **Microfluidics Used in Skin Tissue Engineering**

Microfluidics technology offers real-time monitoring and controlled culturing microenvironments via control of fluid flow and physical factors (shear and hydrodynamic forces) and may connect multiple organ-on-chip models to form a sophisticated human-on-chip model (Mohammadi et al., 2016). Taking control of shear stress and tensional and compressive forces precisely with complete control on media perfusion will provide an excellent system for organ models. Along with micro-control of 3D printing technology, developing microfluidics models will be a significant achievement for creating artificial test systems and eventually replacing animal testing (Ashammakhi et al., 2020; Sutterby et al., 2020).

Improved microenvironment control allowed monitoring cell-to-cell interactions. Lack of functional blood vessels and vascularization on *in vitro* skin models blocks producing clinical *in vitro* skin irritation test. European Center for the Validation of Alternative Methods (ECVAM) reported that cytotoxicity measurements alone do not determine or predict the complexity of skin-irritation cascade (Fentem et al., 2001). The inflammatory respond should be evaluated from many other aspects such as barrier disruption, secreting of proinflammatory mediators, and cellular changes. Moreover, skin irritants may lead to edema, redness, vesiculation.

A group focused on the cytokine and growth factor release of keratinocytes, fibroblasts, and HUVECs to evaluate skin irritation and designed a simple microfluidic device (Jusoh et al., 2019). A microfluidic chip was produced using PDMS with channel structures patterned by lithography techniques. A double-channeled device containing dermal and epidermal sides allowed direct contact between the keratinocytes and the fibroblasts. The microfluidic chip was designed to mimic skin angiogenesis caused by irritant stimulation. Fibrin and dermal fibroblast were suspended in an endothelial growth medium, and a fibrin- DF matrix was formed. Keratinocytes were disassociated in EpiLife medium, mixed with fibrin matrix. DF matrix was injected into the left channel and KC matrix into the right channel. Fibrin gels were polymerized within the chip by a thrombin supplement. Then, the endothelial growth medium and EpiLife medium were then put into the designated reservoirs, and the chip was incubated for 1 d. Then HUVEC was suspended in the endothelial growth medium and adhered to the FB side (left) by tilting the chip to 90° for 30 min. Sodium lauryl sulfate (SLS) was used as irritant, and steartrimonium chloride (SC) as safe formulations -at least when it was formulated- were tested on the chip. Keratinocytes were treated with the SLS, and the epidermal barrier was disrupted. Also, facing DFs and KCs facilitated the cell-cell interaction that induces angiogenesis. The communication of keratinocytes and fibroblast regulates hormones and soluble factors, therefore, regulates homeostasis (Trompezinski et al., 2004). Enhanced vessel sproutings were seen on chemically irritated samples. Lumen formation and perfusable blood vessels were imaged using CD31 and collagen IV markers under both conditions. Higher SLS doses led to higher cell death. Instead of tracking cytokine levels, VEGF was followed for angiogenesis vascular permeability. VEGF is a potent mediator of angiogenesis and control the migration and proliferation of endothelial cells and decrease the vascular permeability. SLS and SLC behaved similarly from the angiogenesis formation aspect. Blood vessel sprouting was seen on both samples which indicates release of cytokines during inflammation process. Preliminary findings of this study showed SC induces skin irritation. This

microfluidic chip which maintained paracrine communication and allowed multiple different media channels for cell types which would help evaluating the change in growth factor concentration simultaneously as a result of irritation (Jusoh et al., 2019).

In a very recent study, a cost-effective, simple, reliable, and industrial-level scalable microfluidic chip was designed and tested for a skin model with epidermal and dermal components (Valencia et al., 2021). Immortalized human skin keratinocytes (HaCaT cell line) and primary human dermal fibroblasts were used in the dermo-epidermal model. Cells were modified to express hybrid histone protein providing their nuclei fluorescence. This study lacked biological analyses like immunocytochemistry or culturing conditions. Human fibrinogen and an antifibrinolytic agent were used to create a fibrin hydrogel to generate the stromal compartment. For gelation, thrombin was activated by adding $CaCl_2$ (1% w/v in saline). The microfluidic chip consisted of methacrylate layers (PMMA and PDMS), microporous polycarbonate membrane, vinyl layers, and adhesive vinyl tape, designed in CAD software cut on the plotter. The core of the chip design was two parallel fluidic chambers and a membrane between them. The membrane allowed the interchange of solutes between the lower and upper chambers. The upper chamber carries the bilayer model, the human epithelium with a stromal component with an epithelial. The size of each component was an important parameter in this model, so the lowest dermal height found in the human body to support epidermal growth and differentiation was used. The lower chamber was continuously supported with perfused culture medium. Double-sided adhesive sheets and nylon screws were used to seal and anchor the chip and tubes without any leakage. A parallel flow system between two liquids was designed to produce the stromal tissue inside the chip's upper chamber with a constant and determined height. The flow rate of parallel fluids was calculated precisely and used the viscosity measurements, Navier-Stokes equations, and continuity equation. Fluid flows were controlled by independent syringe pumps, which were connected through Teflon tubes to the inlet holes of the chip in the upper sheet. There was a

place for the pre-gel between two parallel flow gaps, and each of them was connected to the tubes. A fibrin pre-gel solution containing FBs was pumped with the accompanied parallel sacrificial Phosphate Buffered Saline (PBS) flow. Once the pre-gel left the upper chamber through the outlet tubes, pumps were stopped. Pre-gel was left there for 10 minutes for gelling and fabrication of the dermal part of the tissue. Then, the culture medium was pumped through the lowest chamber and did not stop until the end of the experiment and supplied nutrients to the cells through the membrane (Valencia et al., 2021).

Meanwhile, the upper chamber was given medium 24 hours to vanish PBS and keep the gel wet during FB spreading. Then the upper chamber was given KCs supplemented in the medium for 1 min via tubes connected to the pump. KCs were pumped on top of the stromal component and allowed for 6 h for cell attachment. Upper chamber fluid flow then stopped since the fresh medium flow from the lowest pump. The upper chamber could benefit other areas, such as pumping a drug to be tested or having a circulating flow. Dimensions of the designed chip were constant; therefore, change in biomaterial, flow rates, or experiment type could be calculated through mathematical formulas. To test this, three different flow rates and three hydrogel thnicknesses were tested, and reproducible results were obtained. The viability of cells after 4 days in culture was near 100% at day 4. Fluorescence images showed cells distributed and spread along with the chamber uniformly. This method brings automatization and standardization on the loading process of cellular components into chip and presented in this study as a proof-of-concept.

1.5 Aim of The Study

The aim of the study is to develop a 3-layered *in vitro* model biomimicking skin for drug testing and develop a bioink that can be printed at room temperature. In the literature, full-thickness skin is made up of epidermis and dermis layers. But hypodermis layer is an important parameter for toxicology studies. Addition of

hypodermis and the availability of evaluating each layer separately gives unique properties to this skin model. On the other hand, room temperature printable bioink was developed as another soft tissue or specifically skin bioink candidate. In the first part of the thesis, epidermis, dermis, and hypodermis layers are printed separately as the compartments to obtaina bottom-up construct. Each layer can be used separately or together and place into microbioreactor chips like lego blocks. Herein, all layers are studied alone and combined to define their effects on the trilayered skin model *in vitro*. The epidermis layer is composed of 3D printed poly(lactide-co-L-caprolactone) (PLC) and keratinocyte cells; the dermis layer is 3D printed from GelMA where dermal fibroblasts (DF) and adipose-derived stem cells (ADSC) (3:1) are encapsulated, and hypodermis layer is also 3D printed with GelMA which contains DF, and adipogenic differentiated ADSCs (1:3). Cell compositions are arranged in each layer to mimic the native skin. Adjusting cell ratio of dermis and hypodermis that are often mentioned together provides higher similarity to the native human skin.

The chip is designed to allow an air-liquid interface for keratinocyte maturation, dynamic culture of hydrogel encapsulated dermal and hypodermal layers and a bottom reservoir-channel system for collecting penetrated drugs for downstream analysis. The skin model is composed of adipocytes, mesenchymal stem cells, human dermal fibroblasts, and human keratinocytes. After successfully producing the skin substitute, the 3D model was used for testing drug penetration. In this study, dexamethasone, a common topical corticosteroid drug ischoosed as the model drug to observe the drug penetration via skin layers into the circulation using the microbioreactor microfluidics setup. Testing skin penetration is crucial because skin cosmetic products and pharmaceutical products require toxicology testing by law and currently there is no end-product system that can measure drug penetration.

The second part of the thesis aim to develop a bioink composition that can be printed without the need for cooling or heating. A hydrogel composition composed of HAMA, alginate, and GelMA was produced, and the bioink was pre-crosslinked

with $CaCl_2$ to achieve viscoelastic properties required for 3D printing at room temperature. The bioink is post-crosslinked with $CaCl_2$ and UV further to obtain structural stability. Printing the cell loaded bioink at room temperature allows higher printing shape precision as printing platform and printer's cartridge temperature tuning become less problematic. Expensive heating and cooling systems of complex printer devices slow down scientific process of 3D printing by being less available. Room temperature printable bioink with tunable properties will allow fabrication of tunable cell-loaded scaffolds. These multiple crosslinking schemes allow the product of an interpenetrating network bioink that can be printed at room temperature L929 fibroblasts and ADSC: DF cells are used in the bioink, and cell viability and proliferation were studied in the bioprinted gels.

CHAPTER 2

MATERIALS & METHODS

2.1 Materials

2-hydroxy-4'-(hydroxyethoxy)- 2-methylpropiophenone (Irgacure 2959), type A gelatin from porcine skin (90–110 bloom), methacrylic anhydride, bovine serum albumin (BSA), alginic acid sodium salt from brown algae (low viscosity), paraformaldehyde, Coomassie brilliant blue, hyaluronic acid sodium salt from *Streptococcus Equi*, deuterium oxide were purchased from Sigma-Aldrich (USA). N-N, Dimethylformamide was purchased from Merck (Germany). Live–Dead cell viability/cytotoxicity kit, Dulbecco's Modified Eagle Medium with and without phenol red, newborn calf serum, HCS LipidTOX™ Green Neutral Lipid Stain, for cellular imaging were from Thermo Fisher Scientific (USA). Purasorb PLC 7015 was bought from Corbion (Holland). Dimethyl sulfoxide (DMSO), Triton X-100, was purchased from AppliChem (USA). SnakeSkin dialysis tubing was the product of HyClone, Thermo Scientific (USA). CD31, CD45, CD 105, Mouse IgG1 κ Isotype Control (mouse anti-human), CD31 (Alexa Fluor 488 tagged, for immunofluorescence), CD90 (Alexa Fluor 647 tagged, mouse anti-human) were obtained from Biologend (USA). Alexa 532 Phalloidin, Alexa 488 goat anti-mouse secondary antibody, 4′,6-diamidino-2-phenylindole (DAPI) were from Invitrogen (USA). Trypsin EDTA solution B and C, L-Glutamine solution were purchased from Biological Industries (Israel). Endothelial Cell Basal Medium-2 (EBM-2) and EGM-2 SingleQuots were from Clonetics, Lonza (USA). Endothelial Cell Growth Medium was the product of Cell Applications, Inc. (USA). Mesenchymal Stem Cell Adipogenic Differentiation Medium (MADM), mesenchymal stem cell growth supplement (MSCGS, Cat. No. 7552), fetal bovine serum (FBS), mesenchymal

stem cell adipogenic differentiation supplement (MADS), fibroblast medium (FB) were from ScienceCell (USA).

2.2 Methods

Production of Hypodermis, Dermis, and Hypodermis Layers

Gelatin methacrylate (GelMA) was synthesized, photocrosslinked and 3D bioprinted to mimic dermis and hypodermis layers of the skin. Hypodermis and dermis bioink were prepared by loading adipose-derived mesenchymal stem cells (ADSCs), primary human dermal fibroblast cells from adult human skin (DF), and adipocytes in different ratios to photocrosslinkable GelMA solution.

The epidermis was produced by 3D printing of poly(lactide-co-L-caprolactone) copolymer (PLC) with a 70/30 molar ratio of L-lactide and ε-caprolactone (PURASORB® PLC 7015). Afterward, samples were washed and sterilized with UV, and keratinocyte cells (KCs) were seeded on them. In addition, samples were treated with Air-Liquid Interface (ALI) for keratinocyte differentiation.

2.2.1 Synthesis of Methacrylated Prepolymers

Methacrylated hyaluronic acid (HAMA), and Gelatin Methacrylate (GelMA) were synthesized and characterized as dermis and hypodermis bioink candidates. Initially, HAMA was to culture Human umbilical vein endothelial cells (HUVEC) to provide prevascularization motives to the skin model (Eke, Mangir, Hasirci, Macneil, et al., 2017). Later, mixture of HAMA, GelMA and alginate was produced as an alternative bioink for soft tissue.

2.2.1.1 **HAMA Synthesis**

Methacrylated hyaluronic acid (HAMA) was synthesized, according to (Busatto et al., 2016; Chandrasekharan et al., 2019). Briefly, 1 % hyaluronic acid (HA) was dissolved overnight in distilled water at ambient temperature. Dimethylformamide (DMF) was added slowly to the hyaluronic acid solution and stirred until mixed well. The solution was transferred to a cold room (at +4 °C) for 1 hour to cool down. Methacrylic anhydride was added dropwise to the mixture to have a 5 % (v/v) solution at 4 °C and stirred. pH was adjusted to 8-9 using 5 M NaOH and kept constant for 5 hours. The reaction solution was dialyzed against distilled water for five days. Dialysis water was changed twice a day throughout the dialysis process. HAMA solution was filtered, froze at -20°C, and lyophilized for five days. Synthesized HAMA was stored at +4°C until used.

2.2.1.2 **GelMA Synthesis**

GelMA was synthesized according to (Shirahama et al., 2016). Briefly, Type A porcine skin gelatin (20% (w/v)) was dissolved in 0.25 M carbonate-bicarbonate buffer at 60°C. Methacrylation reaction was initiated by adjusting pH to 9 with 5 M NaOH. Next, methacrylic anhydride 2% (v/v) was added dropwise into the gelatin solution and stirred at 50°C. After 3 hours of stirring, pH was adjusted to 7.4 to terminate the reaction using 6M HCl. The mixture was transferred to snakeskin dialysis tubing 10000 mW cutoff and dialyzed against distilled water for two days. Distilled water changed twice a day. Dialyzed solution was filtered, frozen at -20°C, and lyophilized for 3 d. Synthesized GelMA was stored at +4°C until use.

2.2.2 **Preparation of Hydrogels**

Hydrogels were prepared by free radical polymerization of prepolymers using photoinitiator 2-hydroxy-4’-(hydroxyethoxy)-2-methylpropiophenone (Irgacure

2959) and UV curing. ALMA, HAMA, and GelMA solutions were exposed to 365 nm UV (Omnicure s1000) for 4 seconds to obtain crosslinked hydrogels. 1.4 W/s UV irradiation was applied on prepolymers from a 3 cm distance. Defining UV exposure duration is explained in Section 2.2.3.3.

2.2.2.1 **Preparation of GelMA Hydrogels**

GelMA and IrgaCure were mixed at different ratios to find optimum mechanical, swelling, and viability conditions. IrgaCure (0.3, 0.6 and 1% (w/v)) were dissolved in PBS at 60°C. GelMA (10, 15, and 20% (w/v)) was added to the solution and mixed until fully dissolved. Prepolymer was poured into 48-well-plate, or 3D printed depend on the application. UV irradiation was applied as explained conditions above for crosslinking of GelMA prepolymer.

2.2.2.2 **Preparation of HAMA-Alginate-GelMA Hydrogels**

Irgacure 2959; 0.6 % (w/v) dissolved in dH_2O at at 60 °C. Lyophilized HAMA 0.1 % (w/v) and Alginate Low Viscosity 4% (w/v), GelMA 10 % (v/w) and IrgaCure 0.6 % (v/w) were added into the solution and mixed at 50 °C until homogeneously distributed. 75 mM $CaCl_2$ in dH_2O was added to prepolymer solute and mixed overnight at ambient temperature to obtain a 30 mM $CaCl_2$ pre-crosslinked gel mixture. The mixture was poured into 48-well-plate or 3D printed depend on the application. After that, irradiation applied to on construct as explained above. Finally, produced crosslinked polymer was incubated in 75 mM or 150 mM $CaCl_2$ in dH_2O for 5 minutes for post-crosslinking samples or and no post-crosslinking was applied for only pre-crosslinked samples.

2.2.3 Characterization of Hydrogels

2.2.3.1 Nucleic Magnetic Resonance (NMR) Spectra of Methacrylated Prepolymers

2.2.3.1.1 HAMA

NMR (Biosurplus, Avance Bruker DPX 400, USA) experiment was performed at 400 MHz, and 16 scans were used to determine the incorporation of methacrylate groups into hyaluronic acid (HA) and determine the degree of methacrylation. HA and HAMA samples were dissolved in deuterium oxide (D_2O, 20 mg/mL). The DM was calculated from the relative integration of the methacrylate protons (5.6 and 6.0 ppm) to the methyl protons in HA (1.8 ppm) (Oudshoorn et al., 2007).

2.2.3.1.2 GelMA

NMR (Biosurplus, Avance Bruker DPX 400, USA) spectrometer was performed at 400 MHz and 16 scans to determine the substitution degree of methacrylate groups GelMA. Gelatin and GelMA samples dissolved in deuterium oxide (D_2O, 20 mg/mL). NMR analysis was performed to calculate the degree of methacrylation using. The NMR spectra of GelMA and gelatin were normalized to the phenylalanine signal between 6.9-7.5 ppm, which comes from gelatin and does not involve a methacrylation reaction. Subsequently, integrated lysine methylene signals (2.8–2.95 ppm) of gelatin and GelMA were determined. The following formula calculated the degree of methacrylation of GelMA (Jason W. Nichol et al., 2010).

$$\text{DM } (\%) = \left(1 - \frac{\text{A}(\textit{lysine methylene of GelMA})}{\text{A}(\textit{lysine methylene of unmodified gelatin})}\right) \times 100$$

(1)

2.2.3.2 **Uniaxial Compression Tests of Hydrogels**

Uniaxial unconfined compression tests were performed on GelMA and HAMA-Alginate-GelMA hydrogels. 600 µl of polymer solutions were poured into custom-made cylindrical polydimethylsiloxane (PDMS) mold (r=5.58 mm, ht=11.16 mm) and crosslinked as explained in Section 2.2.3.2. Gels were produced on test day and incubated in PBS at 37°C until testing. A compression test was performed using the Uniaxial mechanical testing device (CellScale UniVert, Canada). A minimum of three samples from each group was used (n≥ 3). Uniaxial compression test was performed at a 1 mm/min rate with a 80% displacement using a 10 N load cell. The slope of the elastic region of the stress-strain curve was recorded as elastic modulus (or Young's Modulus). Young's Modulus was calculated by GraphPad Prism 8 software. Strain (ε, no unit), stress (σ, MPa) and elastic modulus (Young's Modulus, E, MPa) of samples were calculated by the following equations:

$$\varepsilon = \frac{\Delta l}{l\mathrm{o}}$$

(2)

lo (mm) was the initial length of the sample, while Δl (mm) is the difference of length by the applied force.

$$\sigma = \frac{F}{A}$$

(3)

F (N) was the stress applied to the sample, while A (mm^2) is the sample area in which force was applied.

$$E = \frac{\sigma}{\varepsilon}$$

(4)

2.2.3.3 **Determining UV Exposure Duration of Hydrogels**

UV exposure time was defined for GelMA and applied for HAMA-Alg-GelMA hydrogel. GelMA solution with a concentration of 15 %v/w and IrgaCure 2959 of 0.6 % v/w were dissolved in PBS. The solution was exposed to 365 nm UV with the power of 1.4 W/s for 1, 2, 3, 4 and 5 s to determine optimal exposure time. Samples were incubated in PBS at 37°C for five days. The physical appearance of hydrogels was observed, and live-dead tests were performed for evaluation of L929 viability.

2.2.3.4 **Swelling and Water Uptake Analysis of Hydrogels**

Swelling and water uptake were defined for GelMA and HAMA-Alg-GelMA hydrogels. For this analysis, 600 µl of sample polymer solutions was prepared in PBS and poured into PDMS coated 48-well plate and crosslinked. A minimum of three samples from each time point ($n \geq 3$) was tested. The crosslinked hydrogels were weighed after UV exposure indicated below by W_0. Samples were then incubated in dH_2O at ambient temperature for 72 hours. Every 24 hours, samples were removed from the well plate and lightly blotted. The weight of lightly blotted hydrogels was indicated by $w_{swollen}$. All samples were lyophilized for one day and weighed to obtain w_{dry}. Water content and water uptake of the hydrogels were calculated according to the following formulas (5, 6):

$$\text{Swelling (\%)} = \frac{\text{Ws-Wd}}{\text{Wswollen}} \text{x100} \quad \textbf{(5)}$$

$$\text{Water uptake (\%)} = \frac{\text{Ws}}{\text{Wo}} \text{x100} \quad \textbf{(6)}$$

Where Ws represents swollen weight (g), Wd weight of lightly blotted samples (g), and Wo weight measured after UV exposure.

2.2.3.5 **Rheological Measurement of Hydrogels**

Rheological measurements of bioink formulations were performed with a Malvern Kinexus Lap+ Rotational Rhemometer (Malvern Panalytical**,** UK) with parallel plate steel 40-mm geometry at ambient temperature. GelMA (10%, w/v), alginate (4%, w/v), GelMA (10%, w/v)- alginate (4%, w/v), GelMA(10%, w/v)- alginate (4%, w/v)- HAMA (0.1%, w/v), GelMA(10%, w/v)- alginate (4%, w/v)- HAMA (0.1%, w/v) - 75 mM $CaCl_2$ pre-crosslinking samples were added to the bottom

plate and subsequently, the steel plate geometry was lowered until contact with the surface of the bioink sample. For solid phase gels (G′ > G″), the geometry was lowered further until the axial force on the instrument equaled 0.02 N. For liquid phase gels, geometry was lowered until contact with the surface. After contact, the shear elastic modulus G′, shear loss modulus G″, and loss tangent tan(δ) were measured for each hydrogel bioink using a frequency sweep between 0.50 and 100 Hz and at 1 Hz temperature sweep between 10 to 40 °C. All rheological measurements were conducted in triplicate. Results were analyzed with GraphPad Prism 8.

$$\eta^* = \frac{\sqrt{G'^2 + G''^2}}{\gamma'} \quad \textbf{(7)}$$

$$\tan\delta = \frac{G''}{G'} \quad \textbf{(8)}$$

Storage modulus was shown as G′ and loss modulus was shown by G″. The ratio of G″ to G′ is defined as the loss tangent (tan δ), where δ is the phase angle of the material.

2.2.4 Characterization of Poly (L-Lactide-co-L-Caprolactone) Scaffolds (PLC)

2.2.4.1 Differential scanning calorimetry of PLC Copolymer

Differential scanning calorimetry (DSC) was carried out to determine the printing temperature of the copolymer using a Diamond Differential Scanning Calorimeter (Perkin Elmer, US). Glass transition temperature (Tg) and melting temperature (Tm) of PLCs before and after printing was measured. The DSC measurements were performed from -50 °C to 220 °C at a heating rate of 10°C/min, melted at

195°C, and kept 3 min, then cooled to -50 °C at a cooling rate of 10 °C/min, kept at -50 °C for 3 min. Finally, the second heating run was reheated to 195 °C at a heating rate of 10 °C/min.

2.2.4.2 **Uniaxial Tensile Test of PLC**

The tensile test was performed for solvent casted copolymer and 3D-Printed PLC scaffolds. For preparing casting solution into PDMS mold, PLC was dissolved in chloroform 10% (w/v). Two different patterns were tested for the tensile test. Mesh **(Figure 4)** and wave-patterned 3d printed PLC were compared for use in the epidermis layer. Uniaxial mechanical testing (CellScale UniVert, Canada) was conducted at a rate of 1 mm/s with a 100% displacement using a 200 N load cell. Young's Modulus was calculated by GraphPad Prism 8 software using equations 2, 3, and 4 (given in Section 2.2.3.2).

2.2.4.3 **Weight loss of PLC**

A degradation test was performed on 3D-printed PLC scaffolds. Scaffolds were initially sterilized with 70% ethanol (EtOH) and air-dried in a laminar flow hood. Then, samples were weighed, and initial weights were indicated below by Wo. Samples were incubated in DMEM High Glucose media at 37 °C in orbital shakers for eight weeks. For the first month every week and on the second month, three samples were weighed. Next, samples were washed with sterile filtered dH_2O and air-dried in the laminar flow hood. Dry samples were weighted and weight at the given time point is indicated by W_i. The following equation calculates weight loss of PLC:

$$\text{Weight loss } (\%) = \frac{\text{Wo} - \text{Wi}}{\text{Wo}} \text{x } 100 \quad \textbf{(9)}$$

2.2.5 **3D Printing of Layers**

2.2.5.1 **3D Printing of GelMA**

GelMA prepolymer (GelMA 15% (w/v), IrgaCure 0.6 % (w/v)) was prepared and heated to 37°C for pouring into the cartridge of the 3D Bioplotter (EnvisionTEC GmbH, Germany). The printing was performed by a 23 Gauge conical plastic nozzle with an inner diameter of 0.33 mm at 0.6 bar pressure. The ambient temperature was adjusted to 24°C. The printing platform temperature was fixed at 10°C. The cartridge was heated to 22°C, and the hydrogel's temperature was stabilized for an hour before printing. Each layer was 90° to the layer below, and three layers for the dermis layer and five layers for hypodermis were printed (Figure 4). 3D Printed GelMA scaffold was exposed to 365 nm UV (Omnicure s1000) for 4 seconds at a 3 cm distance to obtain crosslinked GelMA hydrogel.

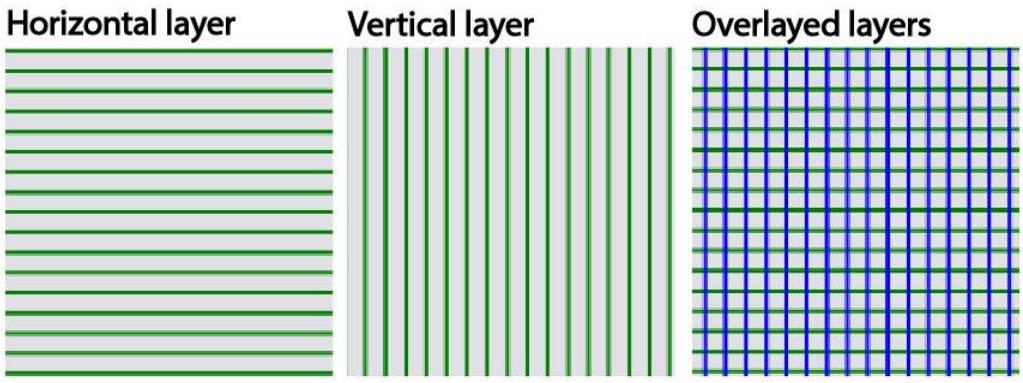

Figure 2.1. Schematic representation of 3D printed GelMA and HAMA-Alginate-GelMA constructs

2.2.5.2 **3D Printing of HAMA-Alginate-GelMA Scaffold**

30 mM $CaCl_2$ pre-crosslinked HAMA-Alginate-GelMA prepolymer (HAMA 0.1% (w/v), alginate 4% (w/v), GelMA 10% (w/v), IrgaCure 0.6 % (w/v)) was prepared and heated to 37°C for pouring into the cartridge of the 3D Bioplotter

(EnvisionTEC GmbH, Germany). The printing was done by a 24 Gauge conical steel nozzle with an inner diameter of 0.33 mm at 0.3 bar pressure. The speed of the extrusion of the polymer was 40 mm/s. The ambient temperature was adjusted to 24°C. The printing platform temperature was fixed at 15°C. The cartridge was heated to 30°C, and the hydrogel's temperature was stabilized for an hour before printing. Each layer was 90° to the layer above **(Figure 4).** 3D Printed GelMA scaffold was exposed to 365 nm UV (Omnicure s1000) for 4 s at a 3 cm distance to obtain crosslinked hydrogel.

2.2.5.3 **3D Printing of poly (L-Lactide-co-Caprolactone) Scaffold**

The scaffolds were produced by 3D printing of L-lactide/Caprolactone (PLC) copolymer using a 3D Bioplotter (EnvisionTEC GmbH, Germany). The needle size of the extruder was 24 Gauge (inner diameter of 0.3 μm). The ambient temperature of the printer was adjusted to 24°C while the platform temperature was fixed at 30°C. For printing, the copolymer was loaded into the cartridge and heated to 180°C for 30 min. After the polymer temperature was stabilized, the cartridge was heated to 195°C. A constant pressure of 8 bars was applied throughout the printing process. The speed of the extrusion of the polymer was 1 mm/s. 4 layers were printed with a steel nozzle with 0.45 mm inner diameter. Thus, the thickness of the scaffold was 1.2± 0.3 mm. Each layer was 90 ° to the layer below, and the top 2 layers were shifted 50% relative to the bottom layers. Waves with changing frequency were used for each layer to reduce the pore size of the scaffold **(Figure 2.2).**

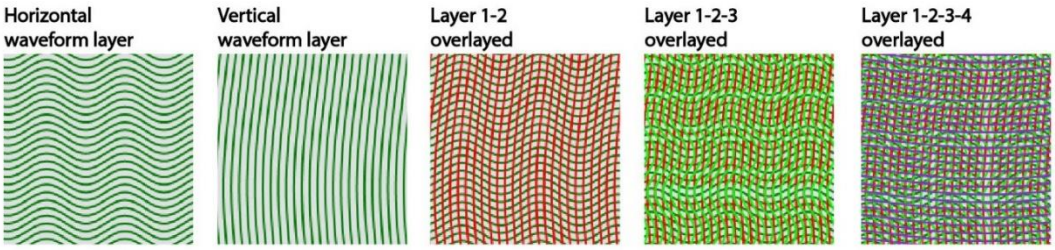

Figure 2.2. Schematic representation of layers of the 3D printed strand shifted wave PLC scaffolds.

2.2.6 *In Vitro* Experiments

2.2.6.1 Viability and Cytotoxicity Studies

2.2.6.1.1 Live-Dead Viability Assay

The live-dead cell viability assay was performed to determine cytotoxicity. The medium of the samples was discarded and washed with PBS. Live dead experiments were performed for L929 fibroblasts on PLC membrane in GelMA, ADSCs, DF, and adipocytes in GelMA. Samples were stained with Calcein-AM and ethidium homodimer-1 (2 % (v/v) and (0.5 % (v/v) respectively in colorless medium) in DMEM colorless media and incubated at 37°C for 20 minutes, then washed with PBS.

Confocal analysis and cell imaging were performed with Zeiss LSM 800 Confocal Laser Scanning Microscope (Germany). Live-dead assay labels viable cells as green while dead cells are red. Cell counting was conducted via Image J-NIH Software. The following equation was used to calculate the viability of cells in hydrogels:

$$\text{Viability of cells (\%)} = \frac{\text{Live cells (Green signal without red)}}{\text{All cells(Green signal only)}} \times 100 \quad \textbf{(10)}$$

2.2.6.1.2 LipidTOX Green- DAPI Staining

LipidTOX- DAPI staining was performed to mark neutral lipids and cell nuclei. The medium of the samples was discarded and washed with PBS. Fixation of cells

was performed with 4% PFA in PBS for 15 min at ambient temperature. PFA solution was removed, and samples were rinsed with PBS. HCS LipidTOX Green Neutral Lipid Stain was diluted in PBS (1:200), and cells were incubated at ambient temperature for 30 min. Afterward, the DAPI (1:1000) stain was added and incubated at ambient temperature for 15 min. Cell imaging was performed with Zeiss LSM 800 Confocal Laser Scanning Microscope (CLSM).

2.2.6.1.3 Cytotoxicity Experiments with L929 Fibroblast Cells

2.2.6.1.3.1 L929 Fibroblast Cell Culture

The growth media of L929 fibroblast cells was DMEM-High Glucose supplemented with fetal bovine serum (10%) and Penicillin/Streptomycin (P/S) (1%). The medium of samples was changed every three days. Cells were passaged after detachment from the surface of tissue culture polystyrene (TCPS) flask using trypsin B solution (0.25 % Trypsin, 0.05 % EDTA in Puck's Saline A) at 37°C for 5 minutes and centrifuging at 3000 rpm for 5 min. Passages 22-26 were used for each experiment. Live dead assay was performed every seven days for each viability experiment.

2.2.6.1.3.2 Viability of L929 Fibroblast Cells on PLC Films

PLC was dissolved in chloroform 10% (w/v) and cast on custom-made, rectangular PDMS molds to obtain smooth films. Then, 2.10^5 cells/ml L929 fibroblast cells were seeded on 0.64 mm^2 PLC film and incubated for 21 days. Live dead analysis was performed on days 1, 7, 14, and 21.

2.2.6.1.3.3 The Effect of UV Exposure on L929 Fibroblast Cell Viability

Live dead assay was performed to determine the optimal UV exposure duration for cell viability in GelMA. GelMA 15 % (v/w) and Irgacure 0.6 % (v/w) was dissolved in DMEM High Glucose. Then, 3.10^6 cells/ml L929 fibroblast cells were mixed homogenously with GelMA solution at 37 °C. 120 μL GelMA solution poured into a PDMS coated 48-well plate and exposed to 1.4 W/s 365 nm UV (Omnicure s1000) for 1, 2, 3, 4, and 5 s from 3 cm distance and incubated at 37 °C, 5%CO_2 incubator. Live dead analysis was performed on days 1, 7, 14, and 21.

2.2.6.1.3.4 The Effect of 3D Printing on L929 Fibroblast Viability

GelMA bioink (15 % (v/w) and Irgacure 0.6 % (v/w) in DMEM High Glucose) was prepared, and 3.10^6 cells/mL L929 fibroblast cells were mixed homogenously. Cell-loaded GelMA solution was transferred to a 3D printer syringe at 37 °C. Cell laden GelMA was printed, crosslinked, and cultured for 21 days. Live Dead analysis was performed on Days 1, 7, 14, and 21.

2.2.6.2 Cell Culture and Differentiation Studies

2.2.6.2.1 Adipose-Derived Mesenchymal Stem Cell Culture

Adipose-derived mesenchymal stem cells (ADSC) were expanded with mesenchymal stem cell medium (MSCM) in a poly(L-lysine) coated flask. Poly(L-lysine) coated culture flask was prepared as follows. Poly-L-lysine in sterile-filtered dH_2O (10 mg/ml) was added to the cell culture flask and incubated overnight in a 37°C incubator. The next day, the poly(L-Lysine) solution was aspirated and washed twice with sterile filtered dH_2O. The aspirated poly(L-Lysine) solution was used up to 4 times. MSCM medium was prepared according to the manufacturer's protocol. Basal medium, FBS, mesenchymal stem cell

growth supplement, and P/S was mixed. The medium was changed every day. After reaching confluency, ADSCs were detached from the culture flask by incubating with Trypsin EDTA Solution C (0.05%), EDTA (0.02%) solution for 5 min. Subsequently, the MSCM medium was added to the flask to terminate trypsin activity. Finally, the cell suspension was resuspended in the culture medium. The cells were counted by NucleoCounter (Chemo-Metec, Denmark). Passages between 1 and 6 were used during the experiments.

2.2.6.2.2 Adipogenic Differentiation of Adipose-Derived Mesenchymal Stem Cells

ADSCs were cultured in a poly-L-lysine coated culture flask or TCPS with mesenchymal stem cell medium (MSCM) until 90% confluency. Then, the MSCM medium was replaced with the mesenchymal stem cell adipogenic differentiation medium (MADM). MADM was prepared according to the manufacturer's protocol which included basal medium, mesenchymal stem cell adipogenic differentiation supplement, FBS, and P/S. Adipogenic differentiation of ADSCs started on the day medium was changed, and this day was mentioned as differentiation day 1. After that, the differentiation medium was replaced every four days. After reaching confluency, adipocytes were detached from the culture flask by incubating with Trypsin EDTA Solution C (0.05%), EDTA (0.02%) solution for 5 min. Subsequently, MADM medium was added to the flask to terminate trypsin activity. Finally, the cell suspension was resuspended in the MADM medium. The cells were counted by NucleoCounter (Chemo-Metec, Denmark). Passages between 1 and 8 were used in the experiments.

2.2.6.2.3 The Effect of Differentiation Duration on Adipogenic Differentiation

Confluent ADSCs were cultured in MADM for 21 days to measure adipogenic differentiation rate. In addition, LipidTOX-DAPI staining was performed on days 0, 1, 7, 14, and 21 to monitor the formation of intracellular lipid droplets during adipogenic differentiation. Cell nuclei with and without surrounding lipid droplets were counted via ImageJ software and calculated with the formula below.

$$\text{Adipogenic Differentiation (\%)} = \frac{\text{Number of differentiated cells}}{\text{Total number of cells}} \text{x} 100 \quad \textbf{(11)}$$

2.2.6.2.4 Human Dermal Fibroblast Cell Culture

Primary human dermal fibroblast cells from adult human skin (DF) and fibroblast medium (FM) were obtained from ScienceCell. DF medium was prepared according to the manufacturer's protocol. FM medium includes FBS, fibroblast growth supplement (FGS), and P/S to the basal medium. After reaching confluency, DF cells were washed with PBS and were detached from the culture flask by incubating with trypsin EDTA solution C (0.05 % Trypsin, 0.02 % EDTA in DPBS) at 37°C for 5 minutes and centrifuged at 3000 rpm for 5 min. Passages between 2 and 6 were used during the experiments.

2.2.6.2.5 Isolation and Culturing of Keratinocytes from Human Skin

Keratinocytes (KCs) were isolated from skin biopsy specimens of abdominoplasty patients at Medicana International Hospital, Ankara, Turkey, after ethical committee approval (2018-FEN-052). In addition, patients were informed and consent from 3 female patients undergoing elective plastic surgery were taken.

Split thickness skin was obtained from abdominoplasty patients and transferred to the laboratory under aseptic conditions. Samples were stored in PBS containing amphotericin B (0.625 µg/mL), penicillin/streptomycin solution (P/S, 10 mL/L) stored at +4°C until use. Keratinocyte isolation was performed the following day after harvesting. Split thickness was cut into 5 mm x 10 mm pieces. Cut pieces were stored into Trypsin (0.1 w/v, 15 mL) and incubated overnight at +4°C. Enzymatic activity was stopped by adding medium onto the petri dish with the dermal side down cut pieces. The outermost epidermis layer was peeled off with sterile forceps. KCs were scrapped from the bottom part of the epidermis and top of the dermis layer with a scalpel (No. 22). KCs were then resuspended in keratinocyte media (Dmem High Glucose: FBS 9:1 supplemented with 0.0001 µL/mL epidermal growth factor (EGF), 0.0005 µL/mL hydrocortisone, 0.000028 µL/mL cholera toxin) and centrifuged at 10,000 rpm for 5 min. Freshly isolated KCs were seeded on poly-l-lysine coated culture flasks in KC Media and cultivated until confluency. Passages between 2-7 were used.

2.2.6.3 **Optimization Studies on the Different Layers**

The Effect of PCL Pattern on KC Growth and Scaffold Coverage

The effect of PCL pattern on cell adhesion was tested on a film membrane, 3D printed horizontal mesh, and 3D printed strand-shifted wave mesh. In addition, PCL constructs were coated with the Coating Matrix Kit (Gibco ™) to enhance the growth of human KCs. Coating matrix used was sterile 1 % (v/v, in a dilution medium) recombinant human Type-1 collagen On each construct, 5.10^5 KCs were seeded and incubated with KC Media at 37°C incubator. The live-dead assay was performed on days 1, 7, and 14.

2.2.6.3.1 Keratinocyte Differentiation at the Air-Liquid Interface

$5x10^5$ KCs per sample were seeded on strand-shifted wave construct which were collagen coated using Coating Matrix Kit (**Figure 2.2)** and cultured for a week until they covered the surface of the construct. Keratinocytes were differentiated by the air-liquid interface (ALI) to mimic the epidermal stratification (Mak et al., 1991). Cell-seeded constructs were transferred into transwell inserts in a 12-well-plate to initiate ALI **(Figure 2.3)**. Constructs were maintained and cultured in inserts for 14 days at 37°C incubator. The medium was changed every 2 days.

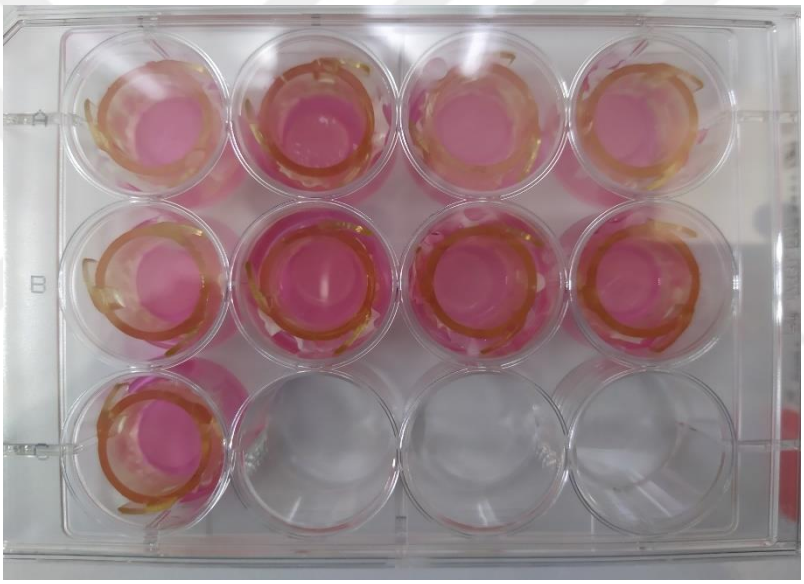

Figure 2.3. Air-Liquid Interface of Keratinocytes. 3D Printed PLC polymer scaffold was coated with a collagen matrix, and keratinocytes were seeded on it. After seven days of culture, the scaffold was transferred into ALI inserts and cultured for another 14 days.

2.2.6.4 Co-culture Conditions for Cell Types in Full Construct

2.2.6.4.1 Determining The Differentiation Medium Ratio for Adipogenic Differentiation

Various volume ratios of MADM and DMEM High Glucose (100:0, 75:25, 50:50, 25:75, 0:100) were used to study the behavior of ADSC monolayers in different medium conditions in 48 well plates. This experiment was performed as the first step for finding the mutual media for cell types used in our skin model. Initially, ADSCs were cultured in MADM for 7 and 14 days for adipogenic differentiation. The medium was changed every three days. After the initial differentiation period, the medium was changed to MADM: DMEM High Glucose volume ratios. The medium was changed every day. Lipid positive cell number was determined by LipidTOX- DAPI staining on days 0, 1, 7, and 14 for each medium composition. Nuclei with surrounding lipid droplets were counted as differentiated. Cell nuclei and differentiated cells were counted by ImageJ Cell Counter. The differentiation ratio was calculated with the following formula:

$$\text{Differentiation (\%)} = \frac{\text{number of differentiated cell nuclei}}{\text{Total number of cell nuclei}} \times 100 \quad \textbf{(12)}$$

2.2.6.4.2 Determining The Optimum Medium Composition for Cocultures

Co-cultures of ADSCs, DFs, and adipocytes were tested in 2D culture for finding the optimal co-culture medium composition**.** Co-cultures were used to reflect the cell population differences between dermis and hypodermis layers. For the dermis layer, a ratio of 3:1 (DF: ADSC) was prepared. For the hypodermis layer, ADSCs were differentiated into adipocytes for 14 days in the TCPS. The ratio for the

hypodermis layer (DF: adipogenic differentiated ADSCs) was 1:3. Differentiated ADSCs included differentiated ADSC (adipocytes) and undifferentiated ADSC together. Media compositions are listed in Table 2.1. Cells were seeded on a 48-well plate at a density of 30.000 cells/well. Controls were self-media (DF-DF media, ADSC-MSCM, 3:1 and 1:3 cocultures- DMEM High Glucose) (n=3). The viability and proliferation of cells were measured with the Alamar Blue Viability assay.

Table 2.1 Media compositions for Alamar Blue Assay

	MSCM (%)	MADM (%)	DMEM (%)
A	25	25	50
B	50	25	25
C	25	50	25
D	50	50	-

2.2.6.4.2.1 Alamar Blue Viability Assay

Alamar blue solution was prepared (89% (v/v) DMEM High Glucose Colorless Media, 1% P/S (v/v) and 10% (v/v) Alamar Blue). Alamar blue solution with the volume of 450 µl/well was transferred into assay plates and incubated for 90 minutes. 200 µl/well Alamar solution was transferred into black bottom 96-well plates as duplicates, and fluorescence was measured with the excitation wavelength of 560 nm and an emission wavelength of 590 nm. Each medium type had three replica wells with duplicates (n=6). The percent viability of cells at different medium compositions was calculated as follows:

$$\text{Viability (\%)} = \frac{\text{(Fl 590- Fl 590 blank)-(Fl 590 Self Media-Fl 590 blank)}}{\text{(Fl 590 untreated-Fl 590 blank)}} \text{ x } 100 \quad \textbf{(13)}$$

2.2.6.4.2.2 Immunohistochemical Characterization of ALI Culture

KC ALI samples were fixed in paraformaldehyde solution (4% in PBS (v/v)) (PFA) for 30 min and rinsed twice with PBS. Then, the cells were permeabilized with 1 % Triton X-100 in PBS at ambient temperature for 15 min. The samples were blocked with 1% BSA diluted in PBS for 1 h and then incubated with anti-wide spectrum Cytokeratin antibody (ab9377) overnight at +4°C. Then, the samples were incubated with the secondary antibodies of anti-goat Alexa 488 and Alexa 647 in 0.1 % BSA (1:250) for 1 h at ambient temperature. Then, nuclear staining was performed using DAPI. DAPI (1:1000) stain was added and samples were incubated at ambient temperature for 15 min. Cell imaging was performed with Zeiss LSM 800 Confocal Laser Scanning Microscope (Germany).

2.2.6.5 3D Printing of Cell-Laden Dermal and Hypodermal GelMA Scaffolds

Bioink preparation, printing, and irradiation conditions are mentioned in Section 2.2.3. GelMA bioinks for hypodermis and dermis were prepared using a cell density of $3x10^6$ cells/mL. Dermis bioink consists of DF: ADSC at a volume ratio of 3:1. Hypodermis bioink contained DF: ADSC at a ratio of 1:3. Bioinks were heated to 37°C and poured into the printer's cartridges (EnvisionTech, Bioplotter, Germany). Cartridges were loaded to the print head and incubated for 30 min. Cell-loaded bioinks were printed into sterile ultra-low adhesive 12 well-plates. 24 G steel nozzle with 0.33 mm inner diameter was used. Scafffolds were composed of 4 layers. The thickness of the scaffold was 1.06± 0.24 mm. Printing parameters were 40 mm/ s speed abd 0.3 bar extrusion pressure at 37°C on the 15°C platform. The ambient temperature was adjusted to 24°C. Subsequently, printed hypodermis and dermis layers were irradiated with UV for 4s. Printed scaffolds were then transferred to a sterile plate in the laminar flow hood. For both hypodermis and

dermis layers, media composed of 50 % MADM and 50% MSCM were added and incubated at 37 °C in a CO_2 in incubator (5%).

2.2.6.6 **Characterization of 3D Cocultures**

Cell-free and cell-loaded PLC and GelMA scaffolds were examined with environmental SEM (ESEM) at 20 kV, 609 PA, and 1.7 °C without gold coating on day 14. The live-dead assay was conducted on days 1, 7, 14, 21 as described in Section 2.2.6.4. Live and dead cell numbers were counted from CLSM images (n=3) using ImageJ software, and viability was calculated according to Formula 12. Scaffolds were fixed with paraformaldehyde and blocked with 1% (v/v) in PBS for 1 h at 37 °C. Subsequently, scaffolds were stained with Alexa fluor 488 Phalloidin and DAPI and imaged using CLSM with 405 nm and 488 nm lasers.

2.2.6.7 **Microbioreactor Design and Production**

The skin chip was fabricated from poly(methyl methacrylate) (PMMA). PMMA layers were sealed with a double-sided adhesive (DSA). PMMA layers and DSA were modeled in computer-aided design (CAD) software (CoralDraw X8) and produced using a laser cutter (Universal Laser Systems, US). 4 external silicone tubings (Instech, US) were inserted into the chip as inlet and outlet fluid flow channels. One channel pair was used for medium feeding and waste. Another tubing pair was used for the PBS inlet and outlet to test the drug concentrations.

The chip is comprised of three chambers one each for the epidermis, dermis, and hypodermis, which were made up of five layers of microstructured PMMA, as shown in **Figure 2.4**. PMMA microstructure was designed in CAD program and laser-cutted. PMMA layers were made to be 1.97 mm thick and 25 mm in length. Tubings were dividing each layer with a fluid channel pattern in half. Tubings provide medium feeding into the middle of the layers, where scaffolds were inserted. A commercial glue affixed them to prevent the fluid leakage.

From top to bottom, the first layer of the chip has a hole 6 mm radius and was designed to provide an air-liquid interface area for keratinocytes. The second layer

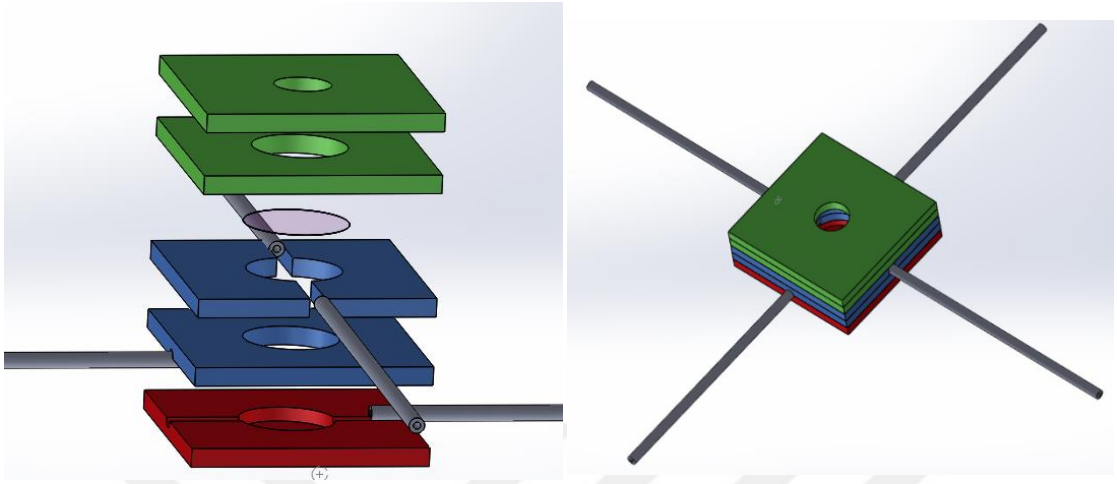

has a wider 10 mm radius gap and acts as a chamber for the keratinocyte-seeded 3D printed PLA epidermis layer. A 1.2 μm pore-sized membrane filter (Isopore, Millipore, Merck, Germany) was sandwiched between the second and third layers of the chip to hold the keratinocyte layer up and block keratinocyte migration. In addition, a 10 mm radius-sized chamber exists in the third and fourth layers to hold dermis and hypodermis layers. The third layer was divided by a space into two pieces where tubing (1.65 mm) could fit. The fourth and fifth layers had half channels from each side where the drug was collected. Finally, the fifth and deepest layer was engraved with the laser cutter (0.8 mm) in the middle to make a hollow so the whole construct could place and stay still.

Figure 2.4. Representative design of disassembled *(left)* and assembled *(right)* full-chip. Green shows the epidermis chamber, blue is for the dermis, and red is for the hypodermis. The design was made using SolidWorks 2018 software. Lila shows membrane filter and tubing were colored in grey. Upper tubing was used as medium inlets and outlets. Inlet tubing is connected to syringe pump dispensing the growth medium, and outlet is connected to waste container. The tubing at the bottom is for PBS flow. Inlet is connected to the syringe pump. The outlet is connected to a collection tube which drug concentrations were measured.

The top chamber was left open to continue ALI and keratinocyte differentiation throughout the experiments. The middle chamber provides media exchange, and the bottom chamber was used for the drug readout channel. The media flow through microfluidic parts supplies continuous nutrients, and waste removal shows

similarity to blood vessels of native skin. All the experiments were conducted as triplicates simultaneously (n=3), reducing the time needed to provide multiple circumstances using multiple injections. This method allows switching flow conditions or drug applications without disturbing the skin model. Here, we designed a functional, easily monitored, tunable testing device for combinatorial drug applications.

2.2.7 Computational Fluid Dynamic Modelling of The Microfluidic Platform

Computational Fluid Dynamics (CFD) analysis was performed to evaluate the effect of the velocity profile and shear stress of the cell culture medium in the microfluidic platform. Reynolds number (Re) in the microfluidic platform was calculated according to Eq 13:

$$Re=\frac{QDhp}{\mu A} \quad \textbf{(14)}$$

Q is the volumetric flow rate, Dh is the hydraulic diameter of the tube, ρ is the fluid density, μ is the dynamic viscosity of the fluid, and A is the cross-sectional area of the tube.

The fluid density and dynamic viscosity at 37°C are 1000 kg m^{-3} and 0.000692 kg m^{-1} s^{-1}, respectively. Flow Dynamics of the cell culture medium was explained using time dependent Navier-Stokes equations. In this study, the cell culture medium was accepted to be incompressible and homogeneous with Newtonian behavior. For this reason, non-Newtonian effects were neglected. In the Stokes stream, the shear stress in the middle of the channel is calculated according to Eq. 15.

$$T=\frac{6\mu Q}{h^2 w} \quad \textbf{(15)}$$

No-slip boundary conditions were accepted in the microfluidic channel and a computational fluid dynamics model using the finite element method COMSOL MultiphysicsTM 5.2a was used to evaluate the local wall shear stress distribution.

2.2.7.1 **Dynamic and Static Culture of 3D Printed Scaffolds**

The chip of the microbioreactor described above was used for static and dynamic cultures. The cell-free and cell-loaded epidermis, dermis, and hypodermis were inserted into chips to understand the effect of cells in the skin model. Dermis and epidermis constructs were placed into the middle chamber. Epidermis scaffold was placed into the top chamber, which forms the ALI. The middle chamber was perfused with growth media. The flow rate was 3.33 μL/min. The syringe pump was programmed for continuous flow **(Figure 2.5)**.

A static chip was built by the dermis, and hypodermis layers were placed into the middle chamber as a control. The system was primed with growth media, and priming was repeated every 48 h.

There was also a control group in 48 healthy plates without the microbioreactor setup. The dynamic and static culture was conducted for 4 d. Live dead assays were performed on days 1 and 4 according to the protocol mentioned above and imaging was performed with Zeiss LSM 800 Confocal Laser Scanning Microscope and Zeiss LSM 800 fluorescence module.

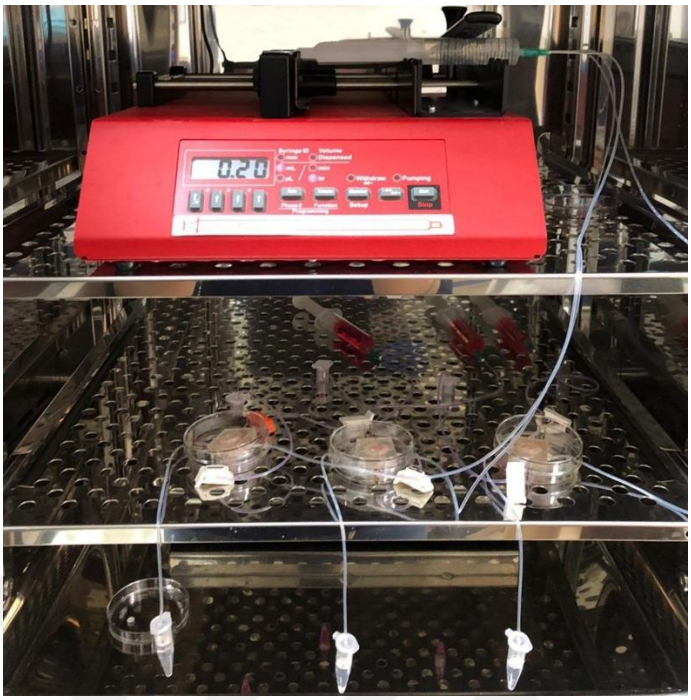

Figure 2.5. Organ-on-a-Chip system fed by syringe pump for drug penetration assay.

2.2.8 **Drug Penetration Tests**

2.2.8.1 **Dexamethasone *In Vitro* Experiments**

10,000 cells/well keratinocyte cells were seeded on a 96 well plate. After the first day of incubation, cells were treated with 100 µM, 10 µM, 1 µM, 0.1 µM, 0.01 µM, and 0.001 µM dexamethasone (DEX) in growth media for 2, 4, 8, and 12 hours. Alamar Blue Viability assay was performed on keratinocytes. The viability of the cells was calculated according to Formula 12.

In the second group, cells were treated with Fluorescein isothiocyanate (FITC) conjugated dexamethasone (DEX-FITC), washed, and FITC fluorescence was measured, then CLSM images were taken. 10^3 cells/well were incubated with FITC-DEX in 96 well plates. 96-well plate was washed with colorless media, and FITC signal was measured with 488 nm excitation and 525 nm emission with the

bottom reading mode of spectrofluorometer at 2, 4, 8, 12 h. FITC intensity was calculated for each drug concentration by taking the average and standard deviation of 3 wells. FITC-DEX treated keratinocytes in 96 well plates were fixed with paraformaldehyde (4% in PBS) and stained with DAPI (15 min at 37 °C). Confocal imaging was performed with Zeiss LSM 800 Confocal Laser Scanning Microscope (Germany) with 405 nm laser for DAPI and 488 nm laser for FITC-DEX.

2.2.8.2 **Drug Penetration on Chip**

Drug penetration assays were performed on cell-free, and cell-loaded 3D printed constructs to understand the effect of the dexamethasone uptake on cells. Also, assays were performed with 2 layered and 3 layered constructs to specify the contribution of the barrier properties on the epidermis layer of the chip. All chip experiments were performed inside a CO_2 incubator (5%, 37 °C).

For cell-free constructs, 100 µL of 10 µM Dex-FITC was added to the top side from the ALI of the chip. During drug penetration experiments, middle reservoir growth media feed was clamped to stop the flow. The bottom (readout channel) reservoir was fed with PBS 3.33 µL/min via a syringe pump. PBS was collected hourly for 9 hours. Then, PBS was collected overnight and measured on 16^{th} and 24^{th} h. The fluorescence of the collected PBS-Dex-FITC solutions was measured 488 nm excitation and 580 nm emission in the black bottom 96 well plates. Experiments were repeated for 3D printed and 14 d cultured hypodermis, dermis layers, and in 3 layers experiments with 14 d ALI epidermis layers. At the end of the experiments, constructs were freed from the chips and imaged with Zeiss LSM 800 Confocal Laser Scanning Microscope (CLSM) (Germany) with 405 nm laser for DAPI and 488 nm laser FITC-Dex.

2.2.9 **Statistical Analysis**

Statistical analysis was conducted using Graph Pad Prism 8. For samples of n=2 t test was used. Samples with more than 2 samples types either One-way ANOVA (one independent variable such as time or growth media type) or Two-way ANOVA (two independent variable such as time and media type together) was used. Tukey's post hoc analysis was used to compare samples with one another. The results were presented according to significance of p values (ns $p > 0.0032$, * $p \leq 0.0032$, ** $p \leq 0.0021$, *** $p \leq 0.0002$, **** $p \leq 0.0001$).

CHAPTER 3

RESULTS & DISCUSSION

3.1 Characterization Of Dermal and Hypodermal Layers of The Skin Model

3.1.1 NMR Spectra of Gelatin and GelMA

GelMA was synthesized methacrylolyl substitution of gelatin's lysine residues. Methacrylic anhydride monomers were reacted with amino lysine, and hydroxylysine groups of gelatin and methacryloyl substitution started (Van Den Bulcke et al., 2000) **(Figure 3.1)**. The degree of methacrylation (DM) was defined as the ratio of hydroxyl substituted amino groups of gelatin (lysine, hydroxylysine) to the total amino groups of unmodified gelatin. DM of GelMA was calculated by NMR spectroscopy. The peak of methylene lysine protons at 2.85 ppm appeared in the spectra was low for GelMA, indicating the high substitution of lysine with methacrylic anhydride (Shirahama et al., 2016). DM of GelMA was higher than 85%, which corresponds to high degrees of substitution with methacrylic anhydride (Jason W. Nichol et al., 2010). Acrylamide double bond incorporation, which is necessary for photopolymerization of GelMA, can be seen at peaks at 5.3, and 5.6 ppm. A peak also validated high DM at 1.9 ppm, which indicates methyl protons of methacrylamide **(Figure 3.2)**.

The photopolymerazition reaction can be defined as free-radical polymerization by the photochemical reaction initiation, propagation and termination which results with polymer formation (Eibel et al., 2018). When UV is applied on IrgaCure solution, IrgaCure releases free radical. This free radical has tendency to open double bond of GelMA and bind two GelMA monomers. Binding to GelMA

molecule is preferable due to well water solubility, lower steric hinderance. High free radical production by the UV irradiation of IrgaCure provides photopolymerization to GelMA (Eibel et al., 2018).

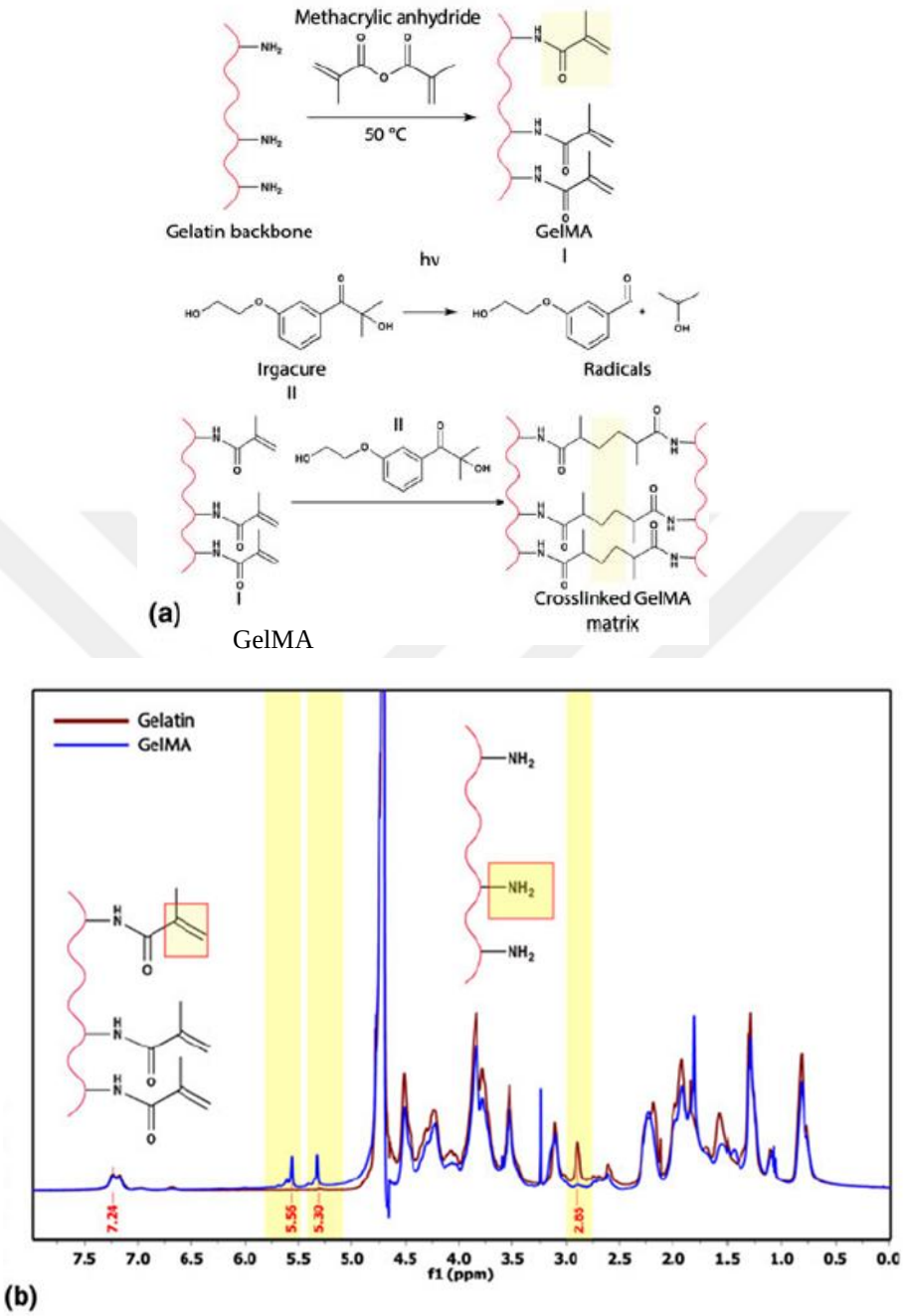

Figure 3.1.GelMA, gelatin and UV crosslinked GelMA synthesis scheme, and nuclear magnetic resonance analysis. (a) GelMA synthesis and photoinitiator reaction mechanism scheme. (b) Nuclear magnetic resonance analysis of gelatin and GelMA (Ermis, 2020)

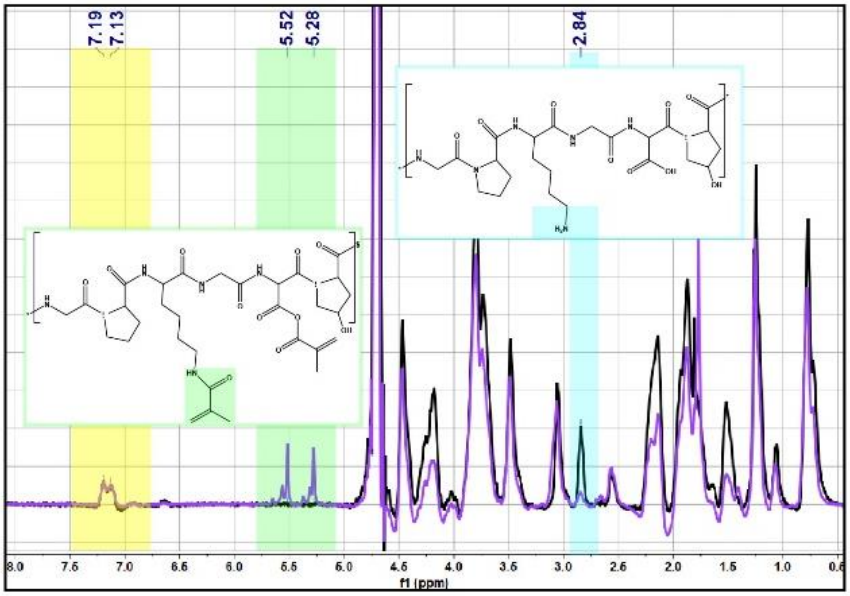

Figure 3.2. NMR spectra of gelatin and GelMA. The purple line indicates GelMA, and the black line shows gelatin.

3.1.2 **Fourier transform Infrared Spectroscopy (FTIR) of GelMA**

Fourier-transform infrared spectroscopy (FTIR) was performed to characterize different chemical groups in gelatin, GelMA, and 4 s cross-linked GelMA **(Figure 3.3)**. All samples showed a broad peak around 3300, which corresponds to the ester (OH-stretching), and vinyl (CH-stretching) bands(Martineau et al., 2005; M. Sun et al., 2018). The 1640 peak corresponds to the amide I (OH-stretching) and 1525 to the amide II (CN-stretching and NH-bending) of gelatin. (Kong & Yu, 2007). A slight shift occurs at the Amide I and II peaks to higher frequencies during methacrylation of gelatin (Modaresifar et al., 2018). This shift is lost after cross-linking of GelMA.

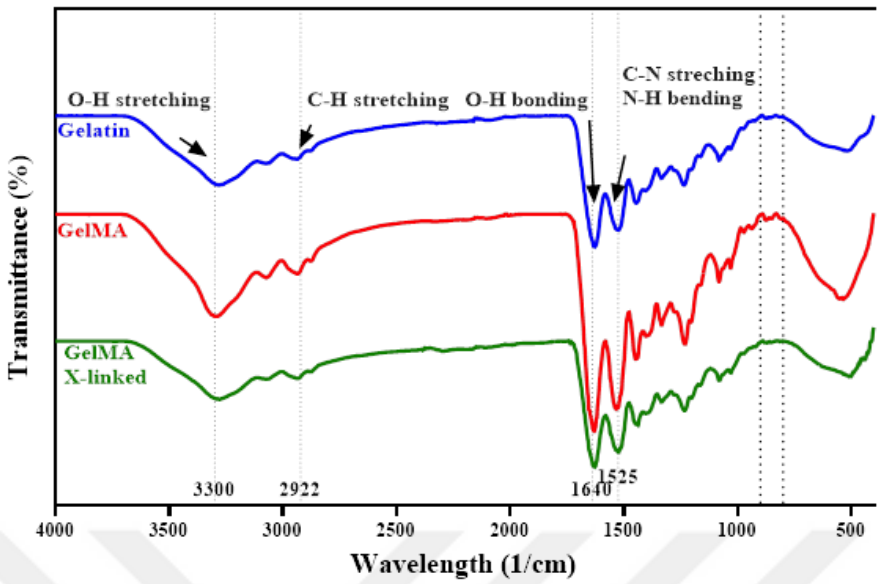

Figure 3.3. FTIR spectra of gelatin, GelMA, and crosslinked GelMA (after hydrogel formation). The purple line indicates Gelatin, red line is GelMA, and the green line shows UV-crosslinked GelMA.

3.1.3 Determining GelMA and Photocrosslinker Concentrations

The physical and biochemical properties of hydrogels majorly depend on their compositions. In the presence of a photoinitiator, GelMA undergoes radical polymerization with UV light exposure and forms a covalently cross-linked hydrogel. Photocrosslinkers are light-reactive ingredients, and when they are exposed to a specific wavelength of light, they absorb the energy and form radicals., convert liquid prepolymer solutions to the polymer networks (Yue et al., 2015). In order to find optimum GelMA and photocrosslinker (IrgaCure) amount, preliminary experiments were performed using different concentrations **(Table 3.1)**. Swelling, water content, and Young's Modulus of the GelMA hydrogels were studied to choose the ideal GelMA (10, 15, 20 % (w/v)), and photoinitiator (0.3, 0.6, 1 % (w/v)) concentrations. 4 s irradiation duration was used in this experiment because the most feasible hydrogel with the lowest irradiation time was fabricated with 4 s UV irradiation (data not shown). Water content analysis was performed to

foresee the effect of GelMA and IrgaCure concentrations on GelMA's sorption properties **(Figure 3.4)**. It was found that increasing GelMA and IrgaCure concentrations led to reduced water content and swelling properties, likely due to the increasing cross-linking density limiting the swelling capabilities of GelMA (Noshadi et al., 2017). 10% GelMA showed significantly higher swelling and water uptake capabilities, whereas 20% GelMA showed the lowest value as expected. Increasing GelMA in polymer solution increased the density of hydrogels and hindered hydrogels' swelling (X. Li et al., 2016). Changing the IrgaCure concentration did not affect swelling or water content significantly in this experiment. This may be because of comparing IrgaCure values low and close to each other. In this thesis IrgaCure concentrations of 0.3, 0.6 and 1 % (w/v) and GelMA concentrations of 10, 15, 20% (w/v) were used. According to the literature, increasing IrgaCure concentrations clearly increases the cross-linking density and decreases the swelling ratio. However, Li et al. compared Irgacure of 0.2, 1, and 5 % (w/v) and %10 GelMA prepolymers and obtained the apparent results. Insufficient amounts of photoinitiator were reported to develop low-crosslinked GelMA polymers in the literature (X. Li et al., 2016).

Table 3.1 GelMA and IrgaCure concentrations used in polymer solution concentration optimization

IrgaCure % (w/v) in PBS	0.3	0.6	1	0.3	0.6	1	0.3	0.6	1
GelMA % (w/v) in PBS	10	10	10	15	15	15	20	20	20

3.1.4 Determining UV Irradiation Duration of GelMA

Irradiation duration was an essential parameter for gel integrity and cell viability. Thus, the concentration of 15 % GelMA and 0.5 % IrgaCure were chosen, and 1, 2,

3, and 4 seconds of UV irradiation was applied on GelMA solutions. As a control, no UV was applied to GelMA solution (0 s). Hydration can have a noticeable effect on the hydrogel's physical characteristics for producing the desired scaffold pattern. It influences the mechanical and surface properties and surface mobility of the resultant hydrogel network (Jason W. Nichol et al., 2010). The ratio of water to GelMA, namely water content, was investigated **(Figure 3.4)**. Hydration properties are determined by the cross-linking density of polymer network, pores, and the interaction between solvent and polymer (Coates et al., 2013; J.W. Nichol & Khademhosseini, 2010). Longer UV exposure durations yield radical polymerization which increases the mechanical strength of GelMA hydrogel (R. Z. Lin et al., 2013). Lowering the cross-linking density provides a higher swelling capacity to GelMA hydrogel (Noshadi et al., 2017). In parallel to literature, 0 and 1 s irradiated samples deteriorated in PBS at 37°C concisely. Increasing cross-linking durations followed a decreasing trend in water content. 2 and 3 s irradiation resulted in higher water content in 72 compared to higher cross-linked groups (4 and 5 s) at all time points **(Figure 3.4 A, *left panel*)**. 2 s irradiated group had significantly higher water content among all irradiation durations **(Figure 3.4 A, *left panel*)**. In the literature, increasing cross-linking density of GelMA slowed down the degradation rate (X. Li et al., 2017). Slow water uptake of 5 s irradiated hydrogels may be attributed to the higher cross-linking density resulting from a more extended time required for reaching equilibrium than 2, 3, and 4 s irradiated samples **(Figure 3.4 B)**. 3 s sample were fragmented during weighing and they were similar to 2, and 3 s irradiated samples in terms of ease of handling. Lower GelMA concentrations led to a significantly higher swelling **(Figure 3.4 C)**. Changing IrgaCure concentrations did not effect swelling sifgnificantly except 48 h data point of 20% GelMA (w/v), 0.6% (w/v) IrgaCure group which may be caused from an experimental error or GelMA concentration becaming high enough for polymerization.

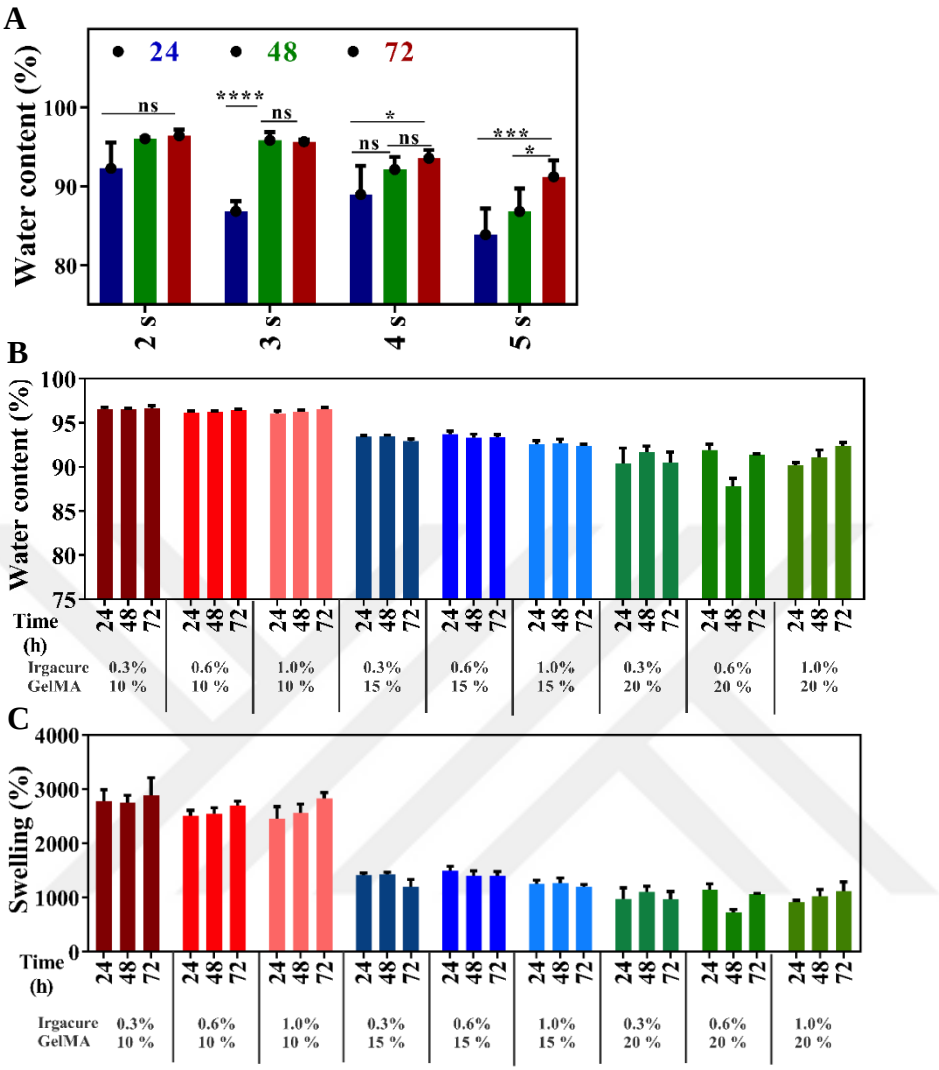

Figure 3.4. Hydration properties of GelMA hydrogels. **A)** Water content of 2, 3, 4 and 5 s UV irradiated GelMA polymers (15% GelMA (w/v) and 0.6% IrgaCure(w/v)) for 24, 48 and 72 h (2 s: Black, 3 s: Green, 4 s: Burgundy 5 s: Purple). Polymers compared within their irradiation duration group (*left panel*), polymers of same irradiation durations were compared with each other (*right panel*).. 4 s was chosen for the UV irradiation time for further experiments (Two-way ANOVA, *p≤0.0332, ** p≤0.0021, *** p≤0.0002, ****p <0.0001). **B)** Water content of changing IrgaCure (0.3, 0.6 and 1% (w/v)) and GelMA (10, 15, and 20% (w/v)) concentrations for 24, 48 and 72 h (Two-way ANOVA, *p≤0.0332, ** p≤0.0021, *** p≤0.0002, ****p <0.0001). **C)** Swelling of of changing IrgaCure (0.3, 0.6 and 1% (w/v)) and GelMA (10, 15, and 20% (w/v)) concentrations for 24, 48 and 72 h. Swelling was the highest at 10% GelMA (w/v) and decreased with increasing GelMA concentrations (Two-way ANOVA, *p≤0.0332, ** p≤0.0021, *** p≤0.0002, ****p <0.0001).

Light cytotoxicity was also performed to find optimal UV-irradiation time **(Figures 3.5 and 3.6)**. L929 cells were cultured and encapsulated in GelMA slabs (15% GelMA (w/v), 0.6% IrgaCure (w/v) in PBS) and cultured for 21 days. Cell viability was measured by counting live and dead cells from CLSM images. Uncrosslinked cell-loaded polymer solution (0 s) lost integrity on Day 0, and 1, 2 s irradiated gels degraded on day 14. The 14 d 3 s group showed 83.34±2.52 % viability compared to 97.3±1.07% in the 4 s irradiated group. Between 3 and 4 s irradiation duration, 4 s was selected considering the high viability. Studies have proven the cell toxicity is caused by the free radicals produced by photoinitiators after irradiation (Wilkens et al., 2016). Also, heat formation by extended UV irradiation durations can be another cause of death. Nevertheless, Monterio et al. showed that short time exposure to UV light did not cause significant long-term damage to the cells (Monteiro et al., 2018). Live-dead staining was in agreement with the literature findings. Although 3 and 4 s irradiated samples were not dense for 7 days, cells became confluent at day 14. Lower viability observed in 3 s irradiated group compared to 4 s irradiated group might be caused by less favorable stiffness of the hydrogels by L929 cells due to lower cross-linking. Also, in the literature DFs were shown to increase proliferation significantly with as the stiffness was increased. Regulatory effect of matrix stiffness was shown with various cell types on integrin binding and cytoskeletal reorganization (El-Mohri et al., 2017; Y. Sun et al., 2012).

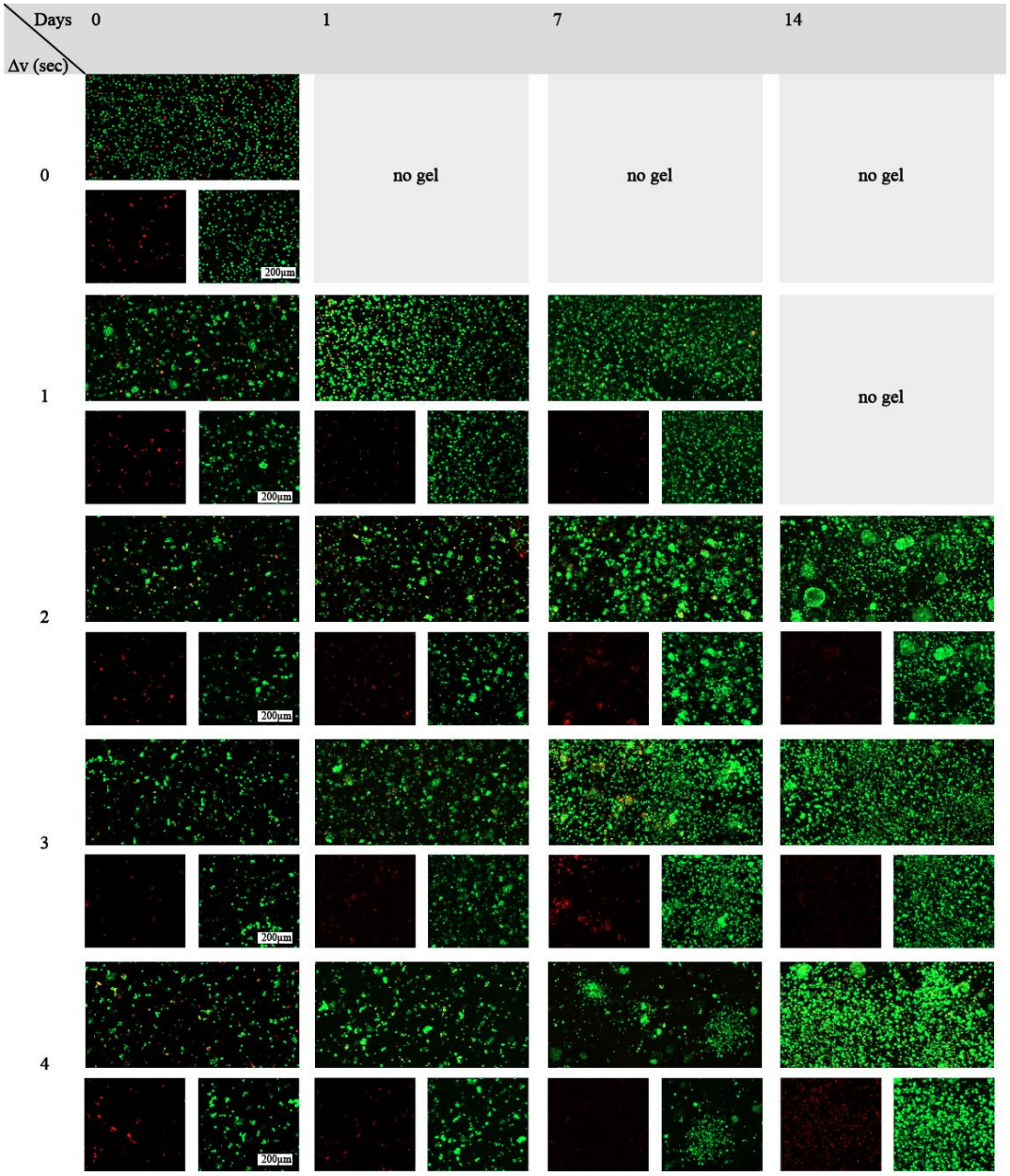

Figure 3.5. Cytotoxicity of L929 cells was tested using live dead staining and CLSM microscopy analysis. Effect of UV irradiation duration was tested on viability of L929 in GelMA polymer solution (15% GelMA (w/v), IrgaCure 0.6% (w/v) in DMEM High Glucose). No UV, 1, 2, 3, and 4 s UV were used. Cells were in GelMA solution. Rectanglular images show overelay of square shaped live (green) and dead (red) images were shown above. 0 s irradiated GelMA solution dissolved completely after day 1. 1 s irradiated GelMA hydrogel was dissolved after day 7. Dissolved gels were shown in the figures as "no gel". 4 s irradiation duration was chosed for the further experiments (Green: Live, Red: Dead, Scale bar: 200 µm).

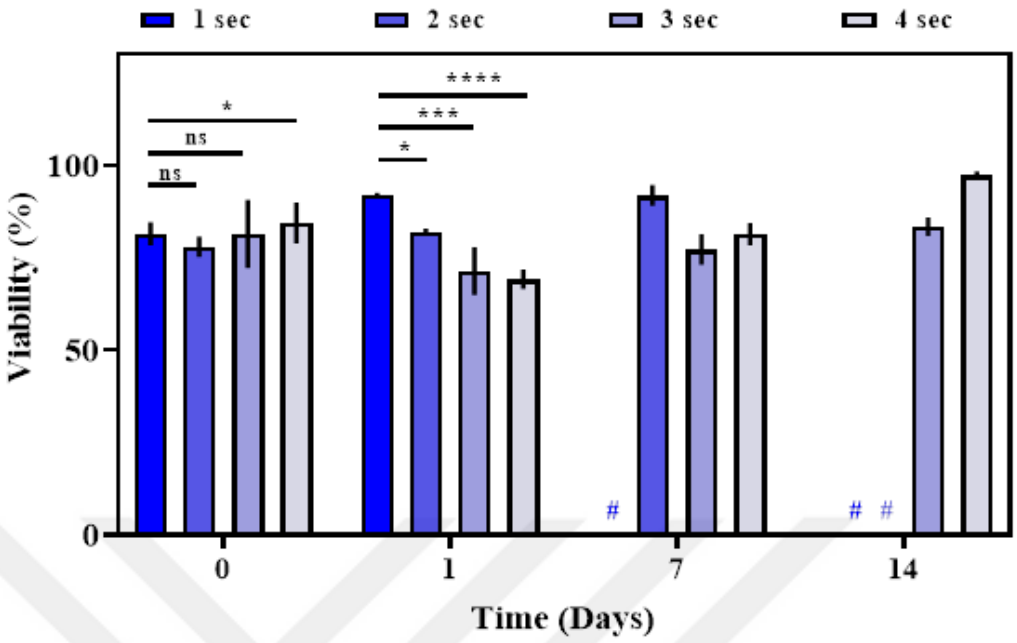

Figure 3.6. Cytotoxicity of L929 cells was tested using live dead staining and CLSM microscopy analysis. Effect of UV irradiation duration was tested on viability of L929 in GelMA polymer solution (15% GelMA (w/v), IrgaCure 0.6% (w/v) in DMEM High Glucose). No UV, 1, 2, 3, and 4 s UV were used and cells were counted from CLSM images (n=3). # shows degraded GelMA. 1 s irradiated GelMA was dissolved on day 7 and 2 s irradiated on day 14. One-Way ANOVA *p≤0.0332, ** p≤0.0021, *** p≤0.0002, ****p <0.0001).

3.1.5 Mechanical Characterization of GelMA

The skin was described as viscoelastic, where the dynamic change between the strain-stress until a stable state is reached (Pereira et al., 1997). The skin has a anisotropic structure. Measured young's moduli are dependent on the employed method. Tensile, indentation, compression, suction, and torsion tests are being employed to find young's modulus of the skin. There are many variations between authors in the literature. Biologic variability between subjects such as age, sex, sampling area, and origin and sensitivity of biological subjects makes it hard to specify one young's module value. Also, excised skin does not reflect the actual values as it is no longer attached to the body (Ní Annaidh et al., 2012). Developing an in vivo skin model that includes anatomical and physiological features is

essential for determining dermatological diseases or calibrating the elasticity of wearable biosensors (Kalra & Lowe, 2016).

A uniaxial compression test was applied on GelMA hydrogels of different concentrations cross-linked with different IrgaCure concentrations. Young's Modulus of all concentrations ranged between 0.065 and 0.636 MPa **(Figure 3.7)**. 10% GelMA had the lowest Young's Modulus. The moduli increased significantly at all concentrations as the GelMA concentration was increased. This phenomenon was supported by the literature. It was reported that the compressive modulus of GelMA hydrogel was directly proportional to the GelMA/volume fraction (Yue et al., 2015). Hydrogels with different modification degrees and GelMA concentrations have been reported to have a Young's Modulus between 0.003 and 0.03 MPa (Jason W. Nichol et al., 2010). In a study, Young's Modulus of 0.03 MPa was reported for 15% GelMA- 0.5 % IrgaCure (w/v) with DM of 80%. The research group reached 0.03 MPa with 10% GelMA hydrogel with %10 higher DM (X. Li et al., 2016, 2017). This implies the importance of batch-to-batch differences during GelMA synthesis. 10% GelMA- 0.6% IrgaCure (w/v) in this study had a Young's Modulus of 0.006 MPa while the other groups reached 0.03 MPa with the same concentration. This difference can be explained by comparing irradiation intensity and duration. Although they have not mentioned UV intensity, they used 5 min cross-linking instead of our 4 s irradiation. IrgaCure concentration had an impact on the mechanical properties only in the 15% GelMA group. 10% group was too soft, and 20% group was very stiff. Cell proliferation was reported to be inversely proportional to GelMA mass fraction within the hydrogel. In the study, cell elongation and migration were compared in 3T3 fibroblast loaded GelMA hydrogels of different concentrations (5, 10, and 1 % (w/v)). Results showed that increasing hydrogel concentration slowed the process but did not inhibit it completely (Jason W. Nichol et al., 2010). Moduli of 15% GelMA kept increasing as the IrgaCure concentration was increased. This may be due to an increase in prepolymer concentration or an increase in the cross-linking density. On the other hand, 20% GelMA concentrations showed lower Young's Modulus with increasing

IrgaCure concentrations. The probability of experimental error was thought, and the experiment was repeated. The same results were obtained. The second trial can be explained by using a different batch of GelMA at the later experiment. The effect of different DMs cannot be neglected in terms of mechanical properties (Chen et al., 2012). Overall published *in vitro* and *in vivo* values for Young's Modulus varied between 0.025 MPa and 140 MPa. Since GelMA was fabricated for soft tissue, dermis, and hypodermis, choosing ~0.4 MPa Young's modulus will meet the need. Water content, swelling, and mechanical tests were considered to choose the most suitable GelMA and IrgaCure bioink concentration for skin dermal and hypodermal layers. %15 GelMA (w/v), 0.6% Irgacure, and 4 s UV irradiation time were selected for further experiments.

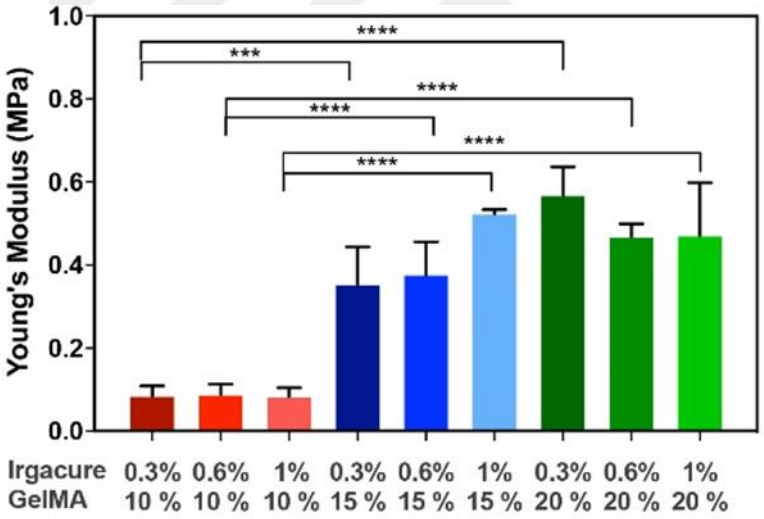

Figure 3.7. Young's moduli of GelMA hydrogels of varying concentrations (10, 15 and 20%, w/v) which were photocrosslinked for 4 s with different Irgacure concentrations (0.3, 0.6, 0.9%, w/v). Uniaxial compression tests were conducted on the GelMA hydrogels. Young's modulus was lowest in the 10% GelMA (w/v) and higher in the 20% GelMA (w/v) group. (Two-way ANOVA, *$p \leq 0.0332$, ** $p \leq 0.0021$, *** $p \leq 0.0002$, ****$p < 0.0001$).

3.2 Characterization of Epidermal Layer of the Skin Model

The skin has an anisotropic viscoelastic structure. It is the outermost barrier of the human skin. The outermost layer of the skin is the epidermis. The epidermis promotes strength and elastic behavior, supports pliability, and resists applied force and stretch (Everett & Sommers, 2013). The skin contains 20% of the body water (Girard et al., 2000) and maintains homeostasis. The overabundance of water within the extracellular matrix can disorganize the arrangement of collagen fiber within the skin and change viscoelastic responses (Everett & Sommers, 2013; Wu et al., 2006). Therefore, soft and highly absorbent hydrogels may not be the best candidates for building the epidermis layer. A highly ductile material, a synthetic biomaterial, would be a good candidate for building up the epidermis layer. In this study, the epidermis layer was fabricated with 3D printing of PLC copolymer.

PLC is a copolymer of L-lactide and ε-Caprolactone in a 70/30 molar ratio. This GMP-grade polymer was in the form of granules. The lactic acid part provides thermoplastic properties, high strength, and high modulus. The addition of thermoplastic Caprolactone enhances ductility, thermal stability, tensile strength, and elongation at break (Nofar et al., 2019). Lactic acid segments of the polymer backbone tend to crystallize. Therefore copolymers reflect semi-crystalline properties (Park et al., 2017).

3.2.1 DSC of PLC

DSC was performed to define the printing parameters of the copolymer. PLC polymer was loaded into the printer head in the granular form and heated to 175 °C and awaited for 1 hour to melt, and heat reaches evenly and precisely in the printing head. After 2 hours of printing, PLC turned to a burned-yellow color each time. After sacrificing yellowish polymer completely, printing could continue for another hour until it becomes yellow again. For this reason; we wanted to check the thermal properties of the polymer. The PLC polymer was analyzed by differential

scanning calorimeter to determine Tg, Tm values before and after printing **(Figure 3.8)**. PLC granules showed prominent glassy transition (Tg) at 17.57°C and melting temperature (Tm) at 110.42 °C. PLC was printed at 175 °C. After printing, DSC was repeated, and results showed that both peaks were shifted to a lower temperature (Tg 15.67 °C, and Tm 103.07 °C). Also, the Tm peak was broadened and decreased in amplitude. This may be explained as either the rearrangement of the polymer chains and decrease in the crystallinity of PLA segments or occurrence of shorter polymer chains because of thermal degradation of PLC resulting in a broad peak at Tm and the peak at around 170°C becoming more evident (Fernández et al., 2012).

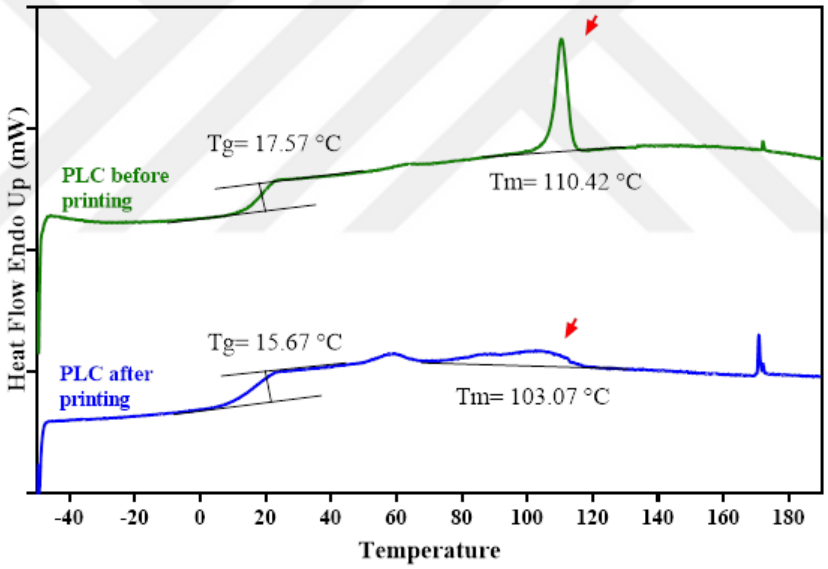

Figure 3.8. DSC thermograms of PLC before (green) and after (blue) printing. Tg and Tm were detected. Tm is shown with red arrows.

3.2.2 Mechanical Characterization of PLC

A uniaxial tension test was performed on 3D printed 4-layered PLC mesh and wave-shifted patterns to define epidermis geometry. Namely, a mesh pattern and a

wave-shift pattern were tested **(Figure 16)**. Waveform also had strand shifts at every two layers to provide a firmer structure. Young's moduli of wave-shift pattern and the 90° mesh were 43.408± 1.074 MPa, and 0.298 ± 0.004, respectively. Wave-shift design increased Young's Modulus by about 150 fold. This result was expected since the wave-shift pattern has more connecting points. Also, wave shape was acting as a spring, and between layers, and as a result holding higher loads. In the literature, for lower porosity with higher mass scaffolds compressive modulus was shown to be higher (Mehendale et al., 2017). In our design, shifted strands have overlapped the pores in the strand after 2 layers, and pore sizes shrunk while the number of pores increased. Theoretically, the lowest scaffold's pores were closed by the shifted upper layers. In literature, mechanical properties of skin extend to a wide range and varying multiple measurement methods (Crichton et al., 2013). For tension tests, available epidermis and dermis region data vary between 17 and 21 MPa depending on the age (Edwards & Marks, 1995). Other mechanical tests data revealed a range between 25 kPa and 140 MPa (Kalra & Lowe, 2016). In a tensile test performed with human cadaver skin (n=33), the mean elastic modulus was found to be 98.97 ±97MPa (Gallagher et al., 2012). Using strand-shifted PLC is suitable for this range. Biomechanical skin properties also change significantly with sex, age, and the skin specimen region (Agache et al., 1980).

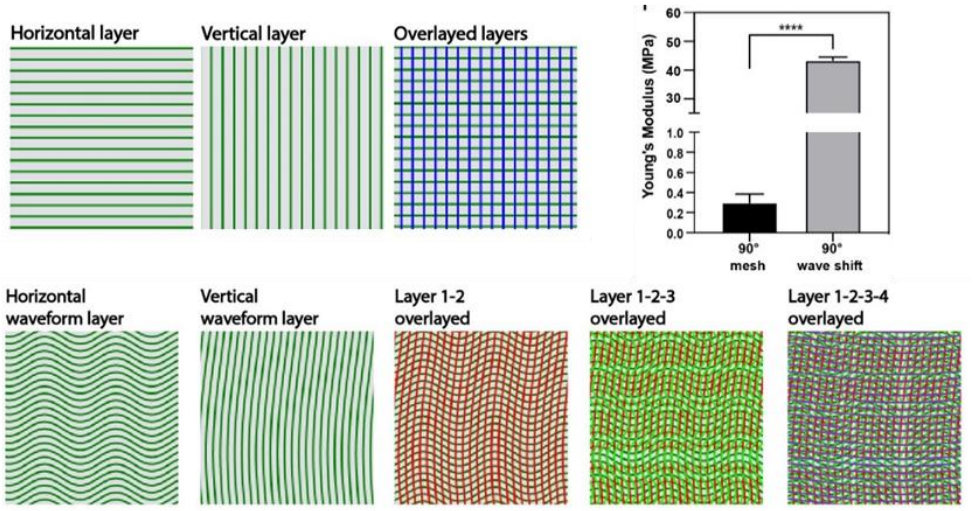

Figure 3.9. Schematic representation of layers of the 3D printed mesh pattern (top) and wave-shift pattern (bottom) PLC scaffolds. Overlaying strands were shifted in all PLC layers to achieve smaller pore size in the bottom layer to decrease cell leakage from the scaffold. Young moduli of 3D printed PLC with 90° mesh, and wave shift geometries (t-test, *p≤0.0332, ** p≤0.0021, *** p≤0.0002, ****p <0.0001).

3.2.3 3D Printing of PLC Scaffold

PLC granules were used, loaded into a 3D printer's cartridge, and melt-extruded via a 3D printer (3D-Bioplotter, Envisiontec). Printing parameters were 8 bars extrusion with 1 mm/s throughout the printing process. Nozzle inner diameter was 0.45 mm.

3.2.4 Scanning Electron Microscope (SEM) of 3D Printed PLC Epidermis Scaffold

SEM images showed the microfiber diameter of PLC scaffolds printed for the epidermis layer was 0.288± 0.021 mm **(Figure 3.10)**. 4 layered final scaffold's thickness was 1.2± 0.3 mm. Between layer shifts, smaller pores occurred. Layer shifted wave pattern mimicked the anisotropic structure of the skin. Keratinocytes may form stratification better with this pattern.

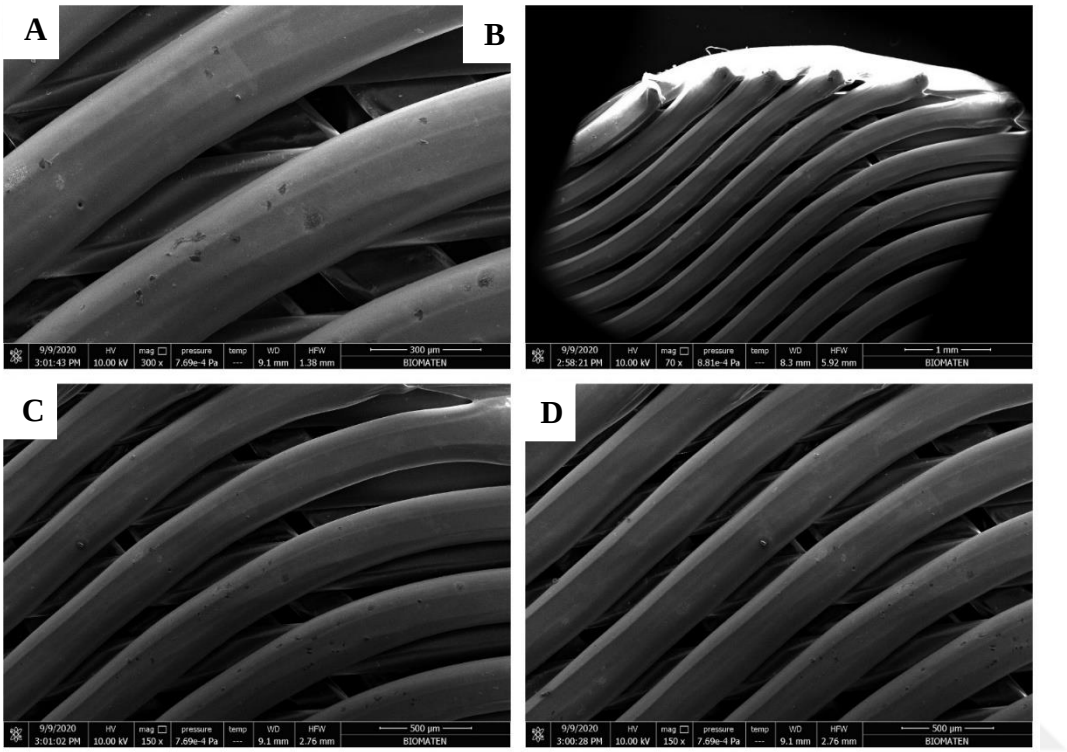

Figure 3.10. SEM Images of 3D printed PLC copolymer. Strand thickness was measured from SEM images and found 0.288± 0.021 mm (n=4) **A)** Scale bar :300 μm, **B)** Scale bar: 1 mm, **C- and D)** Scale bar:500 μm.

3.3 Cytotoxicity Tests of Three Layers of the Skin Model

Cytotoxicity experiments were performed to understand the cytocompatibility of materials (PLC film) and the effect of processing parameters during encapsulation of cells like UV exposure duration in photocrosslinked GelMA slab gels and 3D printed photocrosslinked GelMA hydrogels on cell viability. L929 fibroblast cells were used for the preliminary experiments. Then, optimized gels were tested for cytotoxicity of DF, ADSC, adipocyte cells. Adipocytes were differentiated from ADSCs, as mentioned in Section 2.2.6.2.2. A live-dead assay was performed for 21

days of culture. Cell viability was calculated by counting live and dead cells from CLSM images.

3.3.1 Viability Of L929 Fibroblasts on Solvent Cast and 3D Printed PLC Scaffolds

L929 cells were seeded on TCPS (as control) and solvent-casted PLC film to detect cytotoxicity of the copolymer used in the epidermis layer **(Figure 3.11)**. On day 21, viability was found 97.68 ± 0.88% for TCPS and 98.77±0.44% for PLC film, which were similar values. This GMP grade PLC copolymer provided very high cell viability (97 ± 1.3%) as a scaffold as in the other studies (Tan et al., 2015, 2016).

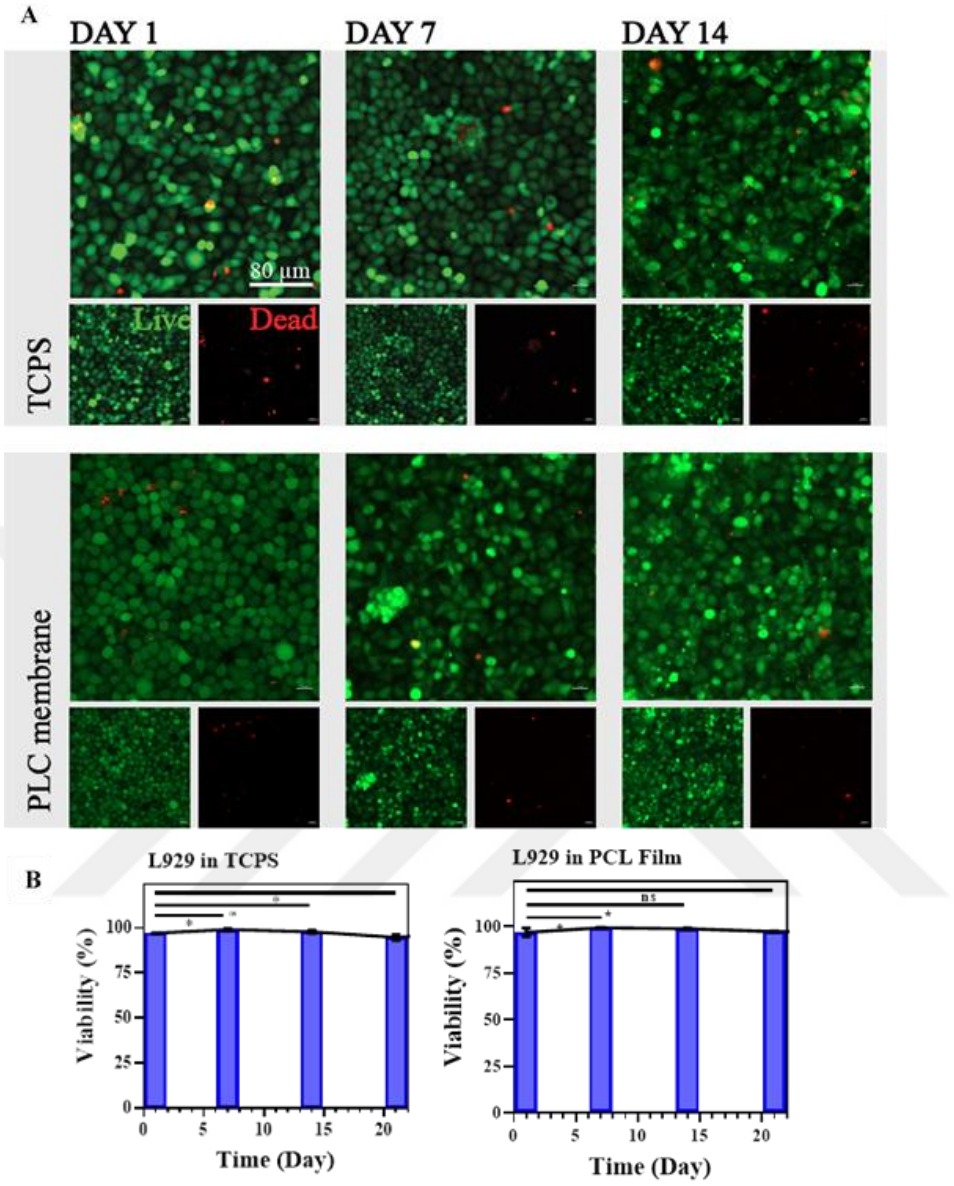

Figure 3.11. Cytotoxicity of PLC and TCPS was performed using live dead staining and CLSM microscopy. **A)** Viability of L929 cells on TCPS (*top panel*), and PLC membrane (*bottom panel*). Live and dead images are given separately above their superimposed images (Green: Live, Red: Dead, Scale bar: 80 µm). **B)** Viability of cells obtained from live dead staining on TCPS (*left panel*), and PLC membrane (*right panel*), (n=3, One-Way ANOVA *p≤0.0332, ** p≤0.0021, *** p≤0.0002, ****p <0.0001).

3.3.2 **Viability of L929, ADSC, Adipocyte, and DF on GelMA Slab Gels**

Cells were encapsulated in GelMA polymer solution (0.6% IrgaCure (w/v), and 15% GelMA (w/v) in DMEM High). The polymer solution was cast into PDMS-coated 48 well plates and irradiated with UV for 4 s. Cell viability assay was repeated for L929, ADSC, adipocyte, and DFs in the GelMA slab gels. Cell-loaded gels were cultured in their growth media for 21 days **(Figures 3.12 and 3.13)**. On seeding day, viability of ADSCs and DFs were higher than adipocytes and cell viability reached up to 90% for each cell type. Lower viability on seeding day may attributed to long tyripsin incubation durations. Also, growth arrest and lower proliferation rate of adipocytes may have affected increasing the number of live cells in the culture. Adipocyte proliferation was at a lower rate compared to ADSCs and DFs. Adipocytes in this study were obtained via ADSCs differentiation- namely adipogenesis. Uncommitted stem cells differentiate into mature adipocytes in the adipogenesis process. Adipogenesis is initiated and sustained by introducing adipogenic hormones. It is accepted as the cells undergo many rounds into the cell cycle and then differentiating into adipocytes (Fajas, 2003). A study showed that cellular proliferation is counteractive to adipogenic commitment in the adipogenesis process (Marquez et al., 2017). The low proliferation rate in adipocyte culture may be explained by growth arrest before terminal differentiation.

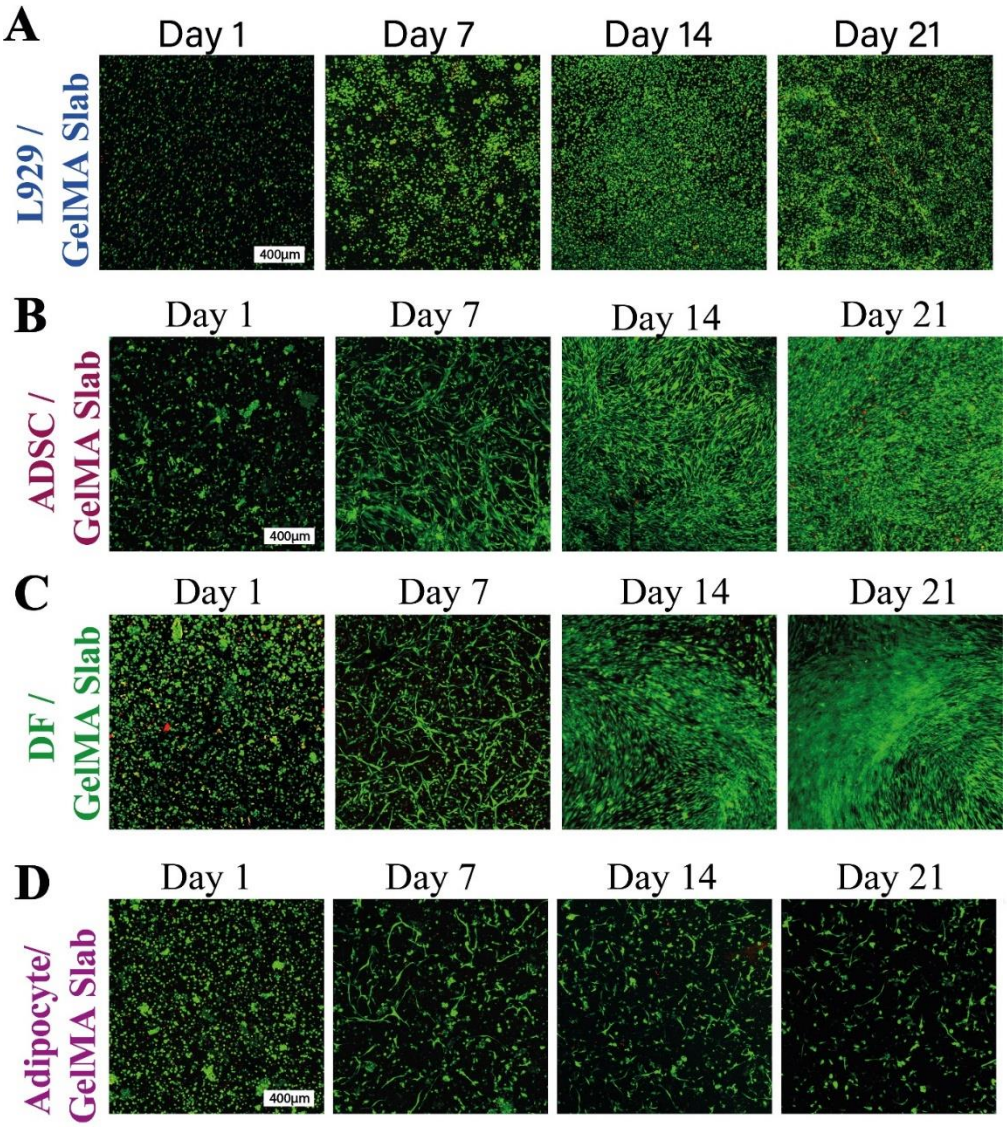

Figure 3.12. L929, ADSC, DF and adipocyte cells encapsulated in GelMA slab gels were analyzed using live dead staining and CLSM microscopy analysis. Confocal images of live **A)** L929 cells **B)** ADSC cells. **C)** DF cells, **D) A**dipocye cells in GelMA slabs, (Green: Live, Red: Dead, Scale bar: 400 µm).

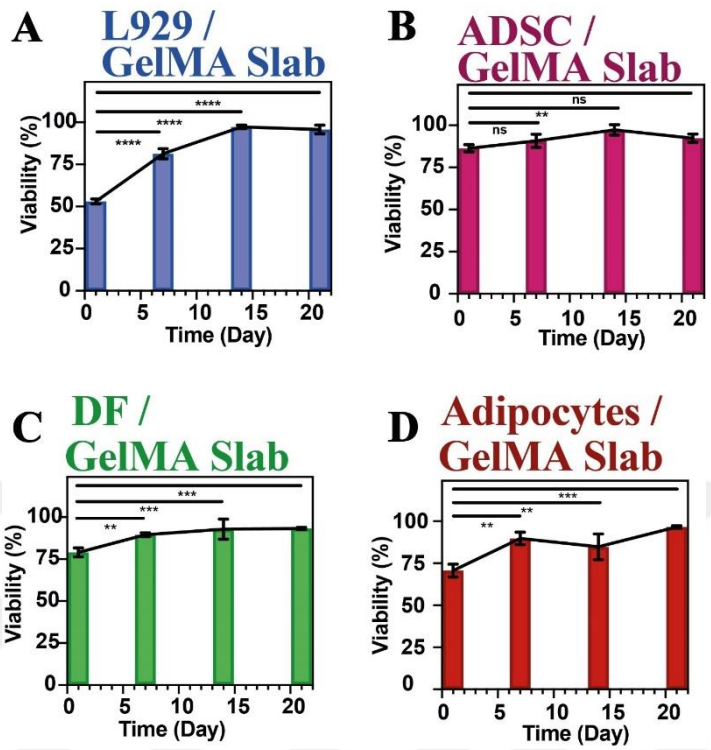

Figure 3.13. Viability of DF cells obtained from live dead staining in GelMA slab gels **A)** L929, **B)** ADSC, **C)** DF and **D)** adipocyte cells encapsulated in GelMA slabs analyzed using live dead staining and CLSM microscopy analysis (n=3, One-Way ANOVA *p≤0.0332, ** p≤0.0021, *** p≤0.0002, ****p <0.0001).

3.3.3 Viability of L929 Fibroblasts In 3D Bioprinted GelMA

The effect of 3D printing on cell viability was tested by comparing L929-encapsulated slabs, and L929 encapsulated 3D printed scaffolds **(Figure 3.14)**. The cell viability observed in L929-loaded GelMA slabs was compared with the viability observed in 3D extrusion bioprinted and UV photocrosslinked L929 encapsulated GelMA scaffolds **(Figure 3.14A)**. Two groups were cultured for 21 days, and the percent of viable cells was calculated from CLSM images **(Figure 3.14B)**. On day 1, viability was slightly lower in 3D printed groups (51.46±5.33 %) than slab (53.02±1.5). The effect of shear stress created by the printer's nozzle may be the reason for it. According to Blaeser et al., shear stress ultimately affects cell behavior. Their findings showed that short time exposure to shear in high levels

may not immediately affect cell behavior but may alter the proliferation potential of cells in the long term. They also suggested that below a specific shear stress threshold (5 kPA for L929 and ADSCs), cells can be printed without side effects (Blaeser et al., 2016). In literature, it is also reported that shear stress induces maturation of megakaryocytes, moderate shear stress was found to induce stem cell differentiation or excessive shear may disrupt cell membranes (Blaeser et al., 2016; Escobar et al., 2020; Potter et al., 2014). Shear could be researched more deeply in this study, but other than the initial low viability obseerved in this experiment, viability was very high overall. Low viability (<70 %) may be caused by an experimental error in this experiment. Although viability of L929 slabs and 3D bioprinted GelMA was similar until day 7, viability of 3D bioprinted did not increased as much as the slab in latter days. These result is similar to a study in the literature (Blaeser et al., 2016). A non-printed ADSCs seeded on glass slides (as control) were compared with 3D bioprinted ADSCs of controlled increasing printing shear. They found, with increasing shear stress, cell viability after printing was significantly decreased from 94% (4 kPa) to 86% (18 kPa). Viability of control group was slightly but significantly higher than 3D printed samples. They also showed high shear stress for short duration during printing does not affect cell viability immediately as much, but can induce long-term changes in the proliferation potential of cells that survived the printing process by comparing proliferation rates.

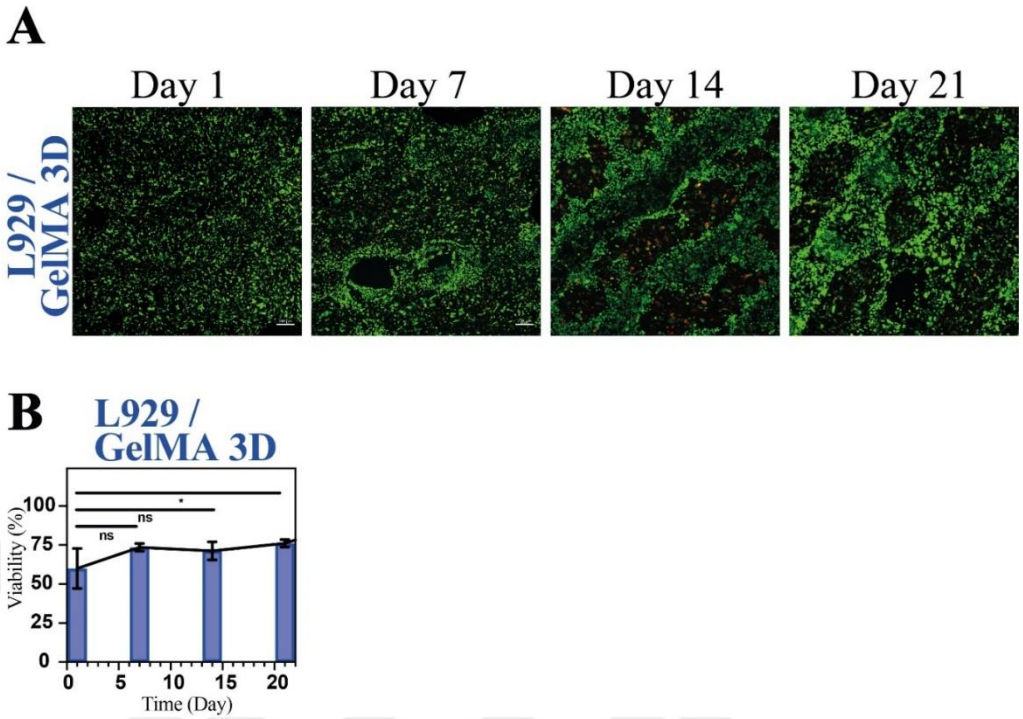

Figure 3.14. Viability of L929 cells in 3D printed GelMA (**A)** Cytotoxicity of PLC and GelMA was analyzed using live dead staining and CLSM microscopy analysis (Green: Live, Red: Dead, Scale bar: 400 µm. **B)** Viability of L929 cells obtained from live dead staining in 3D printed GelMA (n=3, One-Way ANOVA *p≤0.0332, ** p≤0.0021, *** p≤0.0002, ****p <0.0001).

3.4 Keratinocyte Isolation, Culture, and Maturation on Scaffolds

3.4.1.1 Isolation of KCs

To obtain primary KC cells, explanted human skin tissue was cut into pieces and cultured on TCPS. KC on the skin pieces was migrated onto TCPS. Primary keratinocytes in vitro were used in experiments after freshly obtaining. An inverted phase-contrast microscope was used to take the image of the keratinocyte migration **(Figure 3.15)**. KCs were cultured until confluency. Keratinocytes exhibited a heterogeneous morphology *in vitro,* as expected in the primary KC TCPS culture (Hunter-Featherstone et al., 2021). KCs in the epidermal tissue zone showed cobblestone morphology. Cells reached the outgrowth zone day at day 4 and

became confluent in 14 days. Outgrowth cells formed colonies and exhibited a heterogeneous morphology the characteristic cobblestone morphology as expected.

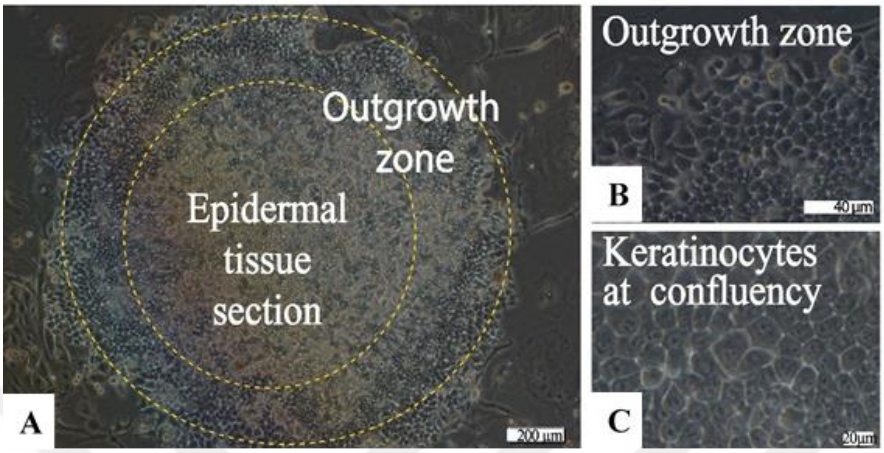

Figure 3.15. Keratinocyte isolation using the outgrowth method. Phase contrast images were taken. Explant epidermal tissue was cultured in TCPS (Epidermal tissue section). Cultured keratinocytes migrated and proliferated after day 4 (Outgrowth zone). Keratinocytes became confluent in 14 days

3.4.1.2 **KC Adhesion on PLC Scaffold**

Keratinocyte cells seeded directly onto PLC scaffold and cultured for 2 days. Low cell adhesion was achieved **(Figure 3.16A)**. Cell attachment needed to be improved.

3.4.1.2.1 Effect of Collagen Coating on Keratinocyte Adhesion to PLC

Synthetic polymer scaffold can be printed and recapitulate the native extracellular matrix, and a naturally occurring protein, collagen, can provide a physiologically relevant and recognizable platform to remodel the tissue. Collagen is present widely in the body and has good cell compatibility. (Sell et al., 2010). He et al. showed that blending collagen type I to PLC copolymer enhanced the viability, cell attachment, and spread. Keratinocytes adhered to the PLC scaffold after collagen coating and covered the surface of the PLC scaffold **(Figure 3.16B)**.

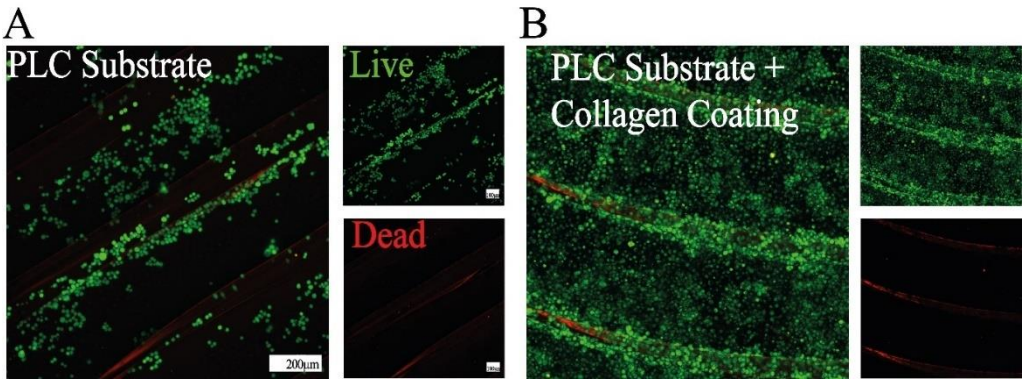

Figure 3.16. Effect of collagen coating on keratinocyte adhesion to PLC scaffolds. PLC scaffolds were 3D printed and live dead assay was performed. **A)** Keratinocytes seeded onto scaffold without collagen coating. Low cell adhesion was achieved. **B)** keratinocytes seeded on collagen coated PLC scaffolds using Coating Matrix Kit. Higher cell adhesion was achieved. (CLSM, Scale bar: 200 µm. Green: Live, Red: Dead).

3.4.1.2.2 Effect of Scaffold Geometry on Keratinocyte Adhesion to PLC

KCs were then used for finding the best pattern for the epidermis layer. KCs were seeded on different 3D printed patterns. PLC scaffolds were prepared as a smooth pattern, 3D printed as a 90° mesh or 3D printed wave-shift pattern. The smooth pattern was prepared as a control. As no cell leakage can occur into deeper layers, the adhesion of porous scaffolds was tested. The smooth pattern was not ideal because the non-porous PLC would block cell-to-cell communication between the epidermis and dermis.

Scaffolds were coated with collagen, as mentioned in Section 2.2.6.3. KCs were seeded onto collagen-coated patterns and cultured for 21 days, and a live dead assay was performed **(Figure 3.17)**. The PLC scaffolds absorbed the red dye and marked struts in the confocal images so that pores could be discriminated in the scaffold. Cells escaped from large macropores of 90° mesh design and migrated to the lower layer of the scaffolds or the cell culture plate. According to a study, cell viability and proliferation rate increased on smaller strand featured and high pore-sized scaffolds than larger feature-sized designed. The mean 2D pore cross-

sectional area of PCL scaffolds was 0.03709 and 0.001 mm^2 (Mehendale et al., 2017).

In this study, wave-patterned PLC design had strand shifts that decrease cell leakage to inner layers and tighten pore sizes. 90° mesh pattern and wave pattern scaffolds leaked cells before KC adhesion, as seen in Figure 24. More cells adhered to wave shifted design, and cells attached to each layer but mostly adhered to the top of the scaffold. Wave pattern provided additional stratification area and granted access to the more profound layers of skin model via overlapping shifted struts. So, KCs could interact with more deep skin layers and mimic epidermis-dermis interactions on our skin model. After choosing the printing pattern, large number of PLC were printed.

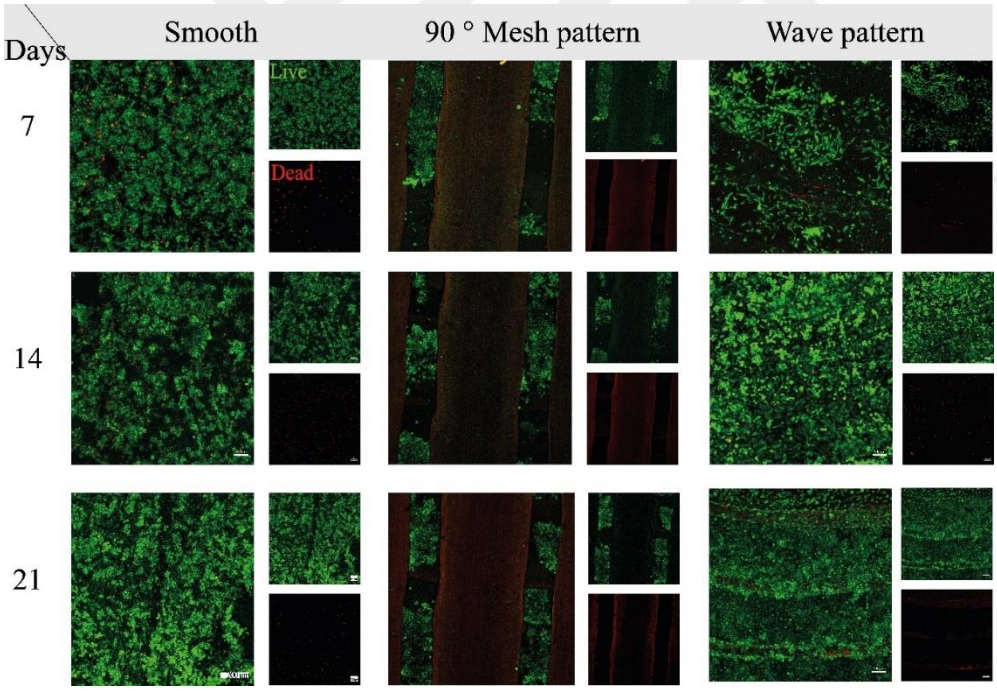

Figure 3.17. Effect of scaffold geometry on keratinocyte adhesion and surface coverage. PLC scaffold were 3D printed in different geometries and coated with collagen. Live dead assay was performed. Smooth, 90° mesh and wave pattern scaffolds were used (CLSM, Scale bar: 200 μm Green: Live, Red: Dead).

3.4.1.3 Air-liquid-interface (ALI) Culture of KCs on 3D printed PLC Scaffolds

KCs were seeded on the collagen-coated scaffold and cultured for 7 days to form a monolayer culture before starting air-liquid-interface (ALI). KCs were differentiated on the scaffold to mimic the stratified model of the skin by using the ALI method. ALI was initiated on 7th day of culture and named ALI Day 0 **(Figure 25A)**. During ALI, KCs became confluent, differentiated, and a stratified epithelium was formed **(Figure 3.18B)**. Stratification can be seen from the cross-section image of **Figure 3.18C**. A thicker epidermal region was formed on ALI Day 14 and can be seen from cross-sectional images (**Figure 3.18C**, Culture Day 21/ ALI Day 14 inlet). Significant increase in the cell number and layer thickening by ALI was measured in another study (Nossol et al., 2011). The stratified epidermis has multiple layers. Keratinocytes multiply in the basal layer and leave this layer toward the upper surface by maturation, differentiation, and migration to the surface. The outermost layer is made up of flattened dead cells (Navarro et al., 2017).

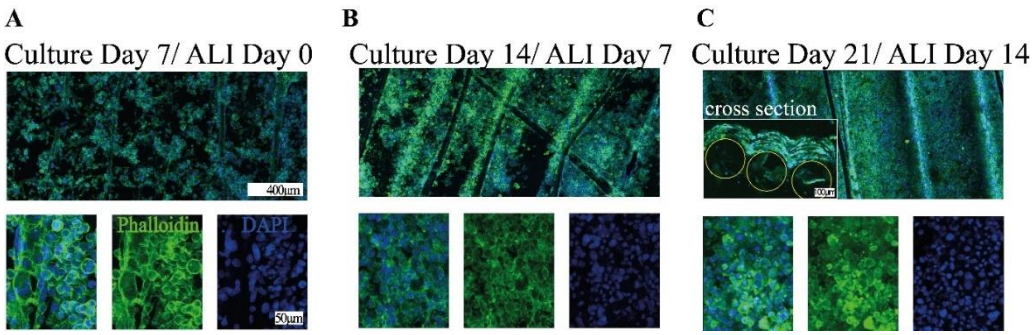

Figure 3.18. CLSM images of ALI culture for keratinocyte maturation. Live-dead (top) and Phalloidin-DAPI (bottom) Stainings. Superimposed images (left) of each phalloidin (middle) and DAPI (right) are given separately for each culture day. ALI duration **A)** Culture Day 7, ALI Day 0 **B)** Culture Day 14, ALI Day 7 **C)** Culture Day 21, ALI Day 14. (CLSM, Top; Live: Green, Dead: Red, Scale bar: 400 µm. Bottom; Green: Actin cytoskeleton, Blue: nucleus, Scale bar: 50 µm).

3.4.1.4 **SEM of 3D Printed KC Seeded PLC Scaffold After ALI Culture**

Cell-free SEM images of PLC scaffold had pore sizes between 136-160 μm, beneficial for nutrient transport and cell migration **(Figure 17)** (Xu et al., 2019). The surface of the differentiated KCs on the 3D printed wave shifted cell-seeded PLC scaffold was observed via SEM. SEM micrographs showed cell-loaded pore sizes were ranging between 6.2-26.26 μm **(Figure 3.19)**. This pore size range limited the number of cells infiltrating the scaffold, and cells may have migrated and proliferated towards the upper layers as in the human skin. Keratinocytes adhere to the scaffold, elongated to neighbouring strust, contact with each other and form a compact barrier **(Figure 3.19A and B).** SEM images illustrated that keratinocytes were inside of the PLC scaffold wall and grown along pores **(Figure 3.19C and D).**

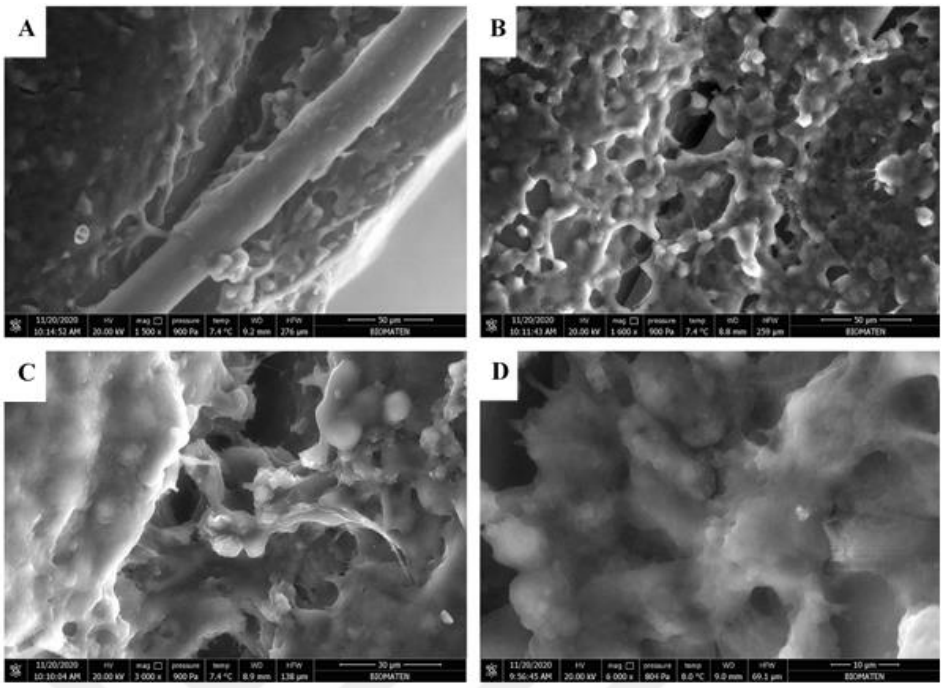

Figure 3.19. SEM images of keratinocyte seeded 3D printed PLC scaffold. Images were taken on 7th day of ALI differentiation. Pore sizes were measured from SEM images and found 6.2-26.26 μm (n=4). Cells adhere to the PLC scaffold and form cell-to-cell connections **A)** Keratinocyte ingrowth between scaffold struts **(**Scale bar: 50 μm), **B)** Cells invaded struts of scaffold and maturated, can be seen from cell stratification on the outermost fiber. **(**Scale bar: 50 μm), **C)** Cell growth in deeper layers of the scaffold (Scale bar: 30 μm), **D)** Keratinocytes largely spread and form dense cultures. **(**Scale bar 10 μm).

3.5 Dermis and Hypodermis Layers Co-Culture Studies

The dermis and hypodermis layers of the skin model were composed of different ratios of ADSCs, adipocytes, and DFs. Adipocytes were obtained from adipogenic differentiation of ADSCs. The dermis is a strong and flexible region of the skin. Dermis layer was composed of strong and flexible connective tissue and made up of fibroblasts, macrophages, and occasionally mast cells (Klenerman, 2015). The fibroblast-rich and stem cells act on the wound healing process (Tracy et al., 2016). A ratio of DF: ADSC (3:1) was selected for the dermis. Hypodermis and dermis borders are challenging to distinguished, but hypodermis is rich in adipocytes (Somuncu et al., 2018). Therefore, a ratio of DF: Differentiated ADSC (1:3) was

selected for the dermis. Culture conditions for adipogenic differentiation and co-culture media were investigated.

3.5.1 Adipogenic Differentiation of ADSCs

3.5.1.1 Defining Adipogenic Potential of ADSCs in Adipogenic Differentiation Media (MADM)

Adipogenic differentiation potential of ADSCs cultured with adipogenic differentiation media (MADM) was measured for 21 days **(Figure 3.20)**. Adipogenic characterization of ADSCs is characterized by changes in cell metabolism and accumulation of lipid droplets (Marcon et al., 2019). Arising number of lipid droplets shows ongoing adipogenic differentiation. Lipid positive cells were counted with Image J software. 21 days differentiation was not preferred due to the more extended culture period and similar differentiation ratio than the 14-Day differentiated group **(Figure 3.21)**.

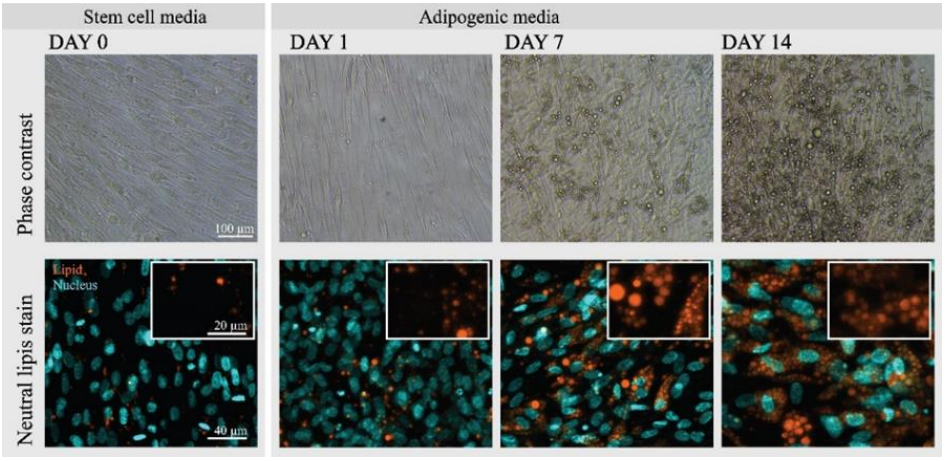

Figure 3.20. Adipogenic differentiation for 21 days. ADSCs were seeded and cultured with stem cell media until 80% confluency (Day 0). Then, medium was changed to adipogenic differentiation media (MADM) and counted as day 1. Adipogenic differentiation media were used for 14 days. Lipid droplets of adipogenic differentiated cells were captured. Top image is captured by phase contrast microscopy (Scale bar 100 µm. Bottom image is CLSM image of LipidTOX-DAPI staining. Lipid droplets were zoomed and showed in small rectangulars on top of the images. (Scale bar 40 µm, Lipid droplets: Orange, Nucleus: Cyan, Scale bar 40 µm, Scale bar of zoomed lipid droplets: 20 µm).

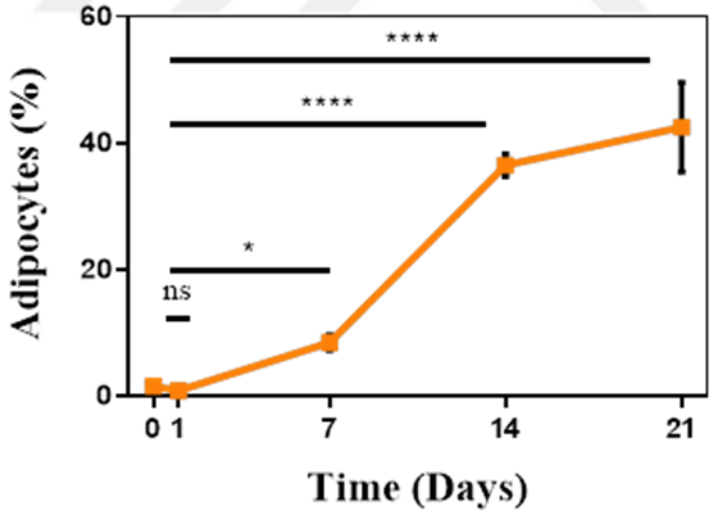

Figure 3.21. Adipocyte percantage after adipogenic differentiation of ADSC for 21 days. ADSCs were cultured in stem cell media until 80% confluency (Day 0). Then, medium was changed to adipogenic differentiation media (MADM) and counted as day 1. Adipogenic differentiation was maintained for 21 days. Nucleus of lipid accumulated cells were counted as differentiated cell (n=3).

3.5.1.2 **Defining Required MADM Ratio**

3.5.1.2.1 The Effect of Initial ADSC Differentiation Duration

ADSCs were cultured for 1 week to reach 80% confluency with MSCM medium in a 37 °C %5 CO_2 incubator. Then, adipogenic differentiation was initiated by changing the medium to MADM. The day differentiation started was named day 0. This experiment was performed to define the required initial adipogenic differentiation duration and MADM content for dermis and hypodermis layers. Therefore, lipid positivity and viability were tested for two adipogenic differentiation duration (7- and 14- days; (ID7, ID14)) and five different media compositions of MADM to DMEM High Glucose (100:0, 75:25, 50:50, 0:100) (Figure **3.22 and 3.23**). According to **Figure 3.23,** when MADM media was changed to MADM: DMEM media, differentiated adipocyte ratio of ID7 culture was 8.4± 1.22% and ID14 was 36.47±1.77%.

3.5.1.2.2 Lipid Droplet Formation and Maturation with Different Media Compositions

In all culture groups, lipid-positive cells increased with time (orange signal). ID7 cells showed a lower amount of lipid droplets compared to the ID14 group. Also, lipid droplets on ID14 (**Figure 3.22**) increased in size with time. It can be explained as lipid droplet maturation. According to previous studies, lipid droplets expand, the fuse on adipocyte differentiation and maturation (Olzmann & Carvalho, 2019).

The mechanism and development of the size and shape of lipid droplets remain primarily unknown. However, there is a balance between the size of droplets and the rate of lipid formation. In case excess of insufficient lipid droplets are formed, lipid toxicity may occur (Yi et al., 2020). Our observations on size and number increase were interpreted according to these studies. On 100% DMEM High

Glucose culture of ID14 group, vacuole-like structures were observed, which may be due to lipid bursting (Strålfors, 1990). Compared to the other medium cell cultures, during lipid droplet maturation, 50% of MADM cultures preserved their lipid integrity and reached. confluency without overpopulating the plate. Therefore, experiments proceeded with a 50% MADM ratio.

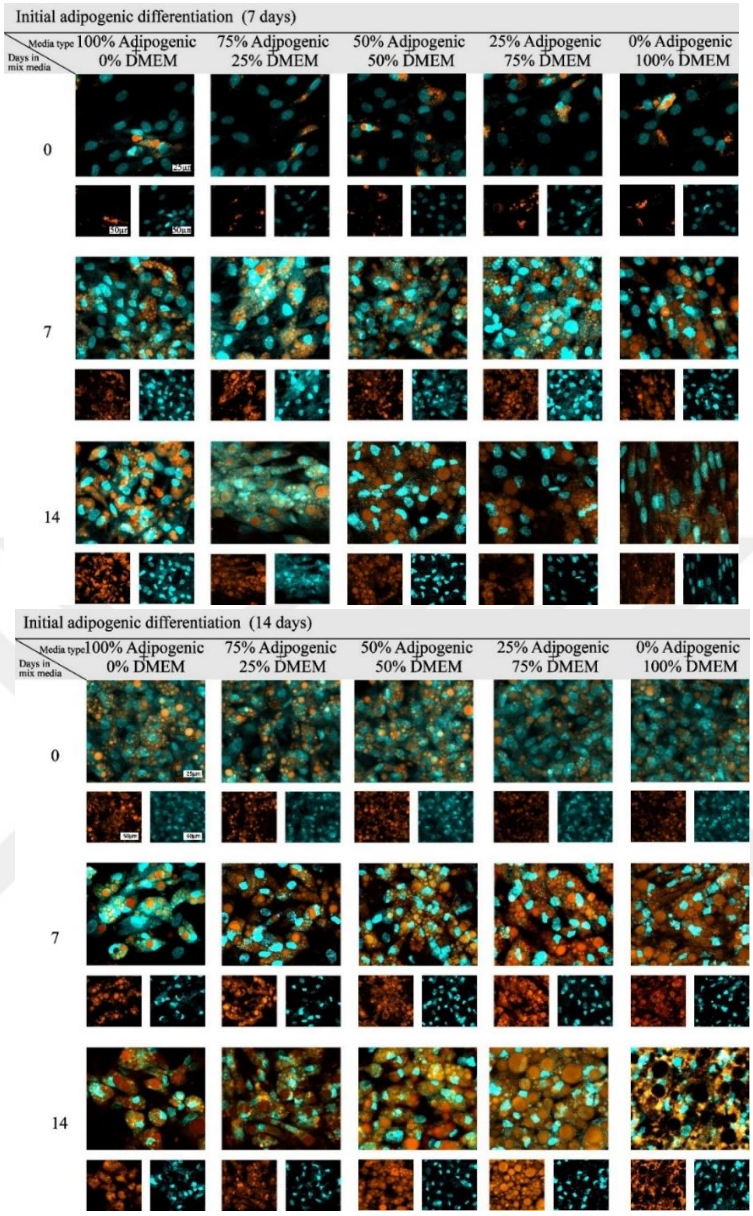

Figure 3.22. Adipogenic differentiation of ADSCs in 2D culture. CLSM images of LipidTOX-DAPI staining. Lipid droplets were stained and shown in orange as the indicator of adipogenic differentiation. ADSCs were cultured until 80% confluency and adipogenic differentiation media were introduced. Cultures were initially differentiated for **top segment-** 7 days (ID7) and **bottom segment-** 14 days (ID14) with MADM media. Then, media were changed to five different media compositions of MADM to DMEM High Glucose (100:0, 75:25, 50:50, 0:100). Top images: Superimposed images of DAPI and LipidTOX. Bottom left images: LipidTOX stain only. Bottom right images: DAPI stain only. (CLSM, Scale bar of Superimposed images: 25 μm, Scale bar of lipid only and DAPI only images: 50 μm. Orange: Lipid, Cyan: nucleus).

3.5.1.2.3 Viability and Adipogenic Differentiation of ADSCs Cultured with Different Media Compositions

In the group where cells were initially differentiated for 7 days (ID7), 25% of ADSCs were positive for lipids and showed 95% viability before changing to 4 different media **(Figure 30A)**. In this ID7 group, a minimum of 80% lipid-positive cell ratio was achieved in all media ratios on the 7^{th} day of the experiment. This might be explained as the initial 7 days in MADM induced adipogenic differentiation of cells to the adipogenic route. On the 14^{th} day, the differentiation ratio was above 90% **(Figure 30B)**. Adipogenic differentiation starts with mesenchymal stem cell lineage commitment (MSCs) into preadipocytes (de Paula et al., 2021). According to a study, upon reaching confluency, preadipocytes, differentiating adipose stem cells, experience contact inhibition, re-enter the cell cycle and finally undergo terminal adipocyte differentiation (Fajas, 2003). In our case, MADM was introduced when ADSCs reached 80% confluency. Cells continued to proliferate until they reached 100% confluency, then showed contact inhibition, and underwent adipogenic differentiation even without MADM medium as discussed in the literature (Fajas, 2003). In the group where cells were initially differentiated for 14 days (ID14), a similar trend was seen on days 7 of 14 of ID14. On the day medium was changed to 4 different media after 14 days of adipogenic differentiation, more than 90% of cells were already lipid positive. ID14 cell cultures maintained a high ratio throughout the experiment regardless of culture media. According to a study, adipogenic differentiation triggers ADSCs to a strong downregulation of proliferation genes, and cell cycle even though viability was not changed (Marcon et al., 2019). This is proven in this study at 100% and 75% DMEM High Glucose cultures. Less MADM in culture media led to over confluency of cultures than higher MADM ratio cultures.

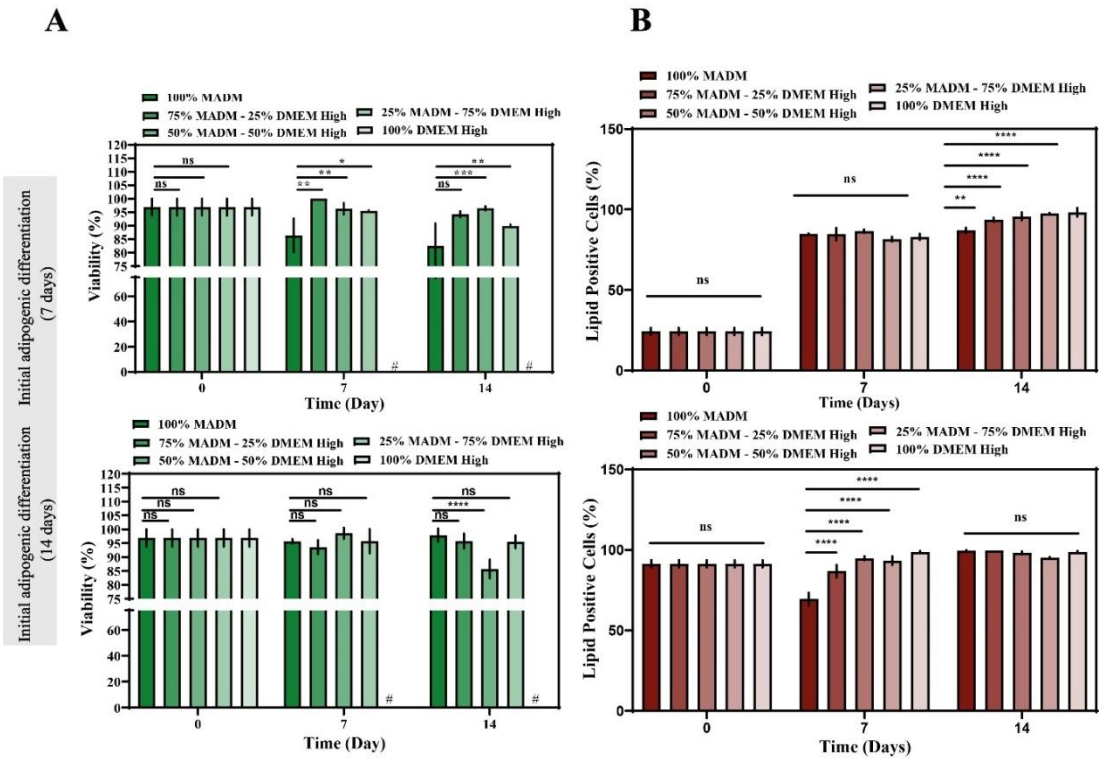

Figure 3.23. Viability and adipogenic differentiation of ADSCs in 2D culture. ADSCs were cultured with stem cell media until 80% confluency. Initially, 1st group was cultured in MADM for 7 days (ID7), and 2nd group for 14 days (ID14). **A)** Viability and **B)** adipogenic differentiation of ADSCs cultured in five different media compositions of MADM to DMEM High Glucose (100:0, 75:25, 50:50, 0:100. Viability and lipid positivity were counted from CLSM images (n=3).

The images of live dead analysis are presented in **(Figure 3.24)**. In the 100% and 75% DMEM High Glucose groups, cultures became over-confluent after 7 days.

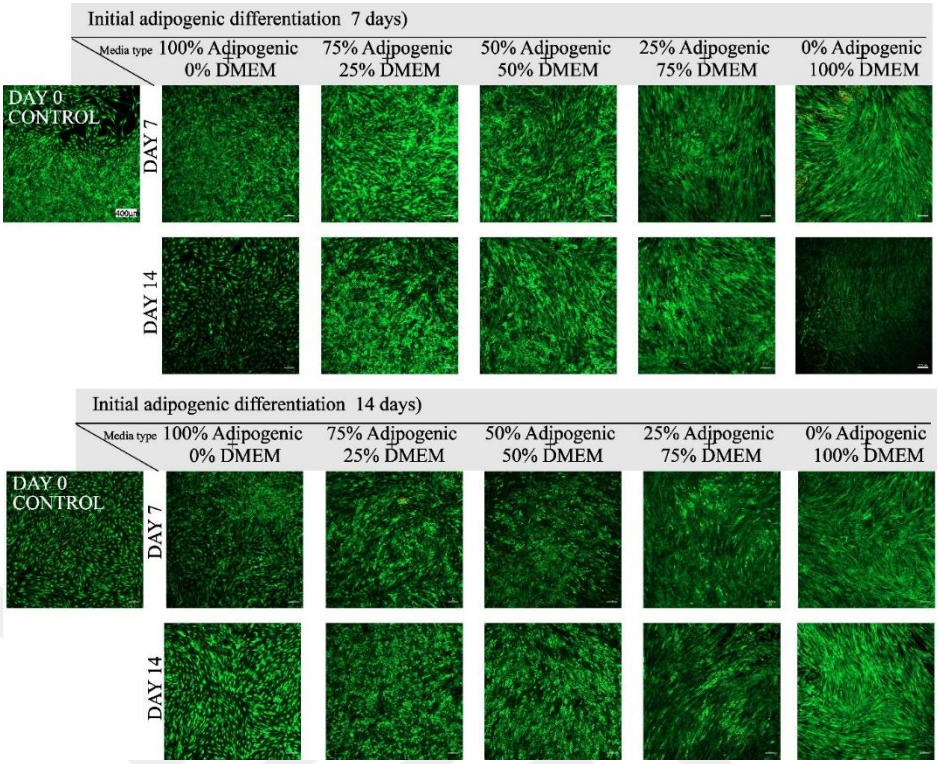

Figure 3.24. Viability of ADSCs cultured in five different media compositions of MADM to DMEM High Glucose (100:0, 75:25, 50:50, 0:100). ADSCs were cultured with stem cell media until 80% confluency. Initially, 1st group was cultured in MADM for 7 days (ID7) (top segment), and 2nd group for 14 days (ID14) (bottom segment). Viability and lipid positivity were counted from CLSM images (n=3) (CLSM, Scale bar: 400 μm, Green: Live, Red: Dead).

3.5.2 **Defining Co-culture Media**

Co-culture experiments were conducted with 2D, 3D printed cultures of DF, and ADSC. 4 different MSCM, MADM, and DMEM High Glucose media compositions were mixed in different concentrations **(Table 2.1)** and tested for ADSCs, DFs, dermis, and epidermis co-cultures. Proliferation and viability were studied and interpreted together with differentiation data from Section 3.5.2.2 for defining co-culture media. Optimized culture conditions were identified and used to generate a 3D skin model. A possible negative effect of different culture media on coculture needs to be checked beforehand. DMEM High media (DMEM+ 10% FBS + %1 P/S) is also referred as ADSC proliferation medium in the literature

(Yao et al., 2013) and also used for culturing explant human fibroblasts (Şeker et al., 2014). But the study of Yao et al. showed lower adipogenic differentiation when using proliferation medium (DMEM High) compared to adipogenic media and linked to dedifferentiation (Yao et al., 2013). Nevertheless, our experiments with DMEM and MADM showed no significant difference in terms of adipogenesis compared to MADM cultures **(Figure 3.23 and 3.24)**. In a study, 15 different media were tried to produce a vascularized tissue model coculture (Yang et al., 2020). ADSCs, human umbilical vein endothelial cells (HUVECs), and normal human lung fibroblasts (NHLFs) were cultured separately and together as cocultures to understand the effect of media compositions individually. Growth media (EGM-2 (Endothelial growth media): Adipogenesis media) were mixed as 0:100, 10:90, 30:70, 50:50, 70:30, 100:0). Then, angiogenic components were added to the media composition chosen one by one to understand their effect on coculture. Minimum 30% EGM was found sufficient for sustaining proliferation to all three cell types and 50-50 % was chosen for the final medium composition considering the lipid staining results. This technique was adapted in this study and different media contents were tested for different media compositions individually and together. The Adipocyte-rich hypodermis layer reflects adipose tissue. The hypodermis layer was composed of higher ADSCs (adipocyte differentiated) and less DF with the DF: ADSC ratio (1:3). DFs, ADSCs (and adipocytes), dermis, and epidermis co-culture were maintained on 48-well-plates 14 days with four different media compositions (**A**: 25% MSCM, 25%MADM, 50% DMEM High Glucose; **B**: 50% MSCM, 25%MADM, 25% DMEM High Glucose; **C**: 25% MSCM, 50%MADM, 25% DMEM High Glucose; **D**: 50% MSCM, 50% MADM) **(Table 3.1)**.

3.5.2.1 **2D Cell Co-culture**

Lipid positivity, stemness and proliferation percantage were controlled for DF: ADSC; (hypodermis, 1:3) and (dermis, 3:1) cocultures and DF, ADSC

monocultures with A, B, C and D medium compositions **(Figure 32)**. Single and co-cultures were stained with phalloidin, LipidTOX green **(Figure 32A)**, and CD105, LipidTOX green (**Figure 32B**) to identify cells in cultures.

3.5.2.1.1 Intracytoplasmic Neutral Lipids Comparison with LipidTOX-DAPI

MADM-rich Medium C and D cultures showed higher adipogenic differentiation than Medium A and B cultures. 50% MADM was sufficient to obtain desired adipogenic differentiation and adequate viability in the previous experiment **(see Figure 3.23 and 3.24)**. Yang et al presented similar results (Yang et al., 2020). Experiment setup was mentioned in Section 3.5.2. They found, adipogenesis media alone resulted significantly lowered ADSC proliferation ratio compared to all other media compositions with EGM-2. Higher ADSC proliferation rates were obtained using maximum 70% Adipogenesis media in coculture. They did not choose 100% adipogenesis media because HUVECs did not survive. But 100 % adipogenesis media didn't significantly altere the lipid amount compared to 50-50 % (Adipogenesis media: EGM-2 without supplements). After collective coculture experiments, they moved on with 50-50 % (EGM-2: Adipogenesis media) growth media. There was less adipogenic differentiation on hypodermis Medium C co-culture than the Medium D co-culture in **Figure 3.25A**. DMEM High media may have caused adipocyte dedifferentiation as previously mentioned in Section **3.5.2** (Yao et al., 2013). Therefore, Medium D was a good candidate for adipocyte-rich hypodermis culture of 2D culture experiments conducted on TCPS.

3.5.2.1.2 Immunohistochemistry of Stem Cell Marker

CD105+ is a type I membrane glycoprotein that serves as an accessory receptor for TGF-beta superfamily ligands, it is expressed in vascular endothelial cells, fibroblasts, monocytes, chondrocytes, and hematopoietic progenitor cells. ADSC obtained from adipose tissue expresses CD105+ increasingly upon cultures (C. S.

Lin et al., 2013; Nassiri et al., 2011; Yoshimura et al., 2006). Here, CD105+ expression was followed to identify ADSCs **(Figure 3.25B)**. CD105+ was also expressed in DFs but less abundantly (Alt et al., 2011; C. S. Lin et al., 2013). For this reason, DF single-cell culture was used as a control. Adipocytes were discriminated by the lipid signals. Cell nucleus were stained with DAPI. Alexa Fluor 647-Phalloidin was used for imaging actin cytoskeleton. Therefore, DF cells could be discriminated with nucleus and actin without LipidTOX and CD105+ or fewer CD105+signal. In Medium B and D, cultures showed higher stem cell markers in hypodermis and dermis co-cultures.

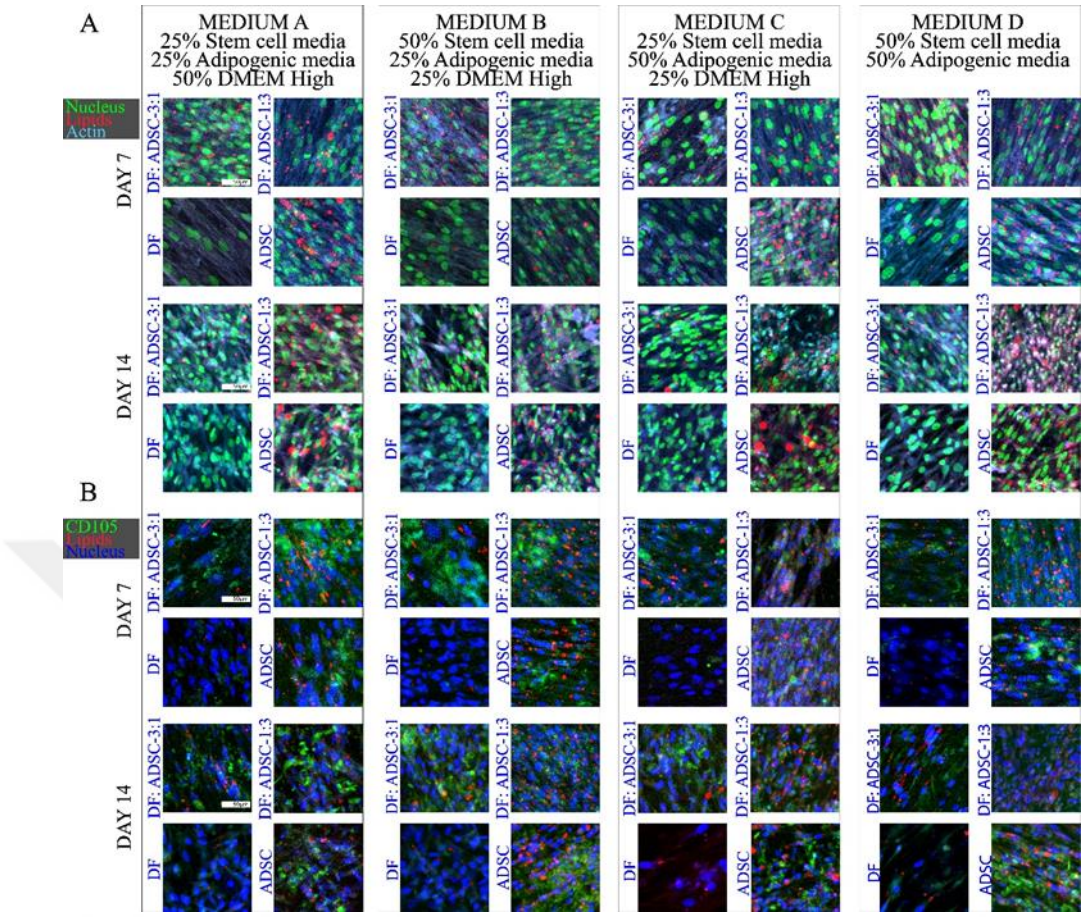

Figure 3.25. Confocal images taken for co-culture experiments with DF, ADSC, and adipocytes. A- DF, ADSC, DF-MSCM 3:1, and 1:3 ratios were cultured with four different growth media compositions. Cells were stained with LipidTOX (red signal) for intracytoplasmic neutral lipids, cytoskeleton (blue), and nucleus (green) (scale bar=50 μm). B- ASSC, DF-ADCM 3:1, and 1:3 ratios were cultured in four different growth media compositions. Cells were stained with LipidTOX (red signal) for intracytoplasmic neutral lipids, cytoskeleton (blue), and CD105 stem cell marker (green) (scale bar=50 μm).

3.5.2.1.3 Defining Proliferation Rate via Alamar Blue Assay

Co-cultures and single-cell cultures were further investigated for proliferation rate via Alamar Blue Assay (**Figure 3.26**). Regardless of media compositions, ADSCs and DFs co-cultures showed higher cell proliferation than ADSCs or DF single-cell cultures **(Figure 3.26 A-C).** It validates the previous researches on the stimulatory effect of ADSCs on DF's proliferation rate (Kim et al., 2007). The synergetic effect

of including different cell types when creating a tissue model emphasizes the increased cell proliferation of co-cultures by approximately two times. The effect of medium compositions was more noticeable after the first day, but the difference faded in the following days. DF cells proliferate more in Medium B single-cell culture, but not much on co-cultures. Medium D showed better performance on co-culture groups, especially on day 4. Hypodermis coculture showed more lipid signal with medium D compared to medium C. ADSCs of dermis coculture showed higher CD105+ signal, and denser actin signal compared to medium C. On day 7, although ADSC culture with medium C resulted in high lipid content, in the hypodermis layer (DF:ADSC 1:3) lipid content was not as high as observed for ADSC culture. This trend continued until day 14. Due to lack of adipogenic differentiation, medium C was not suitable for hypodermis. On the other hand, when ADSC and hypodermis cultures with medium D were compared, hypodermis layer showed higher adipogenesis. Therefore, medium D was chosen for hypodermis. When medium C was used for culturing the dermis (DF:ADSC 3:1) layer, DF showed very few lipids and for dermis layer the lipid was also low on both days 7 and 14. CD 105+ expression was low on day 7, but it was high on day 14. Medium C may not be the best fit for dermis. dermis layer showed higher lipid content when Medium D was used compared to DF and low CD105+ signal. It was decided that medium C or D could be used for dermis coculture. Medium D was used to simplify the chip model by using the same media with hypodermis layer. The dermis and hypodermis experiments were proceeded with Medium D.

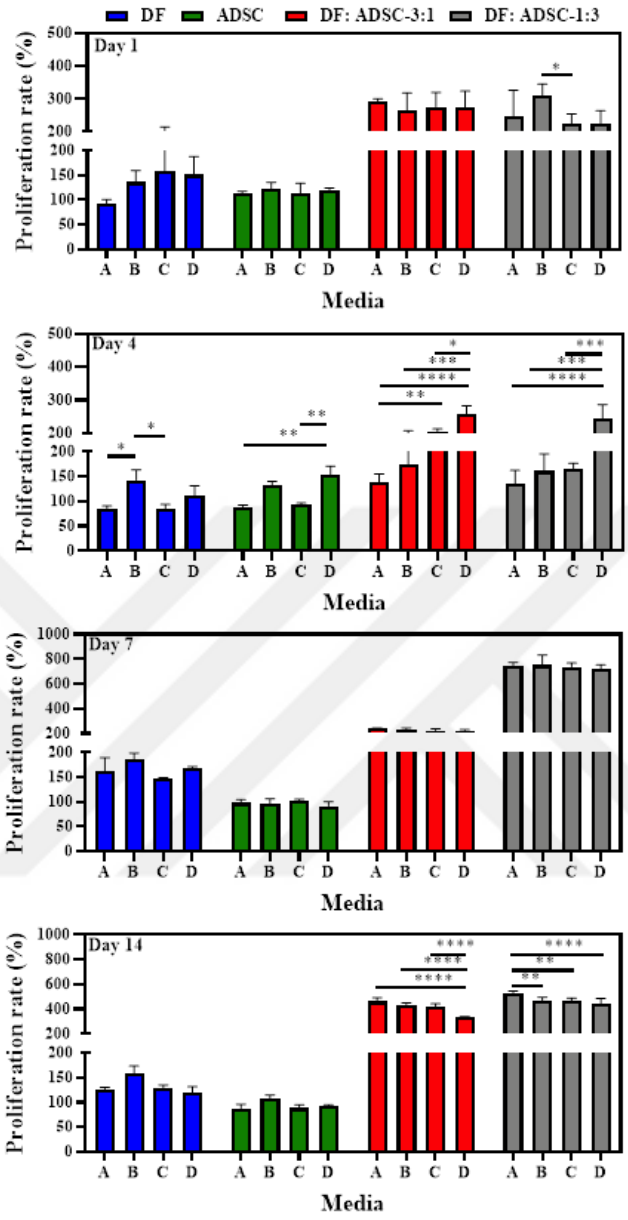

Figure 3.26. Co-culture culture proliferation percentage of DF, ADSC, and adipocytes. Viability of DF, ADSC, and co-cultures under selected four growth media compositions, measured using Alamar Blue assay (**A**: 25% MSCM, 25%MADM, 50% DMEM High Glucose; **B**: 50% MSCM, 25%MADM, 25% DMEM High Glucose; **C**: 25% MSCM, 50%MADM, 25% DMEM High Glucose; **D**: 50% MSCM, 50% MADM) (One-way ANOVA, *p≤0.0332, ** p≤0.0021, *** p≤0.0002, ****p <0.0001).

3.5.2.2 **Viability of 3D Cell Co-cultures**

The dermis (DF-ADSC 3:1) and hypodermis (DF-ADSC 1:3) cocultures were mixed with GelMA prepolymer solutions and bioinks were formed. Bioinks were 3D printed separately and cultured for 21 days with medium D **(Figure 3.27)**. Fibroblast-rich dermis culture was spindle shaped. Adipocyte-rich hypodermis scaffold contained more spherical cells. Cells became spread within the gel and proliferated. Cells migrated and accumulated near pores in both dermis and hypodermis scaffolds. On printing day, viability of dermis was near to 80% and hypodermis was nearly 70 %. This may be the lower because of the cell bursting due to shear stress. L929 GelMA 3D printing results also showed viability near 65 per cent. Or comparing dermis and hypodermis layers, ADSC might have lowered the viability of cocultures during printing and therefore viability was lowered in hypodermis culture more. In both scaffolds, cell viability reached above 90% at day 21.

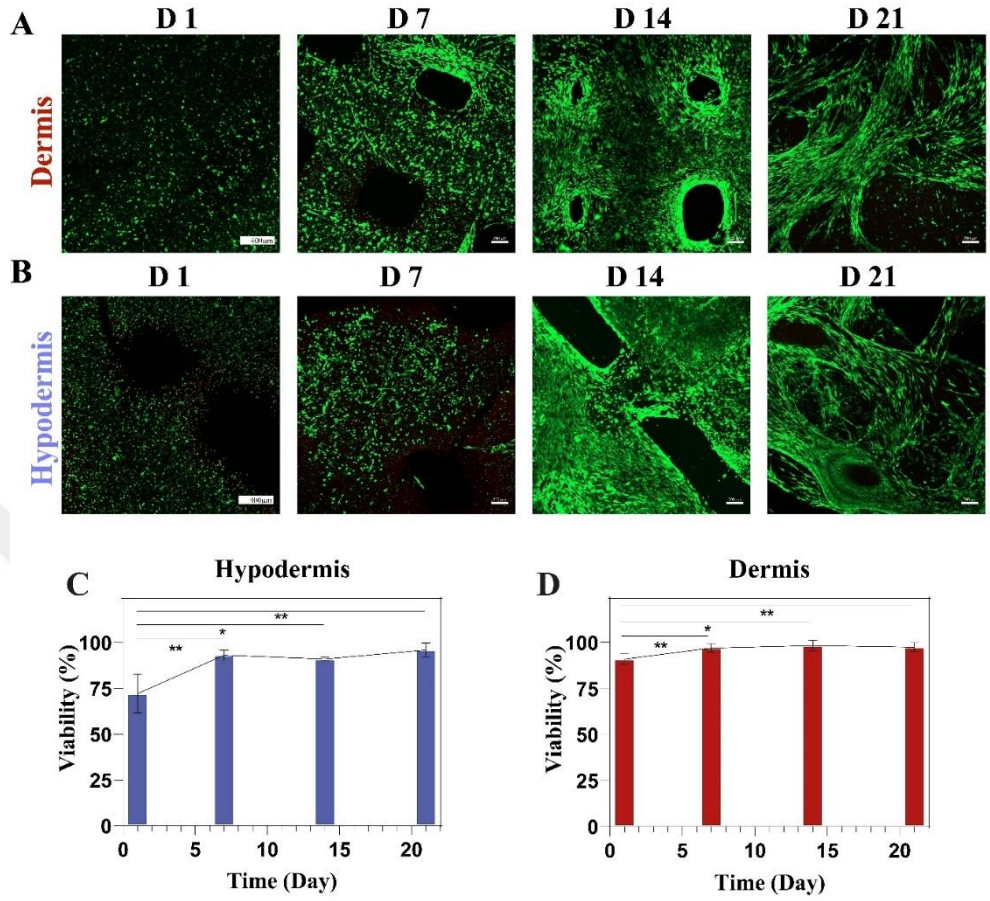

Figure 3.27. Co-culture viability observed in the dermis and hypodermis layers. Growth medium composition D was used (50% MADM- 50% MSCM). Live-dead staining of 3D printed dermal layer (DF-ADSC 3:1) co-culture (green: live, red: dead, scale bar=400 μm). Live-dead staining and viability of 3D printed **A, C)** Hypodermal layer (DF-ADSC 1:3) co-culture (green: live, red: dead, scale bar=400 μm). **B, D)** Dermal layer (DF-ADSC 3:1) co-culture (green: live, red: dead, scale bar=400 μm Viability of cocultured cells was analyzed from live-dead staining CLSM images (n=3) (One-way ANOVA, *p≤0.0332, ** p≤0.0021, *** p≤0.0002, ****p <0.0001).

3.6 Epidermis, Dermis, Hypodermis Layer Production and Maturation

3.6.1 3D Bioprinting of GelMA Scaffolds

Dermis bioink was prepared as follows. Cartridge of 3D printer was washed with EtOH in tissue culture hood and sterilized under UV for 20 minutes in laminar flow hood. GelMA prepolymer solution (15% (w/v) and 0.6 % (w/v) in DMEM High) were cooled down to 37 °C before mixing with the cell suspension. DF: ADSC (3:1) cell suspension was prepared and mixed with GelMA prepolymer solution and loaded into the cartridge in the laminar flow hood to avoid contamination risk. 3-layered dermis was bioprinted via a 3D printer (3D-Bioplotter, Envisiontec). Conical plastic nozzle with an inner diameter of 0.33 was used. Thus, thickness of the dermis was 0.69±0.07 mm.

Same printing conditions were applied to the production of hypodermis layer. Cell suspension was DF: ADSC (1:3) for the hypodermis layer. Hypodermis layer was made up of 5 layers and the thickness was 1.16± 0.28 mm.

The epidermis, dermis, and hypodermis layers were 3D printed, cultured separately, and brought together like building blocks. Each layer was cultured for 21 days before inserting into the chip. Chips were built precisely for scaffold insertation. PLC and GelMA layers were printed with precise 1 mm radius and inserted into 1.1 mm laser-cut holes one by one and sticked together without any help **(Figure 3.28)**.

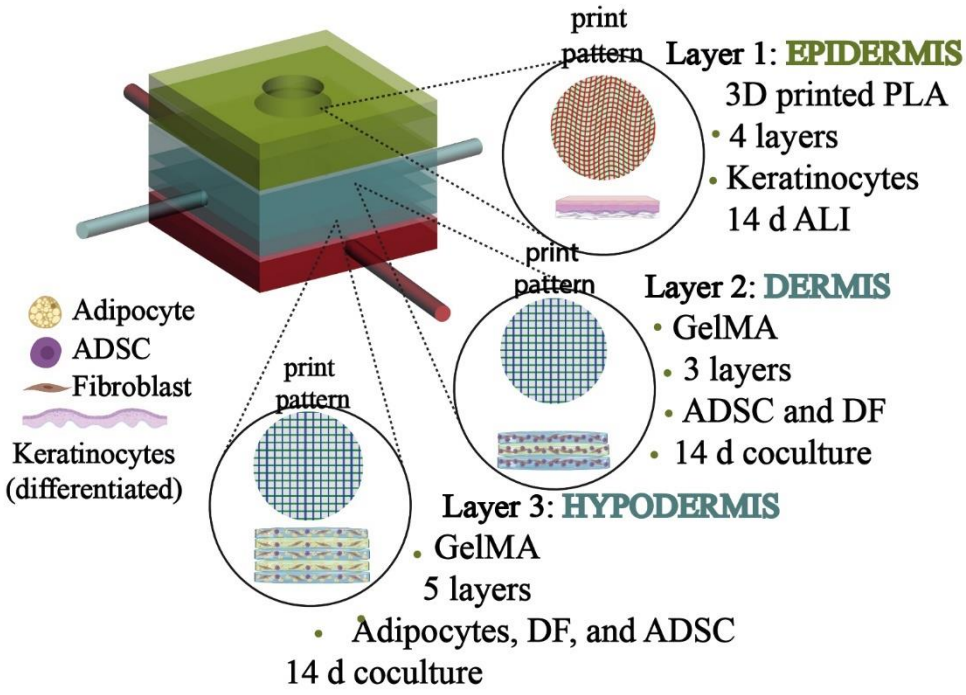

Figure 3.28. Build-up of skin-on-a-chip model. The skin model was composed of PLC epidermis, and GelMA dermis, and hypodermis layers. 3 layers were cultured separately and inserted into the chip.

3.6.2 **Maturation of Epidermis Layer**

Epidermis provides barrier function to water loss and protect body against environmental hazards. It is comprised of many layers that form a stratified squamosus ephitelium. Epidermis is separated from dermis by the basal membrane. Keratinocytes on basal membrane continiously proliferate and periodically leave the basement membrane and migrate upwards. This process is called keratinocyte differentiation. Keratinocyte differentiation terminates when cells slowly lose nucleus and sloughed off. Cells move upwards and outermost anucleated cells are replaced with fresh cells coming from the basal layer. This renewal takes around 30 days and called terminal differentiation of keratinocytes (Koria & Andreadis, 2006; McKay & Leigh, 1995). *In vitro* modelling of this differentiation process was done by seeding keratinocytes on a scaffold and mimic the natural anatomy of the skin.

After monolayer of keratinocytes is formed, outermost part of the scaffold is raised to the air. Blood supply (cell culture media) comes from downwards and cells outermost cells face air. This process is called air-liquid interface. The reason behind keratinocyte leaving basement membrane is mostly unknown, but previous studies mention asymmetric perpendicular division orientation of basal keratinocyte progenitors (Lechler & Fuchs, 2005). A more recent study revealed local cell-to-cell interactions and tension differentials might dictate cell fate choices of the basal layer of epidermis. High proliferation rate of basal lamia cells and cellular delamination initiate stratification (Damen et al., 2021). Cadherin is one of the main component of the adhesive structure that enable dynamic cell-extracellular matrix and cell-cell interactions during differentiation and migration. E-cadherin is a transmembrane molecule and links neighboring cells through homophilic interactions. E-cadherin interactions mediate actin cytoskeleton of neighbouring cells (Hodivala & Watt, 1994; Tinkle et al., 2004; Young et al., 2003). Monolayer keratinocytes do no exhibit adherent junctions. Adherent junctions of dermis are majorly formed by E-cadherin. Formation of intercellular junctions initiates stratification (Lewis et al., 1994). Recent works showed that localized E-cadherin coordinaes tissue polarization of tension beating adherens junctions. E-cadherin junctions integrates adhesion, biochemical signaling, biochemical signaling and contractile forces. For mimicking epithelial barrier, E-cadherin barrier must be mimicked *in vitro* (Rübsam et al., 2017). Epidermis layer was produced and investigated as follows: Strand shifted wave-patterned PLC scaffold was printed. The scaffold was coated with collagen, and KCs were seeded and cultured for 7 days. Subsequently, the 3D epidermis model was transferred into inserts, an air-liquid interface (ALI) was initiated for keratinocyte stratification. ALI culture proceeded for 14 days. As a control, a smooth PLC membrane was used. The seeding procedure was repeated **(Figure 3.29A, *left panel*).** Cultures were stained with pan-cytokeratin and E-cadherin antibodies to distinguish the differentiation and maturation of KCs on strand-shifted patterns. Morphologically similar structures to stratified epidermis layers were identified from KCs populated

in the deeper layers. Keratinocyte differentiation due to ALI was observed as E-cadherin translocated from the cytosol to cell-cell adhesions and cobble-stone-like appearance on ALI Day 14 **(Figure 3.29A, *right panel*)**.

Human skin's anisotropic shape was considered in the epidermis scaffold design. Layer shifts provide a firm structure and mimic the epidermis layer's basal lamina **(Figure 2.2)**. Layer shifts form tiny pores until layers below, and the deepest layer pores are theoretically closed in the scaffold design. So, KCs could settle to the deepest layers without leaking and differentiate through outer layers as innate stratified epidermis layers. In literature, strand shifting between layers were studied and changes in hydraulic permeability was seen. Medium exchance was hindered and degradation products were builded up. Weight loss of PLC scaffolds were nearly 0.5 % in 12 weeks (Walejewska et al., 2020).

3.6.3 Maturation of Dermis and Hypodermis Layers

The dermis and hypodermis layers were 3D bioprinted separately and incubated in 50%-50% MADM: MSCM medium for 21 days. Confirmation of ADSCs adipogenic differentiation and becoming adipocytes was done by staining lipid droplets of the adipocytes. Cells in all scaffolds were imaged using the Z-section images taken by confocal microscopy **(Figure 3.29B-C)**. The porous design of the dermis and hypodermis allowed oxygen and mass transport to the cells which can bee seen from migrated and densed cell groups near pores in the 3D bioprinted GelMA and cell-seeded PLC layers. Therefore, cells were able to mature without apparent cell death. To benefit more from media, cells densely adhered to the pore edges. So, a 3D network in which cells reached the scaffold's inner and outer parts were formed. GelMA scaffolds maintained their structural integrity and were kept their original design above 80 days (data not shown). The ease of GelMA scaffold fabrication allowed producing 40 scaffolds with/ without cells at once in a reproducible manner. Increasing density of E-cadherin shows good stratification formation within this model (**Figure 3.29A).** Keratinocytes were spread and

formed connections between cells. E-cadherin formation was low in the 2D and 3D culture without ALI. After day7, E-cadherin signal increased and spread to the deeper layer, which means terminally differentiation. The pan-cytokeratin antibody is a cocktail of antibodies that identifies a broad range of cytokines. It is useful for detecting the degree of different at. The cytokeratins express thoughout the basal layer (Fuertes et al., 2013).

The difference in cell content between dermis and hypodermis was clear on confocal images. A fewer number of ADSCs were loaded into dermis bioink compared to the hypodermis. Using 50% MADM medium during culture resulted in fewer lipid droplet formation in the dermis, which can be seen from LipidTOX staining **(Figure 3.29B)**. On the other hand, hypodermis bioink included one week of differentiated adipocytes, which lead lipid droplets became visible from the first day of hypodermis culture **(Figure 3.29C)**. DF-rich dermis layer exhibited cell migration within dermis scaffold and had a more prominent cytoskeleton **(Figure 3.29B,** cyan) compared to the hypodermis, which had fewer number of DFs (cross-sectional images, **(Figure 3.29C**). Before integrating into the chip dermis, and hypodermis scaffolds were cultured for 14 days. The epidermis was cultured for 14 days in ALI (total days of cultivation 21). Then, layers were assembled into the chip to build a skin model.

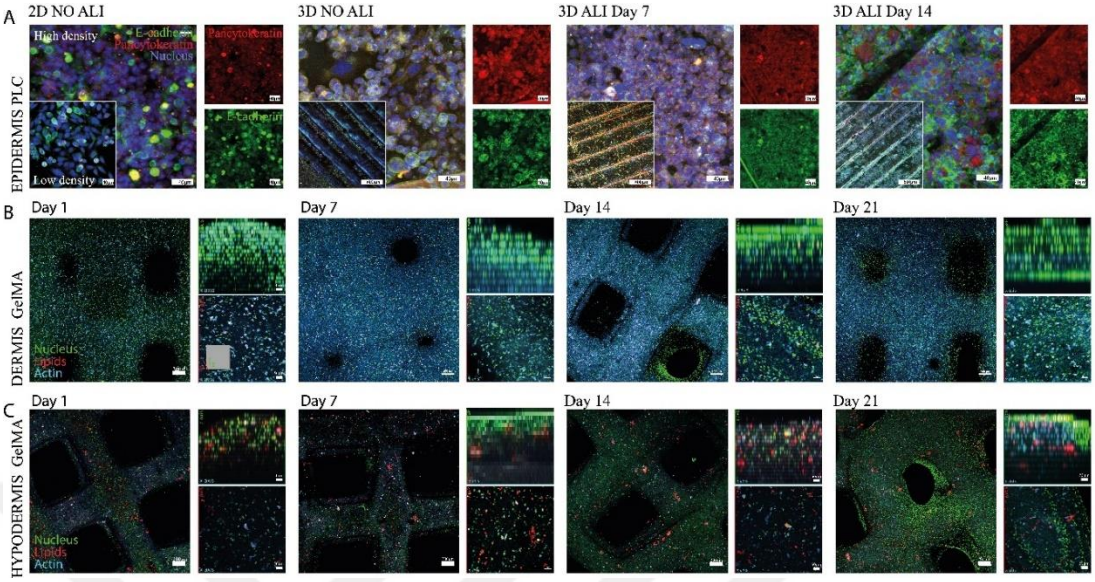

Figure 3.29. Differentiation and maturation in the epidermal, dermal, and hypodermal layers for 21 days. Inset image shows side sections of the skin model. **A)** Keratinocytes were seeded on 3D printed wave-shift pattern. Cells were cultured for 7 days in growth media, then ALI was established after 14 days and can be seen from E-cadherin in all layers (E-cadherin: green, Pancytokeratin: red, Nucleus: Blue). **B)** Dermis layer was produced with DF: ADSC 3:1 ratio encapsulated in GelMA (Nucleus: green, Lipids: red, cytoskeleton: cyan) (*Left panel*: X5, *Right top*: Z stack, *Right bottom*: X20). Bottom- Hypodermis layer was produced with DF: ADSC 1:3 ratio encapsulated in GelMA (Nucleus: green, Lipids: red, cytoskeleton: cyan) (*Left panel*: X5, *Right top*: Z stack, *Right bottom*: X20)

3.7 Microbioreactor Experiments

3.7.1 Structure of the Microbioreactor Chip

The final skin microbioreactor construct comprises 3 chambers for the epidermis, soft tissue, and bottom reservoir. 3 chambers were produced with 5 layers of laser cut PMMA layers stuck together with double-sided **adhesive (Figure 3.28, 3.30)**. Final layered scaffolds were placed into the chip during the assembly. In which the epidermis was placed, the top chamber had an open space so ALI could continue, and KCs could continue differentiating like human skin. A membrane filter with

1.2 µm pore size was placed between epidermis and dermis scaffolds. Epidermis scaffold was placed on this membrane. This membrane prevented KC migration into deeper layers but allowed cell-to-cell communication within the epidermis and dermis layers.

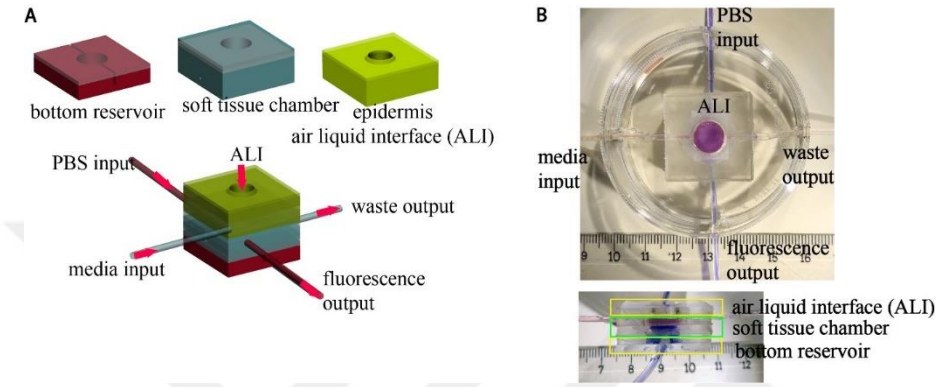

Figure 3.30. Microfluidic chip design. **A)** Three reservoir chip designs with epidermis air-liquid interface (ALI) chamber, soft tissue chamber, and bottom reservoir (*top to bottom*). **B)** Picture of full chip construct without epidermis layer. Dermis layer was stained pink, and dermis was stained blue for discriminating the layers for the imaging.

The bottom reservoir was designed to provide flow to measure penetrated drug concentration through the multi-layered skin construct. The bottom reservoir was engraved via laser cutter during chip production to make an area for scaffolds could sit, and restrain fluid flow, and prevent moving. Middle and the bottom reservoirs were covered with a membrane filter (**Figure 3.28**) as mentioned above to hold GelMA layers up and prevent the bottom reservoir and channels from closing. The final dermis and hypodermis scaffolds were placed in the middle reservoir and media were given at a flow rate of 3.33 µL/min. Previously reported skin-on-a chip studies used flow rates between 3.28 µL/min and 20 µL/min (Lee et al., 2017).

3.7.2 **ESEM images of Epidermis and Dermis Layers**

The skin-on-a chip model was incubated in a microbioreactor for 4 days, and Environmental scanning electron microscope (ESEM) images of the epidermis and dermis layers were captured (**Figure 3.31)**. ESEM images were collected using live-cell imaging, and no fixation was applied. ESEM images showed cell infiltration and migration into the deeper layers of scaffolds. Preservation of the 3D topography can also be seen in ESEM images. KCs showed confluency between the pores of the PLC scaffold **(Figure 3.31A)**. Also, stratification was seen between strand shifts of the epidermis PLC scaffold. ESEM images proved the spread of DFs and ADSCs along the scaffold. Narrowing of GelMA scaffold's pores (**Figure 3.31B)** was attributed to the cell growth, and this is proved by the ESEM images of GelMA scaffold of the dermis.

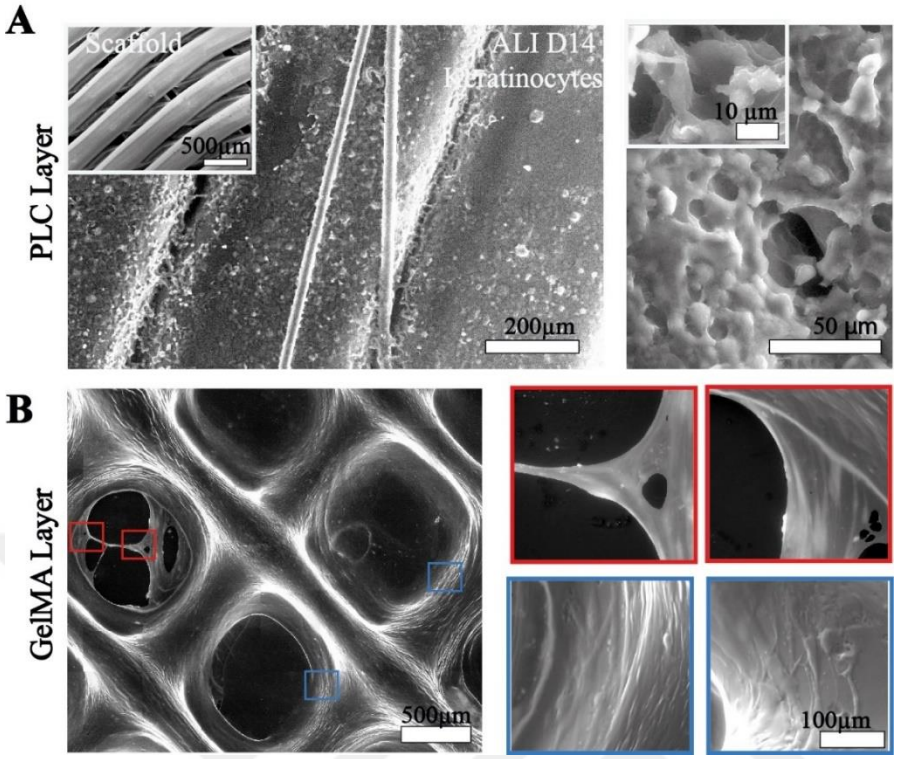

Figure 3.31. ESEM images of the PLC and GelMA after 4 d of a dynamic culture. **A)** ESEM image of 14 days ALI differentiated epidermis layer (Scale bar: 200 µm, left image X4) Inset image showed 3D printed cell-free PLC scalffod (Scale bar: 500 µm). Keratinocytes were spread and stratify in PLC scaffold. **B)** ESEM image of dermis layer on day 4 (Scale bar: 500 µm). Red inset image shows cell growth within pores. Blue inset image shows cell growth in pore surface (Scale bar: 100 µm).

3.7.3 **Computational Fluid Dynamics Analysis**

The computational fluid dynamics (CFD) analysis of the chip design was calculated to simulate the flow behavior in the microfluidic channels during the media and PBS inlet to the polymer skin layers. Flow rate and shear stress distribution were intvestigated **(Figure 3.32)**. Shear stress affects the arrangement, alignment and growth of the of the cells in the microfluidics chip. This technique could be useful for prediction of the permeability, porosity, concentration field and scalara transportation. The mathematical approach of CFD provides quantitative data regarding fluid percolation, mass and heat tansfe across the skin layers and

applied in transdermal drug delivery studies involving ski-on-a chip platforms which is usually not possible in *in vivo* or *ex vivo* experimental studies (García et al., 2019; Ponmozhi et al., 2021). The number of studies is still limited as the topic is relatively new. In a study, different fluid shear stress was applied to investigate the drug toxicity on cells in the presence of shear stress stimuli. They showed the reactive oxygen species levels significantly changed in differen fluid stress levels and compared to static flow culture. They distinguished the effect by the cell apopotosis rate. They claimed fluid shear stress accelerates the interaction between the cells and the drugs and provides more acting sites for drug interaction (Feng et al., 2019).

Upper and middle reservoirs (ALI and soft tissue) were modeled together, and the bottom reservoir was calculated separately. The opening of the bottom reservoir affects the flow profile in the middle chamber, acts as a pressure sink, and atmospheric pressure was involved in the calculation (**Figure 3.30**).

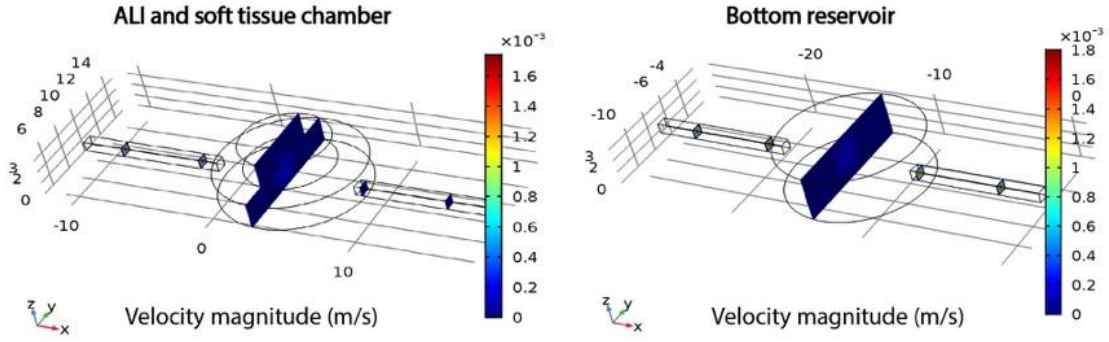

Figure 3.32. CFD models of the soft tissue chamber, and ALI, and bottom reservoir. Media flow velocity is depicted. Color scale shows the velocity magnitude in the middle cross-section of the chip (m/s).

The bottom reservoir and channels were designed for measuring penetration of the drug in the alyers. Shear stress on the bottom channels was investigated to find the shear affecting scaffolds inside the chip at the bottom reservoir. Shear stress profile drops nearly zero inside the middle of the chamber **(Figure 3.33)**. Velocities at channels are also very low (lowest at outlet channel <3.5 10^{-6}, highest at inlet channel 1.8 10^{-3}) **(Figure 3.34)** Flow rate was the highest in the level of the tubing center and decreased as it is farther from the middle. PBS did not only go through center, but also from the outside of the hydrogels. Flow is seen from the black space of the chip where scaffold was put into its reservoir and it is shown with blue color at two sides **(Figure 3.34)**.

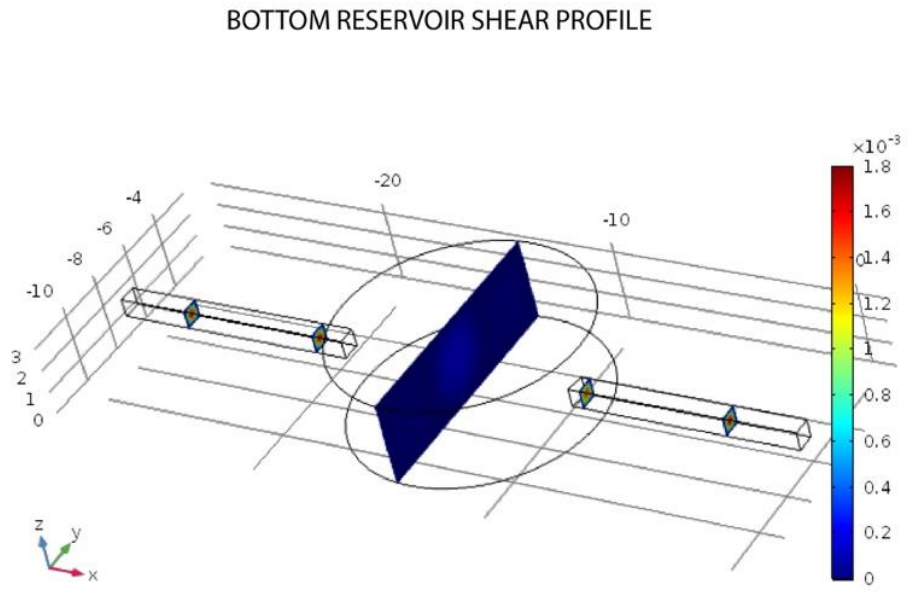

Figure 3.33. Shear profile of PBS of the bottom reservoir of the chip. Color scale shows the shear magnitude in the middle cross-section of the chip (m/s).

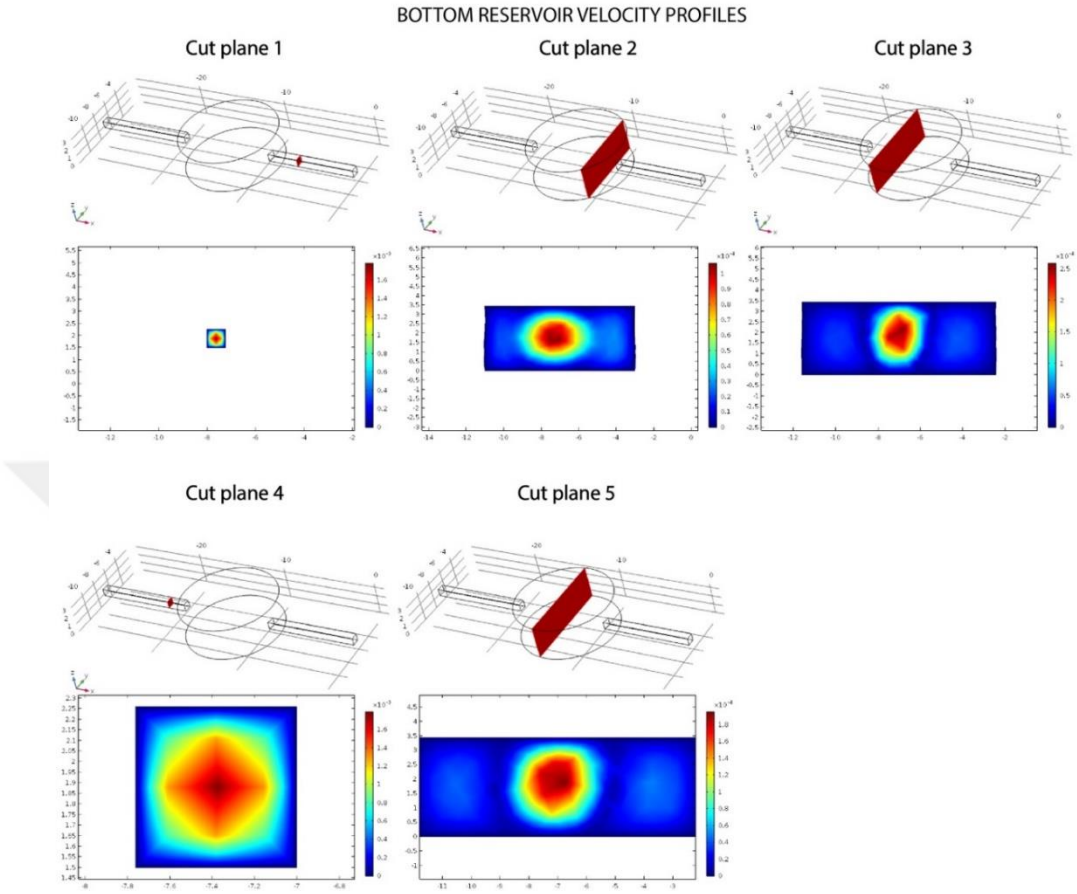

Figure 3.34. Velocity profiles of PBS bottom resorvoir of the chip. Cut plane 1: velocity profile of middle of the PBS outlet tubing. Cut plane 2: Velocity profile of the the PBS inlet tubing where PBS enter into outlet tubing. Cut plane 3: Velocity profile of the PBS where PBS exit from the inlet tubing and meet with scaffold. Cut plane 4: Velocity profile of the middle of the PBS inlet tubing. Cut plane 5: Velocity profile of the the middle of the chip. Color scales show the velocity magnitude in the middle cross-section of the chip (m/s).

Upper channel was used for injecting cell culture media. The flow rate of growth media running from the top channel was kept slow so that the cells in the middle reservoir were exposed to a nearly harmless shear stress. The calculated shear was little to zero **(Figure 3.35 and 3.36)**. Velocity was high in the middle of channels

and chip. As seen from cut plane 5, flow was scattered before entering the outlet tubing **(Figure 3.35)**.

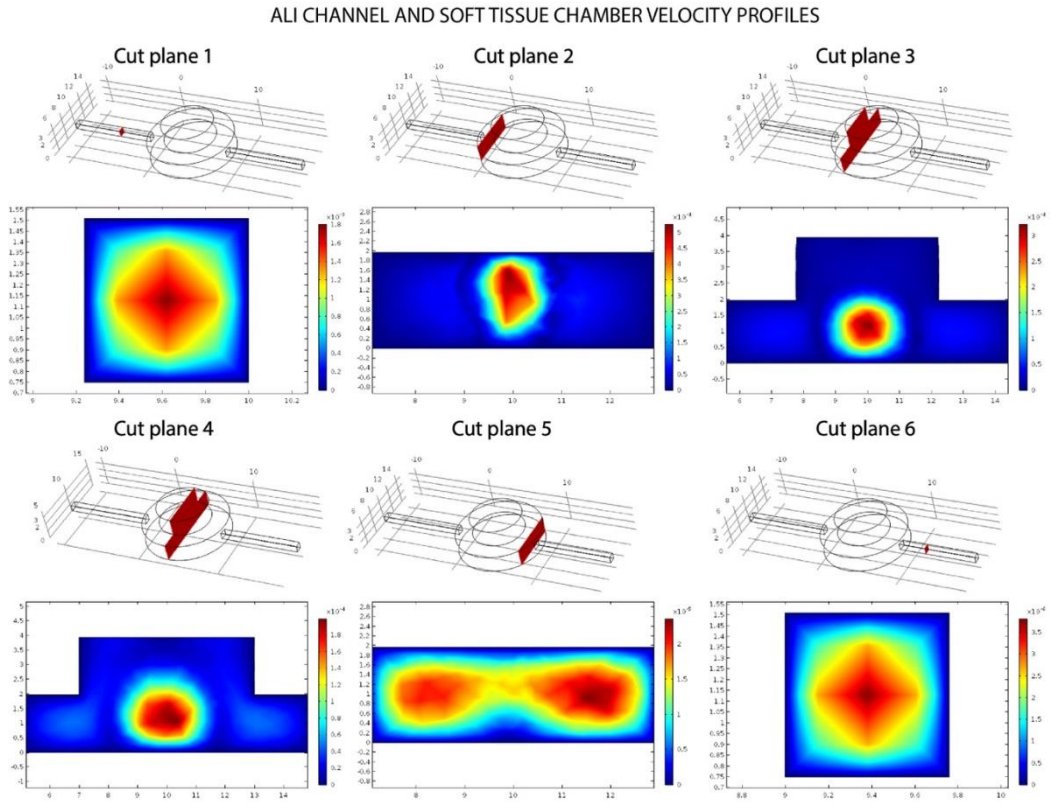

Figure 3.35. Velocity profiles of ALI channel, and soft tissue chamber. Cut plane 1: velocity profile of middle of the medium inlet tubing. Cut plane 2: Velocity profile of the medium inlet tubing where medium exits from the inlet tubing. Cut plane 3: Velocity profile of the medium inlet tubing where medium meets with the scaffold. Cut plane 4: : Velocity profile of the middle of the chip. Cut plane 5: Velocity profile of the medium where medium enters into the outlet tubing. Cut plane 6: Velocity profile of the middle of the medium outlet tubing. Color scale shows the velocity magnitude in the middle cross-section of the chip (m/s).

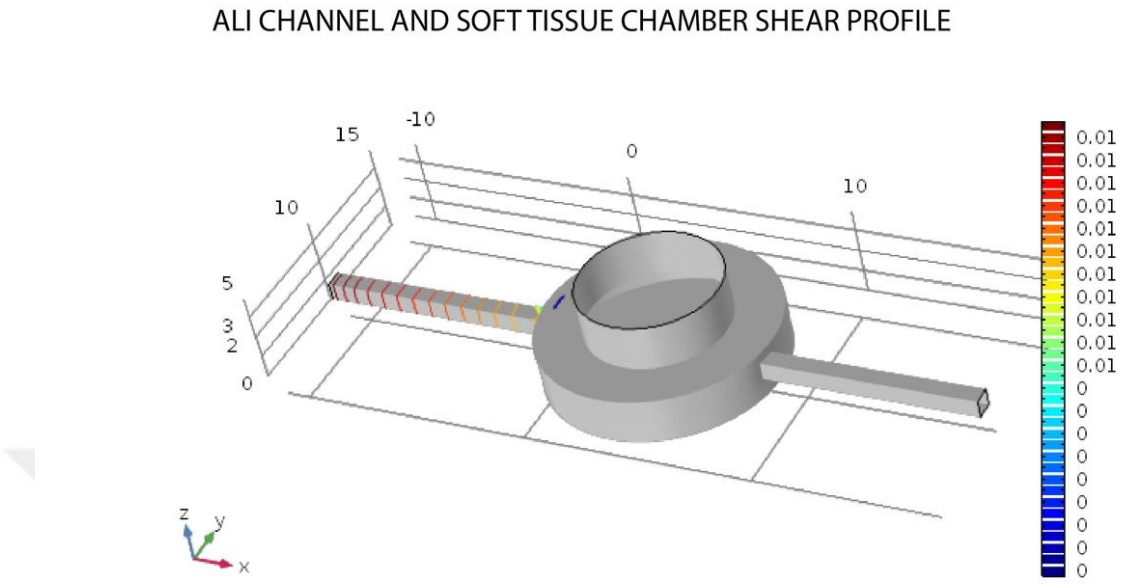

Figure 3.36. Shear profile of medium in the ALI channel and soft tissue chamber of the chip. Color scale shows the shear magnitude in the middle cross-section of the chip (m/s).

3.7.4 **Dynamic Culture vs. Static Culture of The Skin Model**

3.7.4.1 **Static Culture Design**

In parallel with the dynamic flow experiment on the microbioreactor, a steady static culture was also conducted to gain insight on the effect of shear on cell viability. The medium of static culture changed twice a day to keep the amount of fresh medium received the same as the dynamic culture.

3.7.4.2 **Viability Comparison of Static and Dynamic Cultures**

Static and dynamic cultures were compared on days 1 and 4 **(Figure 3.37 and 3.38)**. The live-dead assay was performed on static, dynamic GelMA layers and

membrane between dermis and epidermis (**Figure 3.37**). The effect of shear on cells was expected to be seen near the inlet and outlet. Live dead images were collected from the whole construct (*left panels*), the scaffold center, and locations corresponding to the inlet channels (*right panels*). Cell death caused by shear stress was very low near inlet parts of the dynamic culture. Some of the DFs and ADSCs migrated to the membrane which separates epidermis and dermis scaffolds on day 4 of dynamic culture **(*left panel, inset, membrane*)**.

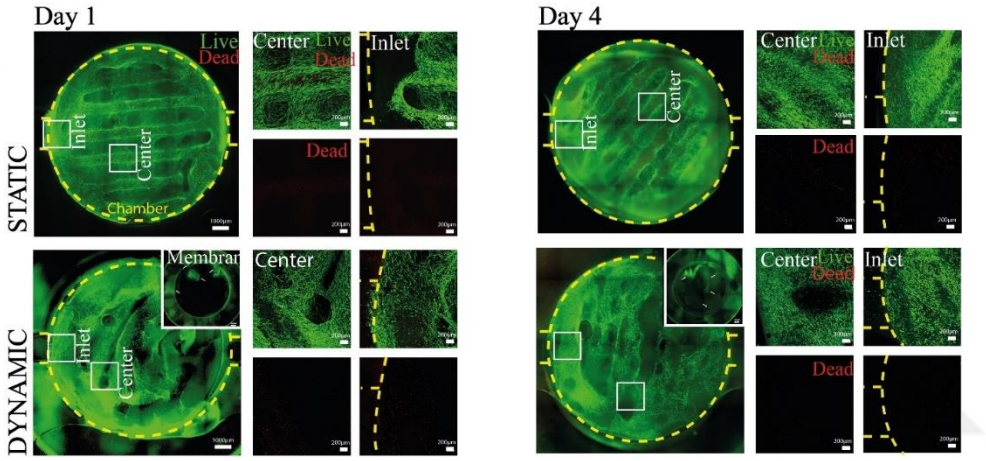

Figure 3.37 Live Dead analysis of the cells inside the scaffolds cultured under static and dynamic conditions on days 1 and 4. *Right panels:* close-up images from the center and the growth media inlets (green: live, red: dead).

In the literature, there are many studies on how skin homeostasis is maintained by the interplay between KCs, and DFs (Russo et al., 2020). The membrane blocked the cell migration from the dermis layer to the epidermis layer. However, soluble mediators of fibroblasts and keratinocytes can be assumed to cross the membrane pores. Porous design of epidermis layer allows interaction between cell seeded keratinocyte layer and cell loaded dermis layer. Keratinocyte growth factor, produced by DF, inducing keratinocyte proliferation (D.-P. Sun et al., 2013), might have passed the membrane and reached KCs in the epidermis layer.

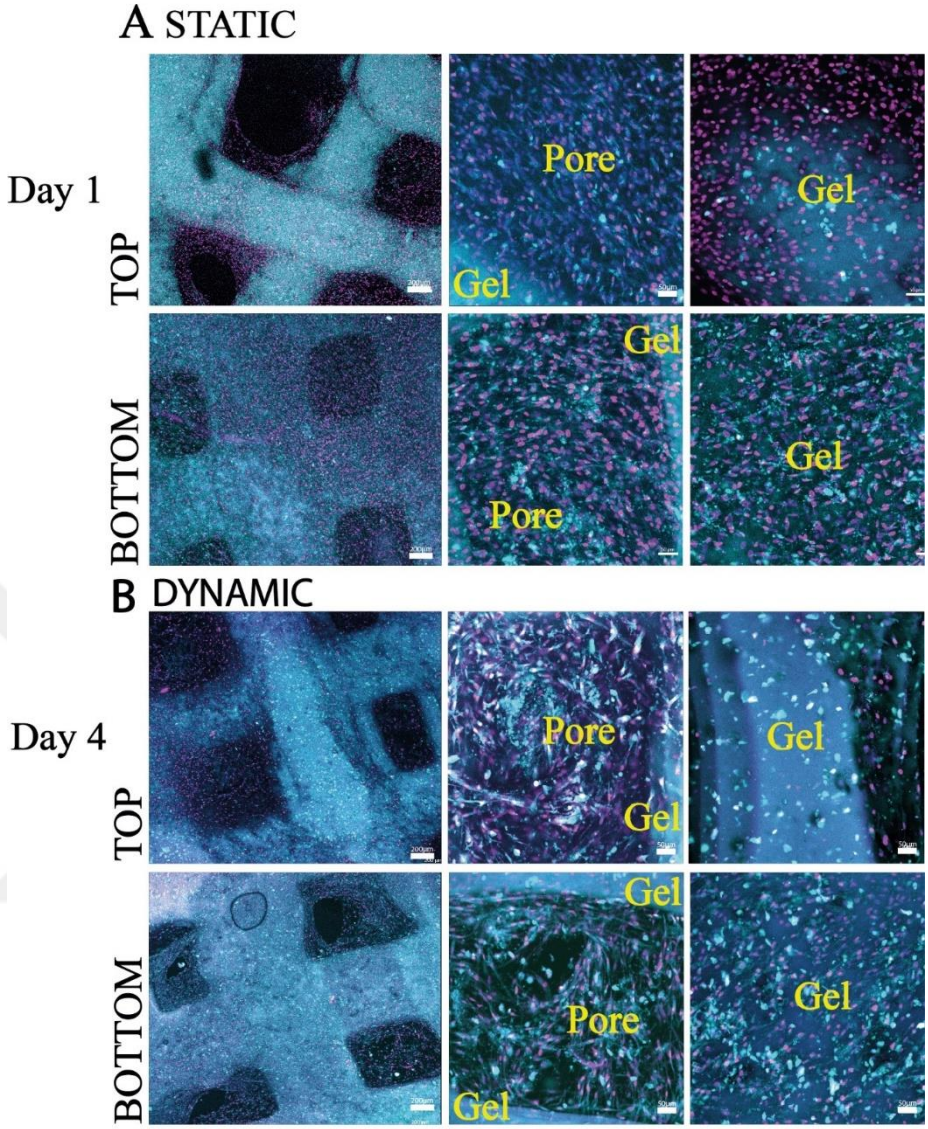

Figure 3.38. Phalloidin and DAPI staining of the **A)** static and **B)** dynamic cultures of scaffolds at day 4. *Right panels:* Close up micrographs of the pore and gel locations (Cyan: phalloidin, magenta: nucleus).

3.8 Drug Penetration in Microbioreactor

3.8.1 Dexamethasone Dose Response

Preliminary experiments for drug penetration assay were performed on KCs seeded on TCPS. Optimum Dexamethasone (Dex) dose was determined using dose dependent test **(Figure 3.39 and 3.41)**. FITC tagged Dex (FITC-Dex) was used in the experiments for fluorometric analysis and imaging. The relative cell viability observed for different drug doses during a culture period of 12 hours was calculated by normalizing Alamar results to no drug results (see Section 2.2.6.4.2.1). Compared to lower concentrations, higher Dex concentration led to higher viability. 100 μM and 10 μM groups showed higher viability compared to the no-drug group. The viability ratio was above 100% percent at some 8 h time point in both groups **(Figure 3.39)**. The proliferative effect of Dex on KCs has been reported in a study (Cho et al., 2019). Also, Dex's anti-apoptotic effect on human KCs was reported in the literature (Stojadinovic et al., 2007). These may be the explanations for the higher viability in higher dose groups.

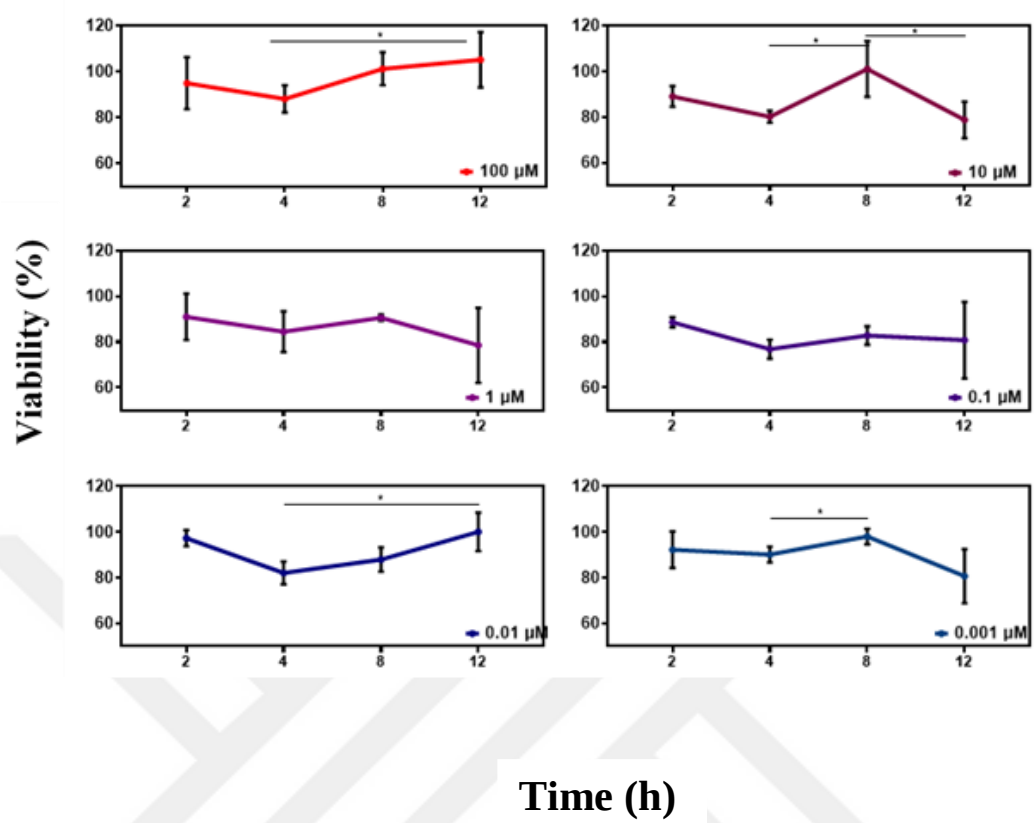

Figure 3.39. Alamar Blue viability results of keratinocytes treated with different concentrations of Dex (One-way ANOVA, *p≤0.0332, ** p≤0.0021, *** p≤0.0002, ****p <0.0001).

The effects of different FITC-Dex (0-100 µM) concentrations on KC morphology were examined with confocal microscopy analysis **(Figure 3.40)**. FITC-Dex treated KCs were imaged with the same signal intensity on Confocal microscopy to compare the signal intensities of different concentration groups. The highest concentration group (100 µM) had the most prominent green FITC signal as expected. Unfortunately, 100 µM Dex-FITC treated cells were distorted after 4 h.

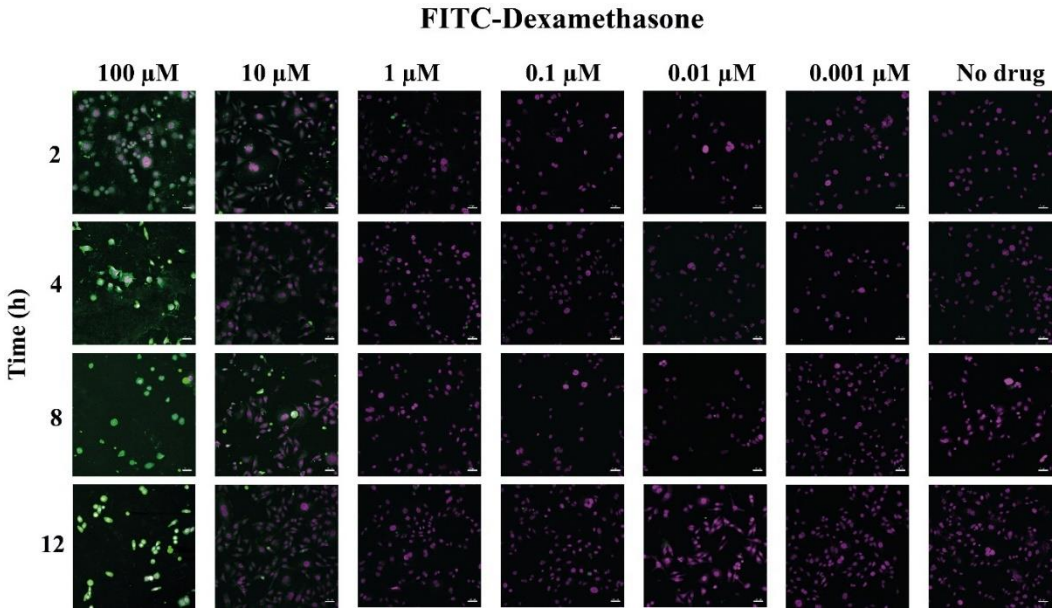

Figure 3.40. CLSM images of FITC-Dex treated keratinocytes at 2-12 h (Green: FITC-Dex, Pink: Nucleus). From left to the right, 100 µM, 10 µM, 1 µM, 0.1 µM, 0.01 µM, 0.001 µM and No-drug samples were imaged at the same fluorescence intensity.

Spectrofluorometric readings were done to FITC-Dex treated KCs (**Figure 3.41**). Fluorescence intensity was highest 100 µM FITC-Dex concentration sample as expected. Dex fluorescence signal accumulated in the first 8 h. 10 µM Dex dose was chosen on its excellent viability, high fluorescence intensity, and keeping cell morphology together throughout the experiment.

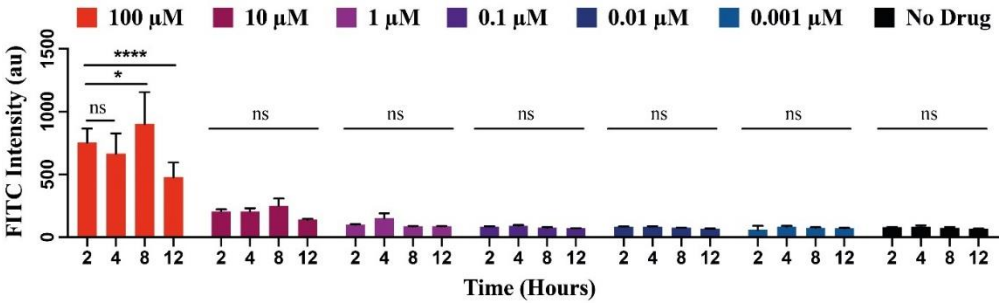

Figure 3.41. Fluorescence intensity of FITC-Dex treated keratinocytes. (One-way ANOVA, *p≤0.0332, ** p≤0.0021, *** p≤0.0002, ****p <0.0001). 100 µM, 10 µM, 1 µM, 0.1 µM, 0.1 µM, 0.001 µM FITC-Dex was used. No drug was used as control.

3.8.2 **Dynamic Penetration Assay**

Chip experiments were started after selecting the Dex dosage. 3-layered chips (epidermis, dermis, hypodermis) and 2-layered (dermis and hypodermis) chips were assembled and connected to a syringe pump to build the micro-bioreactor platform.

In order to obtain precise spectrofluorometric results, middle (soft tissue chamber inlet and outlet) and PBS channels (bottom reservoir inlet and outlet/ readout channel) were not running simultaneously. During dynamic cell culture, medium channels were active, and the readout channel was clamped. Controversy, when drug penetration experiments started, medium channels were clamped, and PBS channels were activated. After fixing clamps for the penetration experiment, the readout channel was run blank for 1 h before applying Dex to remove medium residue from the chip. An Eppendorf was placed at the end of the PBS outlet channel. 10 μM (100 μl) Dex was dropped from the ALI opening at the outermost layer of the chip. PBS flow was initiated from the syringe pump. Samples were collected from the readout channel regularly for spectral analysis **(Figure 3.42**). 2- and 3-layered skin models were prepared with and without cells (as control) to see the effect of drug uptake of cells in the skin model. The presence of cells delayed the drug penetration in both 2 and 3 layered skin-on-chip models. In 2 layered models, an additional delay on Dex penetration was observed due to the buffering effect keratinocyte-seeded epidermis layer. Decreased penetration rate caused Dex distribution to be more extended and evenly than the 2-layered model, which implies the importance of including all 3 layers to the skin mode for accurate penetration results. According to literature, fibroblasts and keratinocytes uptake Dex within an hour and requires another hour to release (Ponec, 1984). This also supports the evidence of delayed concentration increase at the first hour of Dex application in cell-loaded models for both 2-and 3-layered skin-on-chip models compared to cell-free models of both. Cell-loaded skin-on-a-chip models follow a steadier trend compared to no-cell groups in all samples.

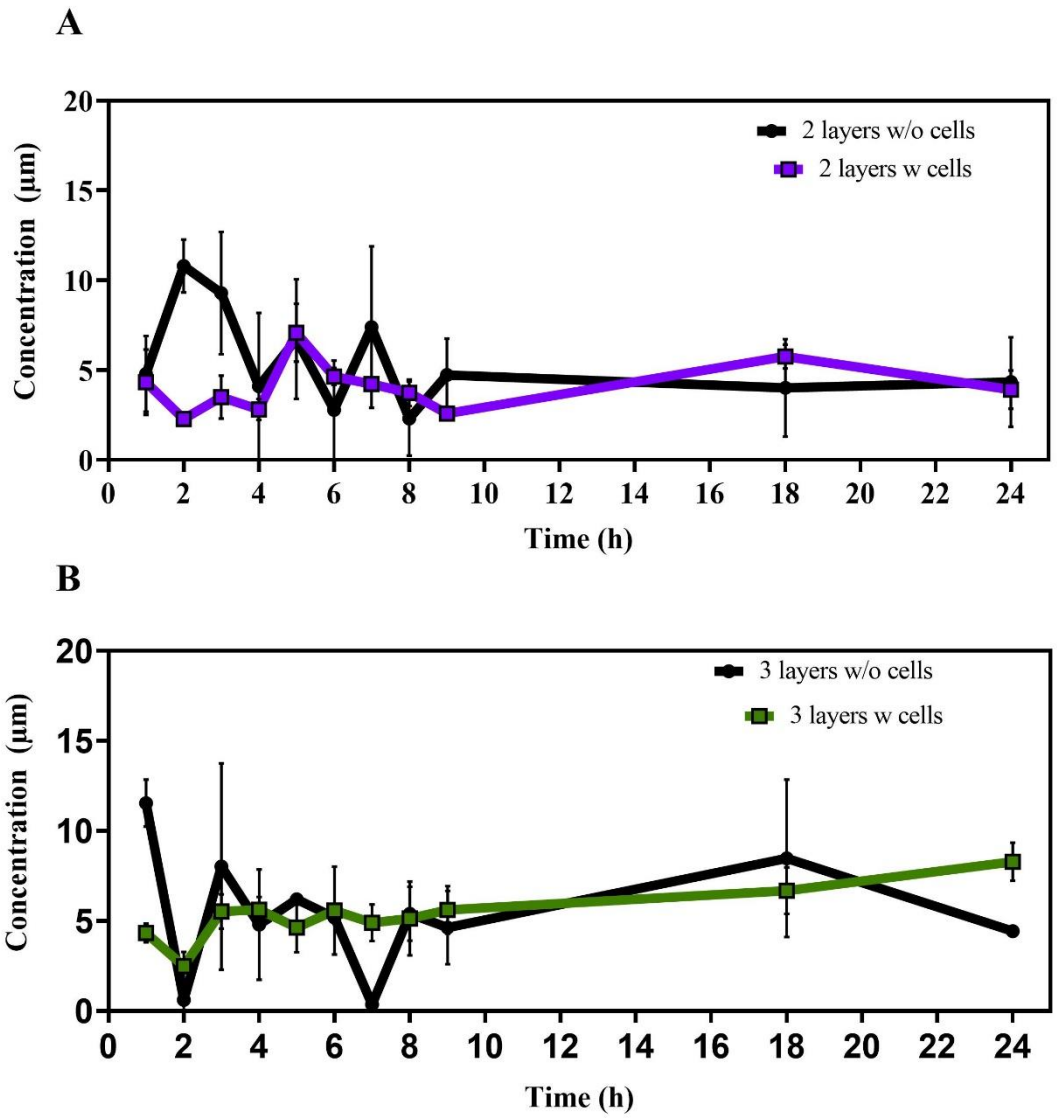

Figure 3.42. Penetrated drug concentration read from the readout channel for 24 h (n=3). Black lines indicate no-cell loaded **A)** 2- and **B)** 3- layered skin models. Purple line shows cell-loaded 2-layered cell-loaded model and green shows 3-layered cell-loaded model.

All skin model samples were imaged after 12 h **(Figure 3.43)**. Hydrogel part of skin models (dermis and hypodermis layers) were imaged. No-drug samples showed a very pale FITC-Dex signal (green) signal. Drug-tested samples showed evenly distributed green signal (Figure 3.43, *left panel*). Hydrogels were imaged with higher magnification, and it was seen that hydrogels also absorbed and

reflected the FITC-Dex signal (blue-nuclei, Figure 3.43, *right panel*). However, the FITC-Dex signal was much brighter on cell-loaded samples. Dex penetration was highest until the eighth hour. Then, drug penetration continued up to 24 h, but penetrated drug concentration was decreased. Cell-loaded 2-and 3-layered models showed a peak around 18 h after initiation of the penetration experiment. Cells may have retard the drug penetration through the skin compartments.

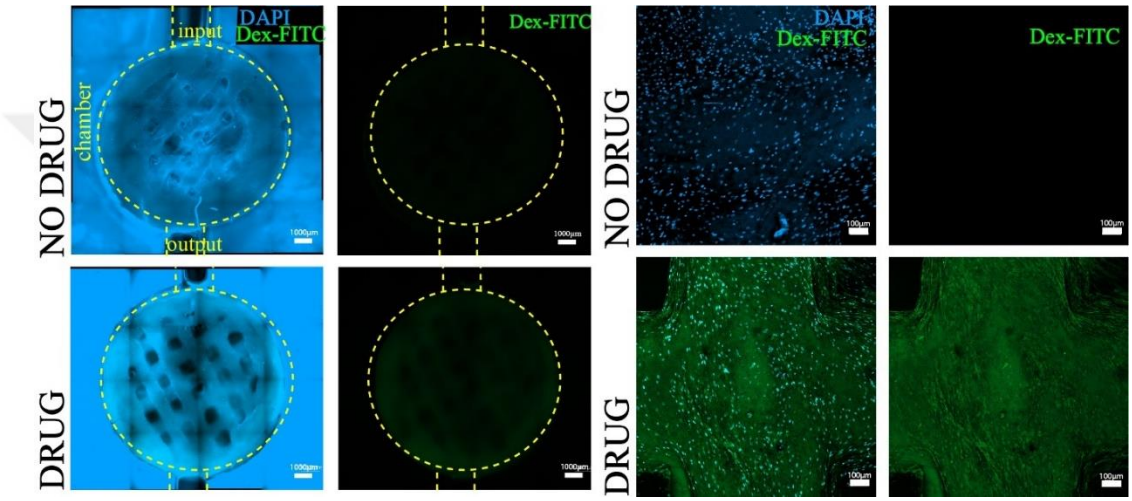

Figure 3.43. CLSM images of the hydrogel components after 24 h of drug penetration experiment No-drug components (top) and drug-loaded components (bottom) were imaged within the same fluorescence intensity (Green: FITC-Dex, cyan: nucleus).

3.9 Characterization of Room Temperature Printable Bioink

This printable bioink was aimed to support prevascularization for the skin model. HAMA hydrogel was shown to provide prevascularization motives to skin models using Human umbilical vein endothelial cells in the literature (Eke, Mangir, Hasirci, Macneil, et al., 2017). Hyaluronic acid is a natural component of extracellular matrix and abundantly present in skin and connective tissues. It has also been used in skin models for inducing wound healing, inflammation and angiogenesis (Gwon et al., 2017; Oliveira et al., 2021). Printing stability of

hyaluronic acid is low and it can be increased with methacrylation. (Poldervaart et al., 2017). In this study, a HAMA hydrogel loaded with HUVECs was going to be printed into the GelMA scaffold, mimicking vascularization of the skin. GelMA was already printed with low temperature head of the printer, therefore high temperature printer was going to use for printing HAMA motives. The lowest temperature that we can print with the high temperature head was 37 °C. Therefore, printing HAMA at room temperature was crucial. In the literature, HAMA concentrations between 1-3% (v/w) and IrgaCure 0.1% (w/v) were used (Poldervaart et al., 2017) to obtain crosslinked gels. But, in this study more than 1% HAMA could not be dissolved completely. Therefore, 1% HAMA and 0.6 % IrgaCure (as optimized with GelMA in Section 3.1.3) were used. HAMA polymer solution was UV irradiated in a culture plate for 4 s (optimized according to GelMA as they were going to be printed intertwined and successfully crosslinked. Then, polymer solution was transferred into the high temperature cartridge. Nevertheless, the viscosity of HAMA solution at 37 °C was very high and polymer solution was spilled out from the cartridge without applying any pressure. Many optimization trials were done to achieve a bioink printable at room temperature. To increase both handling and printability, first GelMA 10% (w/v) was added to the hydrogel content. Unfortunately, GelMA has a low sol-gel transition temperature and has low viscosity at room temperature. Then, alginate 4% (w/v) was also added to the hydrogel composition. Again, the alginate-GelMA-HAMA solution showed low viscosity and poor printability at room temperature. Eventually, to increase the viscosity, pre-crosslinking of the solution with $CaCl_2$ was employed (Hazur et al., 2020). 75 mM $CaCl_2$ solution was added to the polymer solution to obtain final 30 mM pre-crosslinked gel. This intervention increased the viscosity of the solution due to the ionic bonds $CaCl_2$ introduces to the alginate. The scaffold printing was paused after printing each layer and UV-crosslinking applied for 1.5 s. Although polymer solution could be successfully 3D printed and a handleable gel was obtained, HUVEC cells did not survive (Data not shown). Unfortunately, HUVEC cells were removed from the skin model so, prevascularization was not included in

the model. As a successful room temperature printable hydrogel was developed, other cell types were tested as bioink candidates. L929 and DF-ADSC coculture were successfully bioprinted. Then, a post-crosslink approach was followed to study the effect of hydrogel stiffness on the cell viability. After printing and UV-crosslinking, hydrogel was tested for 0-, 75-, and 150-mM post cross-linking with $CaCl_2$ solutions. Swelling, mechanical, rheological properties and viability of different resultant polymers were compared.

3.9.1 NMR spectra of Hyaluronic Acid and HAMA

The cross-linkable hyaluronic acid can be obtained by derivatization of hyaluronic acid with methacrylate groups. This HAMA synthesis takes place in an aqueous environment with the presence of excess methacrylic anhydride to the hydroxyl groups of HA (Skardal et al., 2010). The major drawback of the synthesis is related to the change of pH during the methacrylation reaction. During the reaction, covalently linked methacrylic ester may be hydrolyzed, or methacrylic anhydride can react with water to give methacrylic acid. This makes it harder to have control of DM of hyaluronic acid (Schuurmans et al., 2021). DM can be seen from NMR peak spectra results **(Figure 3.44)** but cannot be calculated accurately due to overlapped methyl signals of the coupled methacrylate and polymer backbone around 1.8-2 ppm (Oudshoorn et al., 2007). The appearance of two peaks in the region of 6.21 ppm and 5.75 ppm shows photocrosslinkable, unsaturated groups (Levett et al., 2014). In literature, high-performance liquid chromatography (HPLC) was performed to quantify methacrylic acid and determine DM (Poldervaart et al., 2017). Reported DM of HAMA were usually as low as 0.15% (Messager et al., 2013) and not more than 15% (Eke, Mangir, Hasirci, Macneil, et al., 2017; Oliveira et al., 2021). DM of synthesized HAMA must be low considering the low gelation under UV light. Adding a second photocrosslinkable polymer with a high DM, GelMA, increased the gelation of the polymer solution.

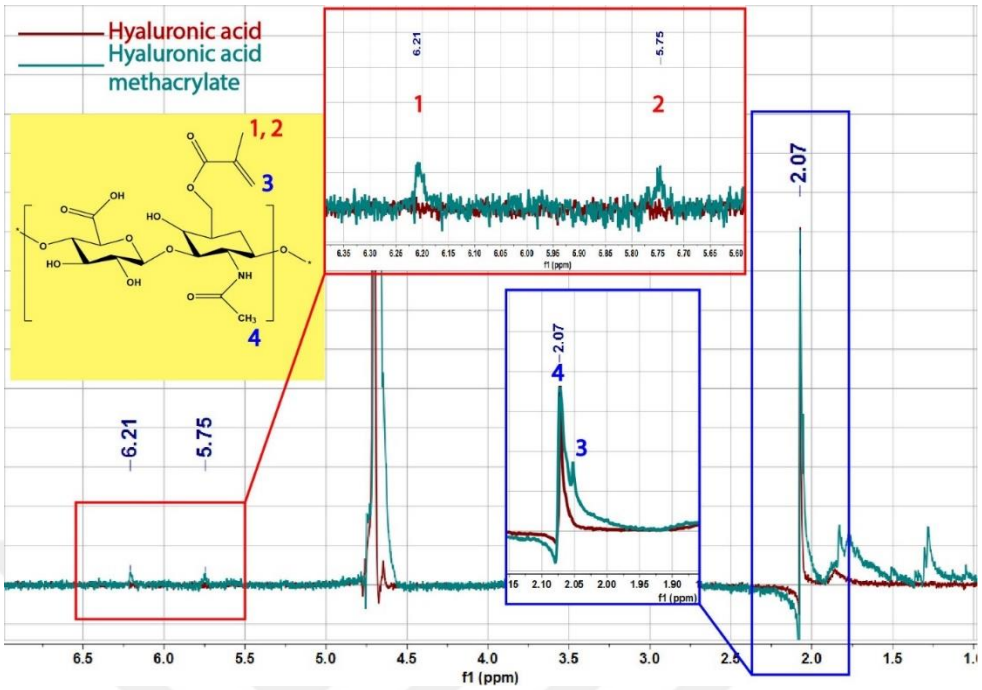

Figure 3.44. NMR spectra of hyaluronic acid and HAMA. The red line indicates Hyaluronic acid, and the green line shows gelatin HAMA (Hyaluronic acid methacrylate)

3.9.2 **Swelling of HAMA-Alg-GelMA Gels**

Swelling (weight change) properties of no post-crosslinked, 75 mM $CaCl_2$, and 150 mM $CaCl_2$ post-crosslinked HAMA-Alg-GelMA were compared for 9 h. After the post-crosslinking step (including no post-cross-linked sample), samples were UV irradiated for 4 s. Swelling analysis was performed to foresee the effect post-crosslinking on sorption properties **(Figure 3.45)**. In the literature, it was reported that decreasing the macromer concentration increased the weight change significantly in 5%, 10%, and 15% (w/v) GelMA concentrations (Jason W Nichol et al., 2010).

In a study, increasing $CaCl_2$ crosslinking concentrations led to a reduction in swelling properties in gelatin-alginate polymer solutions. Low crosslinker concentration was linked to higher swelling of the hydrogel. Also, they tested decreasing the alginate ratio in polymer solution and this led to formation of mechanically poor hydrogels which start dissolving 5 h after initiation of swelling

test. This decrease was attributed to the dissolution of polymer. They concluded the equilibrium of the alginate-gelatin hydrogels significantly dependent on crosslinker concentration and hydrogel composition (Saarai et al., 2011). Likewise, UV crosslinking of GelMA and HAMA increased the concentration of polymer and decreased the swelling compared to %10 GelMA concentration (Section 3.1.4, nearly 97% swelling in 12 h). This likely due to the increasing cross-linking density limiting the swelling capabilities of the hydrogel. Hydrogel swelling was presented as an indicator of the degree of crosslinking in the gel in a study (Bencherif et al., 2008). Post-crosslinking also significantly changed the swelling properties. No post-crosslinked sample swelling was twice higher compared to the 75 mM $CaCl_2$ cross-linked sample, and the 75 mM sample was twice higher than 150 mM $CaCl_2$ in terms of swelling after 9 hours of incubation. In literature, swelling tests were often performed after 12 or 24 h of incubation for hyrogels to reach equilibrium (Möller et al., 2011). But, there are studies showing approxametly 5 h is enough to reach the equilibrium state (Saarai et al., 2011). No post-crosslinked sample reached equilibrium in 6 h **(Figure 3.45)**. Post cosslinked samples did not reach equilibrium after 9 h which could be due to higher crosslinking density of the hydrogels. Similarly, Saarai et al reported that longer time was needed for the hydrogels crosslinked with higher conecntration of $CaCl_2$ samples to reach equilibrium state.

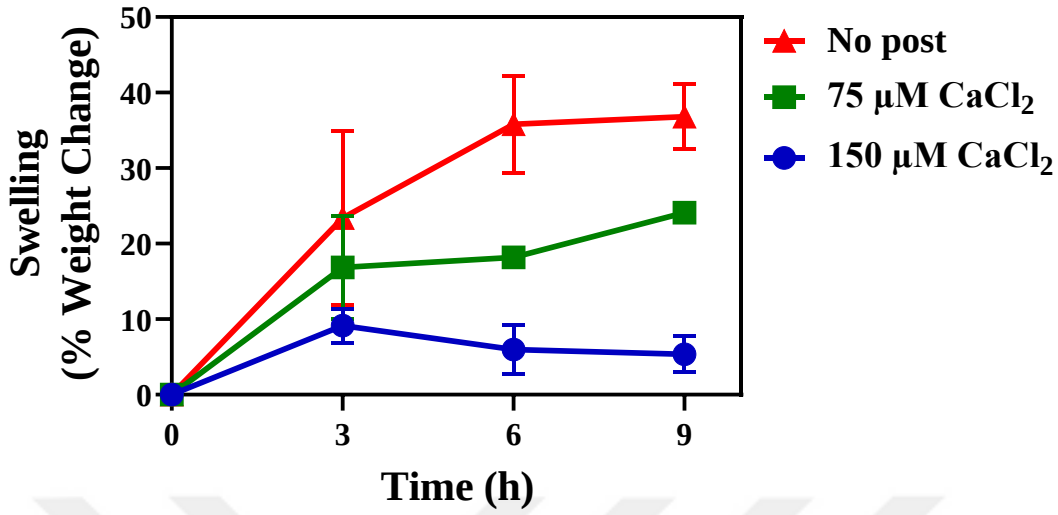

Figure 3.45. Swelling of HAMA hydrogels post-crosslinked with different concentrations of $CaCl_2$. GelMA (10%, w/v), alginate (4%, w/v), HAMA (0.1%, w/v), IrgaCure (0.6% w/v) were dissolved in DMEM High Glucose. 30 mM $CaCl_2$ pre-crosslinking was applied. The polymer solution was UV irradiated for 4 s. No post-crosslinking hydrogel was prepared as the control group. Then, irradiated hydrogels were incubated in 75, or 150 mM $CaCl_2$. Samples were tested for swelling up for nine hours at 37°C.

3.9.3 Mechanical Characterization of HAMA-Alg-GelMA Gels

Uniaxial compression test was performed on the 30 mM $CaCl_2$ pre-crosslinked HAMA-Alg-GelMA hydrogel slabs which were post-crosslinked with different concentrations of $CaCl_2$ (75 and 150 mM $CaCl_2$). No-post cross-linked, hydrogels were used as the control. Young Moduli of no-post cross-linked, 75 mM $CaCl_2$ and 150 mM post cross-linked groups were 0.014±0.002 MPa, 0.019±0.003 MPa, and 0.037±0.004 MPa, respectively ($n \geq 3$) **(Figure 3.46)**. The no-post cross-linked sample had the lowest Young's Modulus. The moduli increased as the post-crosslinking $CaCl_2$ concentration was increased. There was no significant difference between 75 mM $CaCl_2$ post-crosslinked and no-post cross-linking groups. Moduli of 150 mM $CaCl_2$ post-crosslinked samples, on the other hand, was significantly higher than the moduli of 75 mM $CaCl_2$ post-crosslinked and no post-

crosslinked hydrogel groups. In a study, increasing crosslinking density of alginate in alginate-GelMA hydrogels also increased the compressive modulus. However, such hydrogels with higher mechanical properties had undesirable high viscosity which resulted in high shear forces on encapsulated cells during extrusion (Giuseppe et al., 2018).

Results showed that mechanical properties of 3D printed alginate-based hydrogels could be tailored by post-crosslinking. Cell behaviors such as proliferation, migration, and differentiation can be affected by mechanical properties (Pelham & Wang, 1997; Thankam & Muthu, 2014). A study showed post printing crosslinking of alginate-gelatin blend with 300 mM $CaCl_2$ increased the gel stiffness but had no discernable effect on cell viability. The 5% Alg-6% Gel, which had the lowest viscosity and mechanical strength of the three blends, had the highest cell viability (96%) (Giuseppe et al., 2018). Another study showed increasing HAMA polymer concentrations (1% to 3% (w/v)) increased the storage modulus of UV crosslinked HAMA hydrogels. When bone marrow derived mesenchymal stem cells were encapsulated into HAMA, cell fate was influenced by the varying mechanical properties (1.2 kPa to 10.7 kPa). Increasing rigidity altered cell morphology from elongated to round cells, overall cell viability was decreased while osteogenic differentiation increased (Poldervaart et al., 2017). Another study showed the effects of PDMS matrix stiffness on ADSC behaviour (T. Zhang et al., 2018). ADSCs were seeded to PDMS-derived matrices with varying degrees of stiffness to study cell morphology and adipogenic differentiation. Stiffness of matrices was between 134 kPa and 1.4 kPa. Stiffer matrices increased cell spreading area dramatically and adopted a polygonal shape. ADSCs on soft matrices showed a round morphology and allowed more adipogenic differentiation in the presence of differentiation medium. The difference of two studies with opposing results may be explained with the second article's reported concerns. They reported the viscoelastic behaviour of low stiff PDMS which might influence stem cell differentiation. To sum up, characterization of material is crucial to understand cell behaviour.

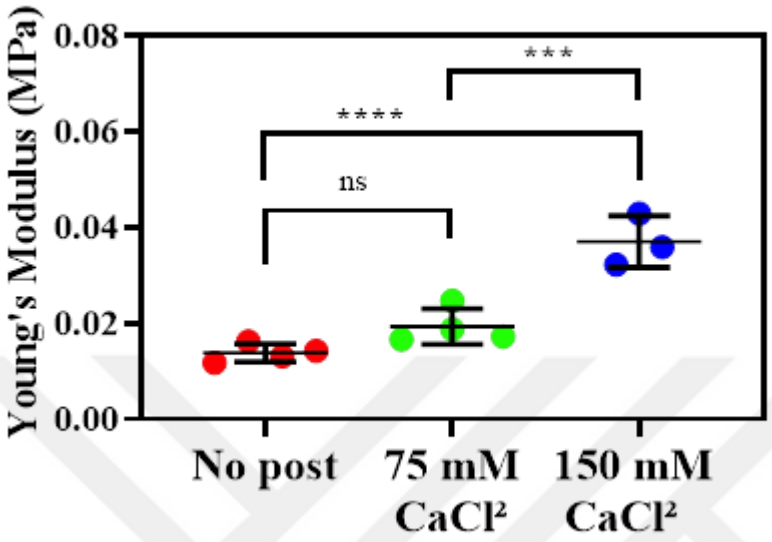

Figure 3.46. Young's moduli of HAMA-Alg-GelMA concentrations (0.1 %, 4 %, 10 %) (w/v) with 0.6 % Irgacure (w/v) irradiated for 4 s, and post-crosslinked with different concentrations of $CaCl_2$. Young's moduli were measured by uniaxial compression tests n≥ 3. Dots represent the Young's Modulus of each sample (Two-way ANOVA, *p≤0.0332, ** p≤0.0021, *** p≤0.0002, ****p <0.0001).

3.9.4 Rheological Properties of GelMA and HAMA-Alginate-GelMA Bioinks

Rheological properties of 5 different bioink materials of gelatin, alginate, and HAMA and their blends dissolved in DMEM High Glucose were studied **(Figure 3.47)**. The storage modulus (G'), loss modulus (G'') and complex viscosity of polymer solutions and pre-crosslinked polymer were determined by oscillatory rheological measurements. Materials with different concentrations were tested to observe the effect of hydrogel concentration on rheological properties, and printability of the materials. The ideal bioink must be extruded through a thin nozzle. Therefore, cell-based micruextrusion printing systems must have a relatively higher viscosity, robust shear-thinning behaviour and fast post-

processing after printing (T. Gao et al., 2018). Bioinks tested were GelMA (10%, w/v), alginate (4%, w/v), GelMA (10%, w/v) & alginate (4%, w/v), GelMA (10%, w/v), alginate (4%, w/v) & HAMA (0.1%, w/v), GelMA (10%, w/v), alginate (4%, w/v) & HAMA (0.1%, w/v) & 30 mM $CaCl_2$ pre-crosslinked.

In order to analyze loss and storage moduli, oscilation frequency was altered **(Figure 3.47A and B)** At low frequencies, the properties at low change of stress can be seen and high frequencies represent characteristics at high change of stress. As shown on **Figure 3.47A and C** precrosslinked alginate, GelMA, HAMA polymer solution had the highest storage modus. The mechanical spectrum of GelMA/ HAMA/ alginate hydrogel showed the highest G' and G'' with no frequency or temperature dependence **(Figure 3.47A and D)**. G' of the semi-IPN gel was higher than G' of pure alginate, HAMA and GelMA hydrogels. In a study, similar results were reported. Photocrosslinked GelMA, alginate methacryate and HAMA hydrogels were mixed in different ratios and their loss and storage modulus were investigated versus deformation percantage (Möller et al., 2011). Alginate was shown the strongest material with the highest rigidity. GelMA was the softest material but it absorbed applied forces better. HAMA on the other hand, has a drastically lower tendency to change its polymeric network structure.

GelMA (10%, w/v), and alginate (4%, w/v) showed similar low storage moduli on their own but when (GelMA (10%, w/v) & alginate (4%, w/v)) were blended they acted synergistically, and the loss and storage moduli increased independent from frequency or temperature **(Figure 3.47 A-D)**. Addition of HAMA to GelMA-Alginate decreased both loss and storage modulus but resulted in more decrease in the storage modulus **(Figure 3.47A and B)**. Same trends were followed in higher frequiences. At higher frequencies pre-crosslinked gels showed the highest stability, while gelatin and alginate-only gels had the lowest. Addition of HAMA (GelMA (10%, w/v) & alginate (4%, w/v) & HAMA (0.1%, w/v) decreased the storage modulus and overall viscosity. At high frequencies, HAMA-GelMA-Alginate polymer solution rigidity increased and it was as high as GelMA-Alginate

polymer solution. Increasing the concentration of bioink raised the storage modulus, and overall viscosity. According to a study, higher loss tangent (G¨/G') was attributed to more uniform extrusion and lower loss tangent owing to a better structural integrity. The viscosity, storage and loss moduli significantly increased with precrosslinking using $CaCl_2$. Higher viscosity requires higher extrusion pressure which may led to higher shear stress on cells and result in cell damage. It was reported that above 600 Pa viscosity, cell viability dropped to 60% from 90%. This was achieved by increasing alginate concentration from 4% (v/w) to 6% (v/w). The effect of pre-crosslinking on visscosity was shown. Also, they mentioned the optimal viscosity for alginate was achieved with 4% (w/v) alginate with 40 mM $CaCl_2$. (T. Gao et al., 2018; Tabriz et al., 2015). In this study, 30 mM $CaCl_2$ was found optimal for pre-crosslinking, which was in agreement with the literature because viscosity was increased by addition of GelMA and HAMA along with 4% (v/w) $CaCl_2$ pre-crosslinking. Shear stress may affect cell viability and proliferation on long term (K. Zhang et al., 2017). $CaCl_2$ precrosslinked sample showed relatively higher viscosity compared to the other polymer solution samples for bioink and showed similar shear values.

According to a study, GelMA and HAMA hydrogels had viscosity lower than 100 Pa, which led to very fluid behaviour and lack of shape retention (Chopin-Doroteo et al., 2021; Duan et al., 2014). Our non-precrosslinked had similar viscosity values (<100 Pa), and could not be printed alone or together witout precrosslinking. GelMA and alginate showed viscosity, close to 100 Pa. We have not tried 3D printing 10% GelMA (w/v) in this study, but 15% (w/v) could succesfully printed due to higher concentration of GelMA. Viscosity is related to polymer concentration, temperature and molecular weight of the polymer. Formulations with viscosity higher than 10^4 Pa have been reported since these can not be deposited smoothly (Duan et al., 2014). Therefore, printable bioink has viscosity between 97.5 Pa- 380 Pa viscosity and shear between 2.77- 0.58 (1/s) **(Figure 3.48A)**. Although printing shear was not measured in this study, a printable shear was succesfully achieved by changing printing parameters. As mentioned, a

balance between G'- G'' and viscosity is required for extrusion during bioprinting to avoid cell damage. Thus, extrudibility is an important parameter and need to be evaluated carefully because of different sensitivity of the cell types. A quantitative correlation between moduli and extrusion pressure or a standardized method to evaluate bioink printability have not been reported. According to literature, stiff solid bioink at room temperature may not be ideal for bioprinting (T. Gao et al., 2018; Malda et al., 2013). Gelatin shows solid-like characteristic (G' dominates) and alginate shows liquid-like characteristics **(Figure 3.48A).** Nevertheless, alginate (4 % (v/w)) and GelMA (10% (v/w)) were in viscous-liquid region in this thesis **(Figure 3.48B),** and could not be printed.

Most part of the pre-crosslinked polymer solution was placed in the stiff solid phase, it was printed succesfully with good cell viability. Viscous-liquid region of pre-crosslinked polymer solution was under 500 G' and G''. Taking consideration of decreased viability above 600 MPa mentioned before (T. Gao et al., 2018; Tabriz et al., 2015) together with **Figure 3.47C,** similar G' and G'' were achieved at room temperature. Hence, a room temperature printable, tunable bioink was produced.

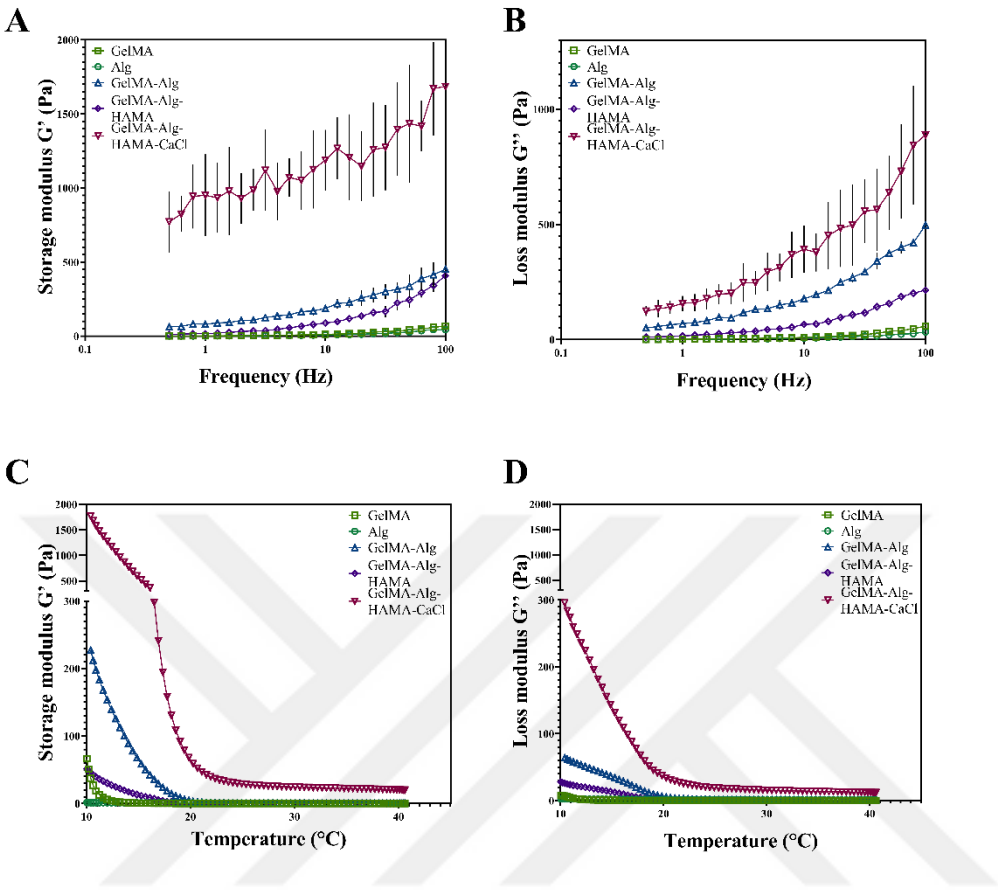

Figure 3.47. Rheological properties of bioink materials of gelatin, alginate, and HAMA and their blends dissolved in DMEM High Glucose. GelMA (10% (w/v)) (light green); alginate 4% (w/v) (turquoise), GelMA 10% (w/v)& alginate 4% (w/v) (blue); GelMA 10% (w/v)& alginate 4% (w/v)& , HAMA 0.1 % (w/v) (purple); GelMA 10% (w/v)& alginate 4% (w/v)& , HAMA 0.1 % (w/v) and 30 mM precrosslinking with $CaCl_2$ (pink) samples were studied. **A)** Varying storage modulus (G') and **B)** Varying loss modulus (G") with frequency. **C)** Varying storage modulus (G') and **D)** Varying loss modulus (G") with temperature.

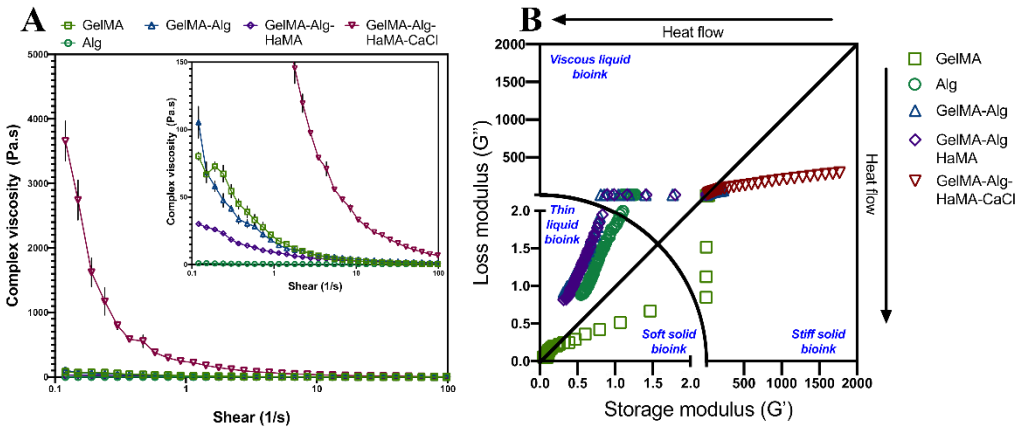

Figure 3.48. Rheological properties of bioink materials of gelatin, alginate, and HAMA and their blends dissolved in DMEM High Glucose. GelMA (10% (w/v)) (light green); alginate 4% (w/v) (turquoise), GelMA 10% (w/v)& alginate 4% (w/v) (blue); GelMA 10% (w/v)& alginate 4% (w/v)& , HAMA 0.1 % (w/v) (purple); GelMA 10% (w/v)& alginate 4% (w/v)& , HAMA 0.1 % (w/v) and 30 mM precrosslinking with $CaCl_2$ (pink) samples were studied. Insert figure caption here **A)** Complex viscosity changing with the shear. **B)** Phase properties of materials with changing storage modulus vs loss modulus.

3.9.5 Viability of L929 fibroblasts encapsulated in HAMA-Alg-GelMA Slab Gels

This hydrogel was initially prepared as a bioink for HUVEC. Despite prolonged and repeated trials for developing a printable hydrogel for HUVEC culture, HUVEC cells did not survive in the printed hydrogels (Data not shown). Thus, produced HAMA-Alg-GelMA ink was 3D printed with L929 fibroblasts, FBs, and ADSCs and succeeded.

GelMA (10%, w/v), alginate (4%, w/v), HAMA (0.1%, w/v), and IrgaCure (0.6 % w/v) were dissolved in DMEM High Glucose. This solution was pre-crosslinked with 75 mM $CaCl_2$ and $3x10^6$ cells/mL L929 cells were added to the solution, and casted into PDMS-coated 48 well plate to prepare 5 mm thick cell-loaded slab gels

were produced. Samples were UV irradiated for 4 s. No post-crosslinking, 75, and 150 mM $CaCl_2$ post-crosslinking were applied and a live-dead analysis was performed. Percentage of viable cells observed in both groups was above 95% at each time point. High cell viability in the bioink was achieved in all post-crosslinking conditions witouth printing **(Figure 3.49)**.

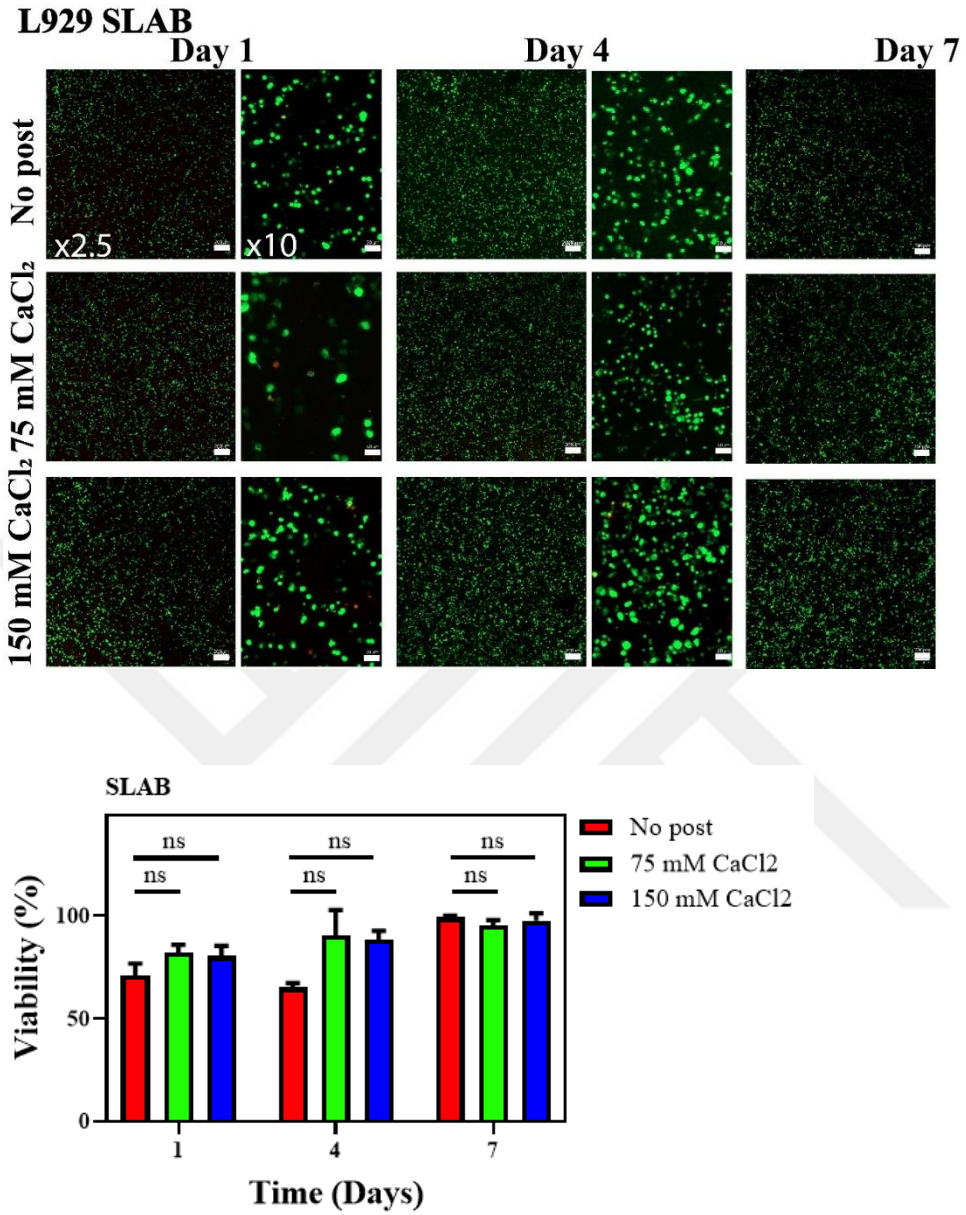

Figure 3.49. Cytotoxicity of HAMA gels post crosslinked with different concentrations of $CaCl_2$. GelMA (10%, w/v), alginate (4%, w/v), HAMA (0.1%, w/v), IrgaCure (0.6% w/v) were dissolved in DMEM High Glucose and 30 mM $CaCl_2$ was added for precrosslinking. Solution was casted into PDMS coated 48 well platesand UV irradiated for 4. Viability of cells obtained from live dead staining. **A)** Confocal microsopy images of L929 fibroblasts in HAMA-Alg-GelMA slab gels after live-dead staining No post-crosslinked (top), 75 mM $CaCl_2$ pre-crosslinked (middle), and 150 mM $CaCl_2$ pre-crosslinked (bottom) samples were cultured (CLSM, Scale bar: 200 μm for 2.5X and 50 μm for 20X images Green: Live, Red: Dead,). **B)** Percentage of live cells on slab gels obtained from live dead staining (n=3), One-Way ANOVA *p≤0.0332, ** p≤0.0021, *** p≤0.0002, ****p <0.0001).

Continuing experiments were performed with $1x10^6$ cells/mL bioinks and compared with $3x10^6$ cells/mL L929 culture during one week of incubation. This was done due to lack of sufficient number of L929 cells (**Figure 50)**. In literature mostly $1x10^6$ cells/ml at maximum is preferred as the cell density (Khoshfetrat et al., 2009). Phalloidin and DAPI stainings were applied to L929 slabs. Cell morphology changed when seeding density was. Compared to $1x10^6$ cells/ml culture, there was a further increase in cell number after day 4 at the $3x10^6$ cells/ml group. In a study, the effect of cell distance on the cellular function and morphology was investigated (Venugopal et al., 2018). They reported that growth arrest remains for low cell density (1000 cells/cm^2) but not in crowded culture (4000 cells/cm^2). They mentioned longer cell-to-cell distances eliminated the possibility of a direct contact of ADSC cells. But stiffness is the main factor in cell spreading. It was also shown that spread cells deposited extracellular matrix and increased stiffness. The effect of cell seeding on stiffness was not studied here. They also compared the cell morphology of low (1000 cells/cm^2) and crowded culture (4000 cells/cm^2) of 3T3 fibroblast cells and find similar results with ADSC. Low seeding density showed round morphology and did not spread but higher concentration formed cell networks. Similar behaviour was seen in this study. When seeding density of $1x10^6$ was used round and coalesced cells were observed until day 4 (**Figure 3.50)** while $3x10^6$ culture formed network on day 7. But, in lower cell density group, cell-to-cell distance was decreased, and network was formed on day 7.

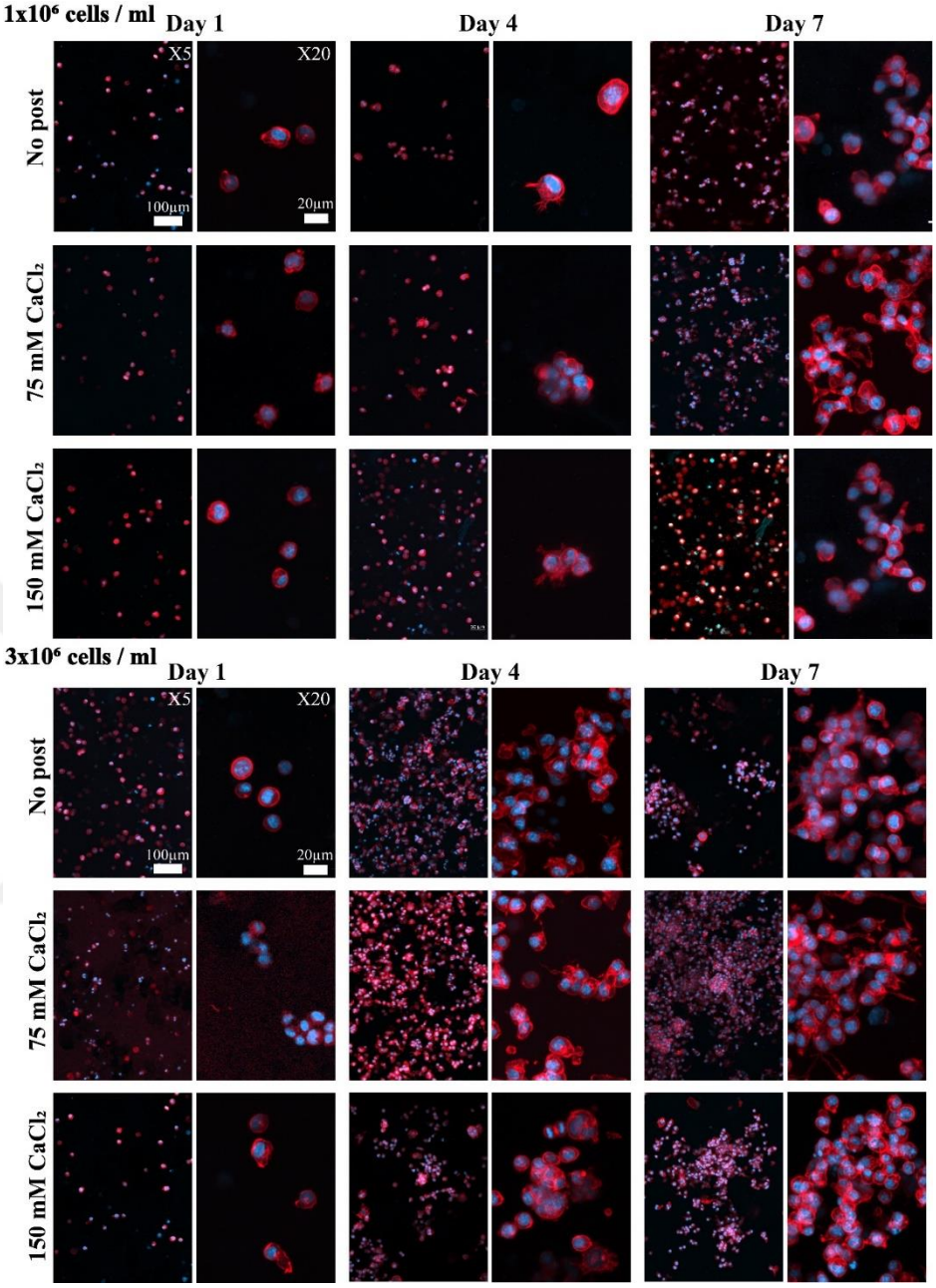

Figure 3.50. Phalloidin. and DAPI staining images of L929 fibroblasts in slab gels with different cell seeding densities. GelMA (10%, w/v), alginate (4%, w/v), HAMA (0.1%, w/v), IrgaCure (0.6% w/v) were dissolved in DMEM High Glucose. 30 mM $CaCl_2$ pre-crosslinking was applied for all of slab gels. Solution was casted into PDMS coated 48-well plates and UV irradiated for 4s. On the top panel shows slab gels containing $1x10^6$ cells/mL, and the bottom panel shows slab gels loaded with $3x10^6$ cells/mL which were post-crosslinked with different concentrations of $CaCl_2$. All of the slab gels were pre-crosslinked (CLSM, Scale bar: 100 µm for 2.5X and 20 µm for 20X images Cyan: phalloidin, magenta: nucleus).

3.9.6 Comparison of FB-ADSC Cells Encapsulated in HAMA-Alg-GelMA Slab Gels

After defining L929 morphology in GelMA (10%, w/v), alginate (4%, w/v), HAMA (0.1%, w/v), and IrgaCure (0.6 % w/v) in DMEM High Glucose polymer solution, viability of FB-ADSC coculture was studied. This solution was also cross-linked with the 30 mM $CaCl_2$ (pre-crosslinking). FB: ADSC (1:1) cells were prepared as $1x10^6$ cells/mL and encapsulated into the solution to produce cell-loaded slabs. Samples were UV irradiated for 4 s. No post-crosslinking, 75, and 150 mM $CaCl_2$ post-crosslinked samples were prepared, and Phalloidin and DAPI staining were performed **(Figure 3.50)**. No cell morphology change was observed for any cell type, seeding density or $CaCl_2$ concentration used in post-crosslinking on day 1 **(Figure 3.51 3D printed and slab).** Increasing crosslinking density of hydrogels in which FB-ADSC were encapsulated increased the cell-to-cell distances on Day 4. Network formation started in no post-crosslinked hydrogels. Cells were round but started coalescating in 75 mM post crosslinked hydrogels. Cells in 150 mM post-crosslinked gels were round shaped and apart from eachother. On day 7, cell network was formed in all hydrogel groups, but it was denser in the 150 mM post-crosslinked hydrogels. Also cells were closer to each other in 75 mM post-crosslinked hydrogels compared to no post-crosslinked ones.

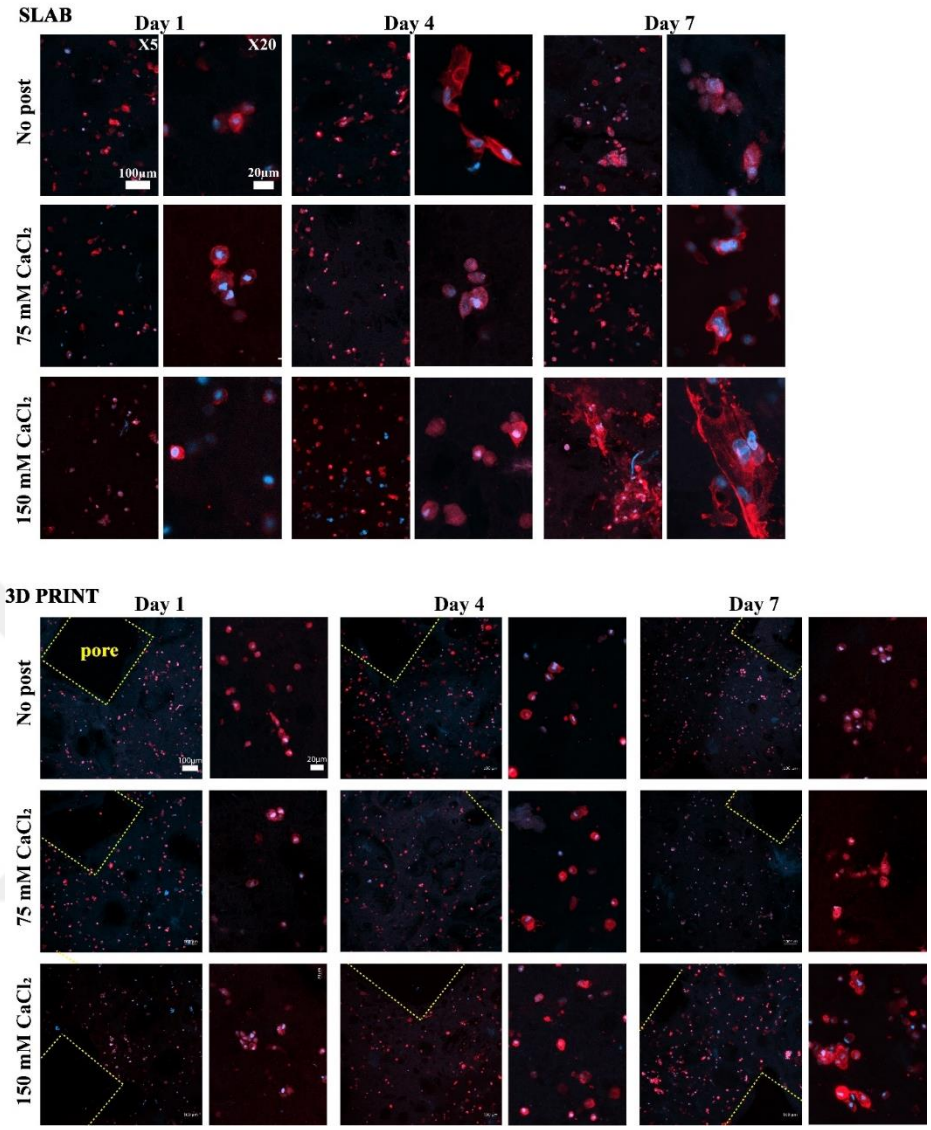

Figure 3.51. Phalloidin-DAPI images of the ADSC: FB (1:1) in slab and 3D printed gels which were postcrosslinked with different concentrations of $CaCl_2$ at days 1,4 and 7 after Phalloidin and DAPI stainings. GelMA (10%, w/v), alginate (4%, w/v), HAMA (0.1%, w/v), IrgaCure (0.6% w/v) were dissolved in DMEM High Glucose. 30 mM CaCl2 pre-crosslinking was applied. Solution was casted into PDMS coated 48-well plates and UV irradiated for 4s. No post-crosslinked (top), 75 mM $CaCl_2$ pre-crosslinked (middle), and 150 mM CaCl2 pre-crosslinked (bottom) samples were cultured (CLSM, Scale bar: 100 µm for 2.5X and 20 µm for 20X images Cyan: phalloidin, magenta: nucleus).

3.9.7 Viability of FB-ADSC Encapsulated in 3D printed HAMA-Alg-GelMA Gels

GelMA (10%, w/v), alginate (4%, w/v), HAMA (0.1%, w/v), and IrgaCure (0.6 % w/v) were dissolved in DMEM High Glucose. This solution was precrosslinked with 30 mM $CaCl_2$. FB: ADSC (1:1) cells were prepared as $1x10^6$ cells/mL, and encapsulated into the 3D printer's cartridge, and printed. Samples were UV irradiated for 4 s. No post-crosslinking, 75, and 150 mM $CaCl_2$ post-crosslinked samples were prepared. $1x10^6$ cells/mL FB: ADSC (1:1) HAMA-Alg-GelMA Slabs and 3D bioprinted scaffolds were prepared and cultured. Live-dead and Phalloidin-DAPI stainings were performed on days 1, 4, and 7 **(Figures 57-59)**. Cell-loaded scaffolds sustained integrity more than 14 days of incubation (Data not shown). Cells proliferated in each post-crosslinking concentration. Cells were spread in the scaffolds for both concentrations of $CaCl_2$. Increased post-crosslinking concentration eased the handleability of the scaffolds.

The cell viability observed in slab and 3D printed groups was compared to understand the the effect of printing. The cell viability in 3D printed group was slightly higher than observed in the slab group. This might be the effect of shear, as mentioned in **Section 3.3.3,** might change the cell fate permanently. The viability of all 3D printed sample groups followed an increasing trend and finally reached above 95% viability. No significant difference between values was found among different samples except 3D printed Day 4 sample, which may be due to an experimental error. Phalloidin and DAPI staining were performed on $1x10^6$ cells/mL loaded ADSC: FB (1:1) HAMA-Alg-GelMA slabs and 3D printed scaffolds **(Figure 3.52 and 3.53)**. All 3D printed samples protected sharp pore edges without degrading for 7 days. Very little cell damage occurred by printing cells at room temperature and shear of 3D printing procedure effected the cell growth positively. A tunable bioink for producing scaffolds with different stiffness, cell morphology was printed, and good viability was achieved **(Figure 3.54)**. This

bioink and post-processing methods can be a useful tool for soft tissue engineering applications.

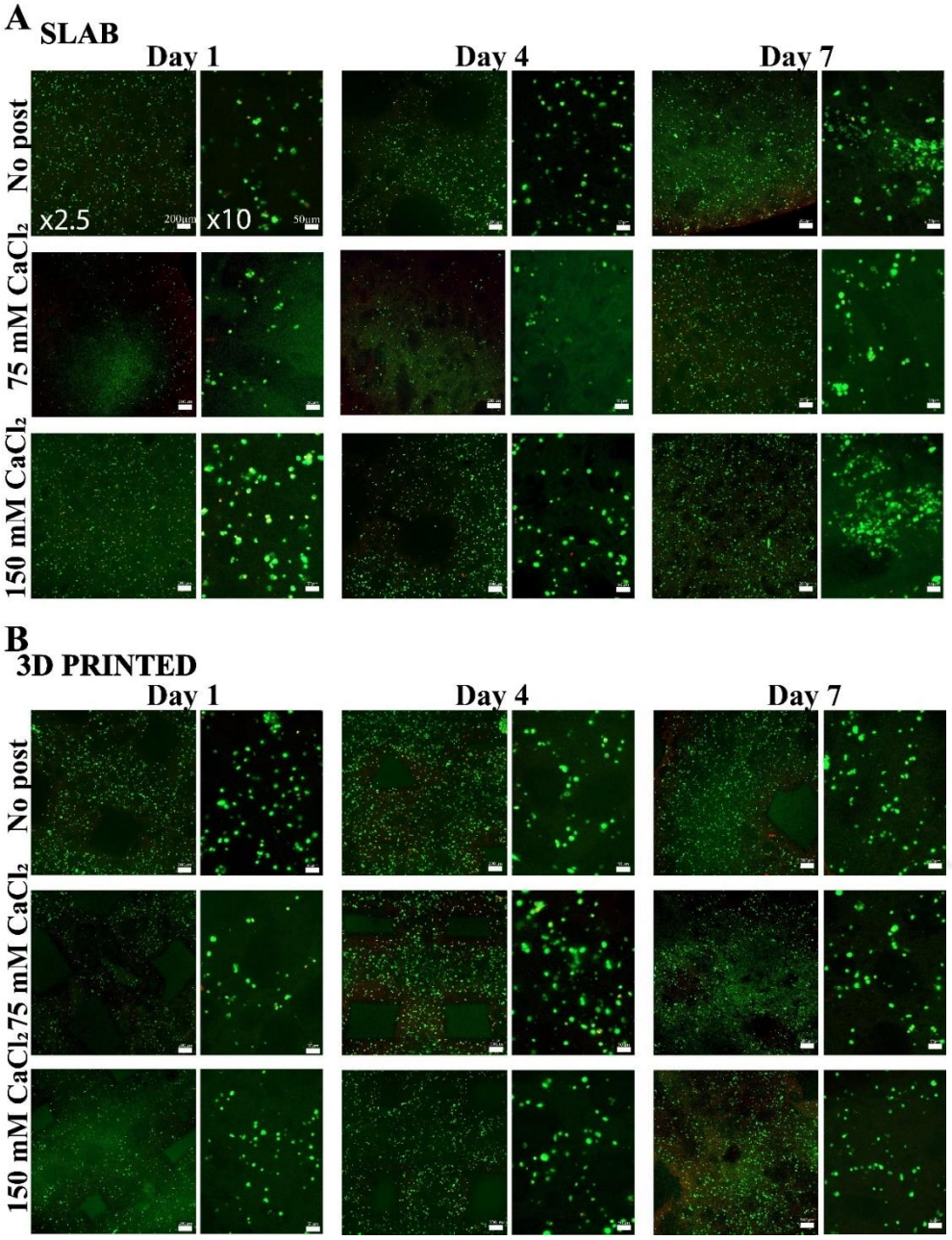

Figure 3.52. Live-dead images of the ADSC:FB (1:1) in slab gels which were postcrosslinked with different concentrations of $CaCl_2$. GelMA (10%, w/v), alginate (4%, w/v), HAMA (0.1%, w/v), IrgaCure (0.6% w/v) were dissolved in DMEM High Glucose. 30 mM $CaCl_2$ pre-crosslinking was applied. The solution was UV irradiated for 4. No post-crosslinked (top), 75 mM $CaCl_2$ pre-crosslinked (middle), and 150 mM $CaCl_2$ pre-crosslinked (bottom) samples were cultured. A) Live-dead staining of the ADSC: FB (1:1) slabs B) viability percentage of the 3D Printed ADSC: FB (1:1) soft tissue scaffolds (CLSM, Scale bar: 200 µm for 2.5X, 50 µm for 10x image, Green: live, red: dead).

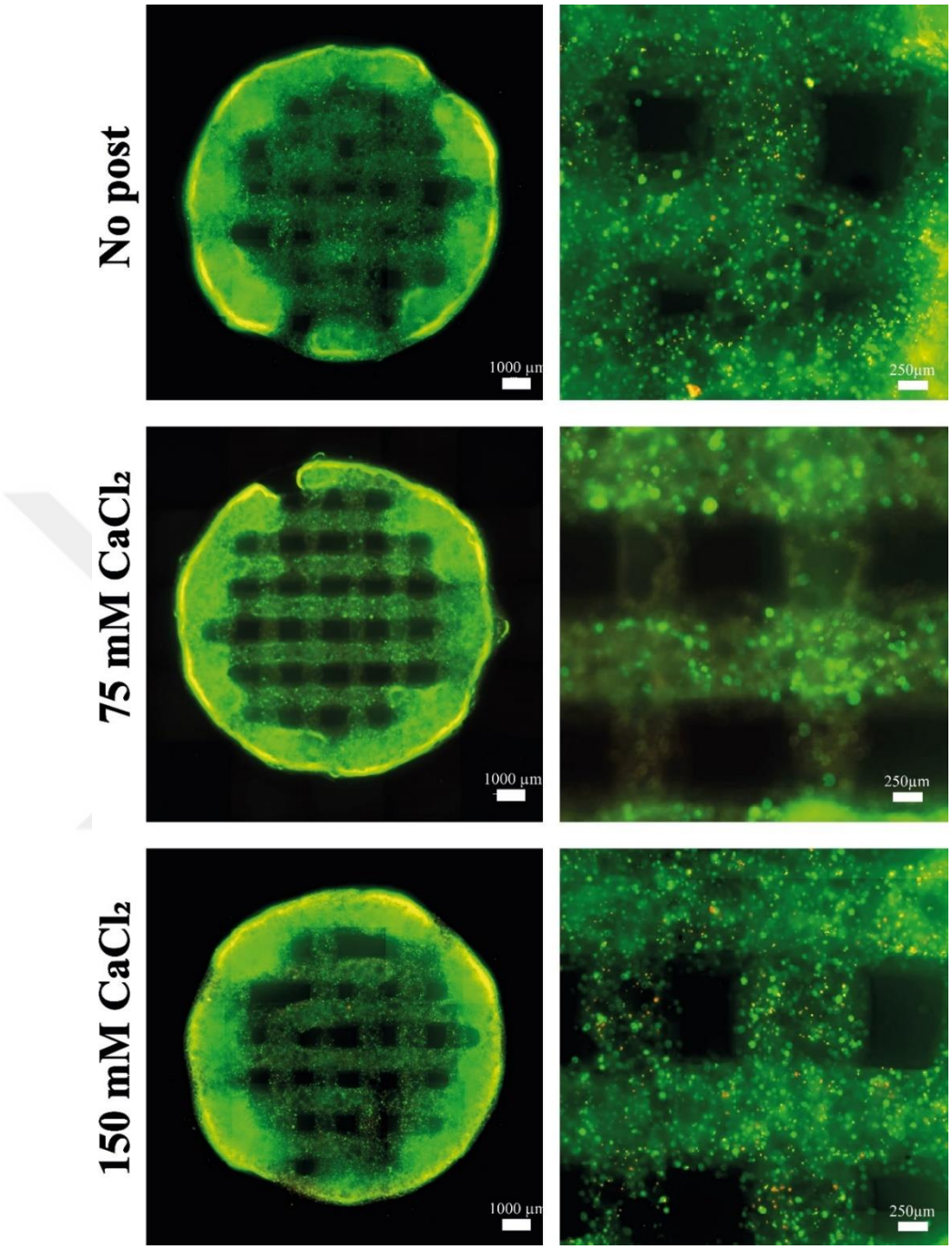

Figure 3.53. Live-dead images of the full HAMA scaffold. ADSC:FB (1:1) in 3D printed gels. GelMA (10%, w/v), alginate (4%, w/v), HAMA (0.1%, w/v), IrgaCure (0.6% w/v) were dissolved in DMEM High Glucose. 30 mM $CaCl_2$ pre-crosslinking was applied. Solution was UV irradiated for 4. No post-crosslinked (top), 75 mM $CaCl_2$ pre-crosslinked (middle), and 150 mM $CaCl_2$ pre-crosslinked (bottom) samples were cultured (CLSM, Scale bar: 1000 µm for overall scaffold image, 250 µm for zoomed image, Green: live, red: dead).

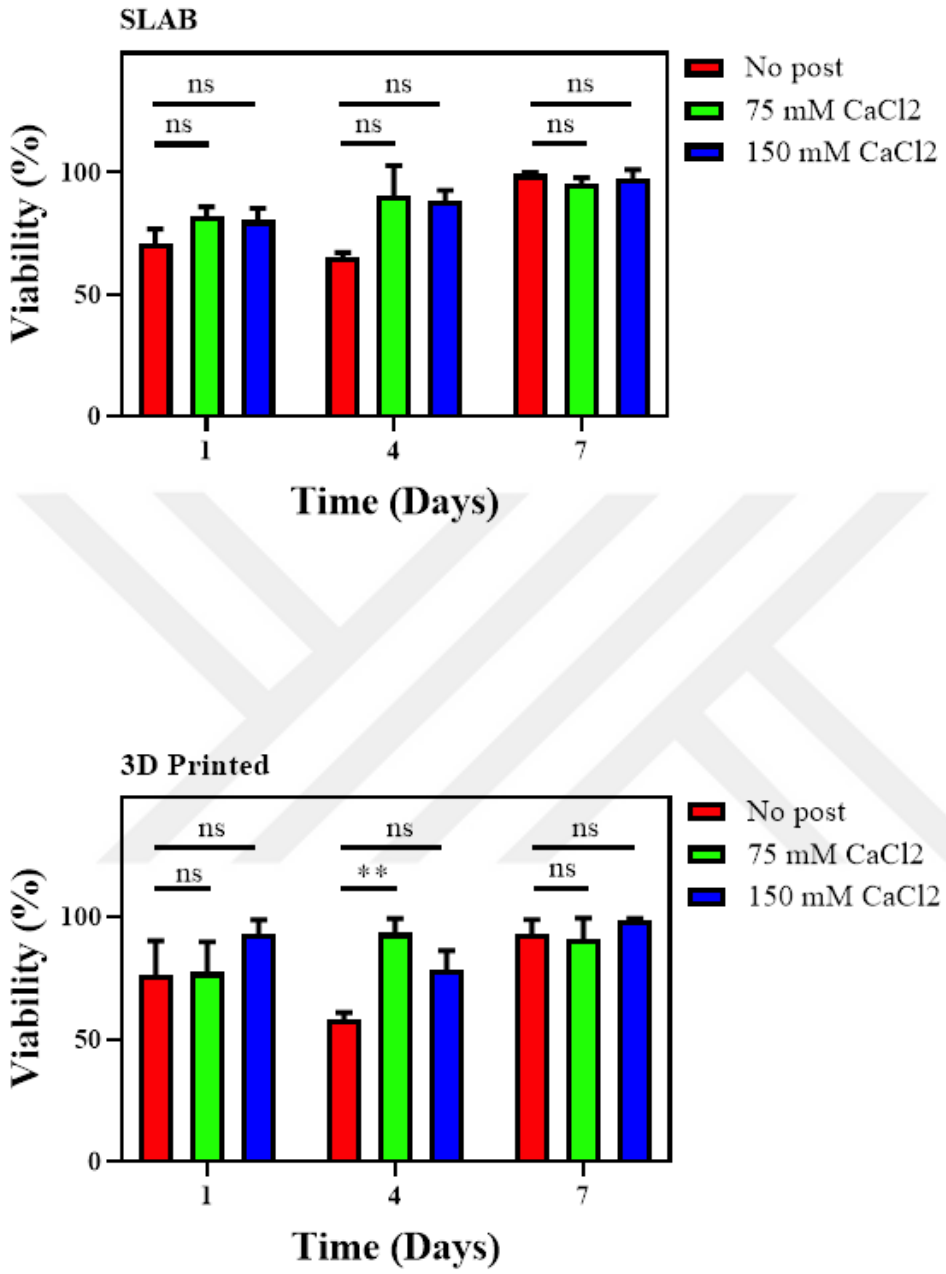

Figure 3.54. Live-dead staining results of **A)** slab and **B)** 3D bioprinted ADSC: FB (1:1) scaffolds. (n=3), One-Way ANOVA *p≤0.0332, ** p≤0.0021, *** p≤0.0002, ****p <0.0001.

CHAPTER 4

CONCLUSION

Human-based skin systems is an urgent need due to high amounts of demand at pharmaceutical industry, cosmetic research, and toxicology testing of their chemical ingredients. To date, considerable effort has been made to identify the potentially toxic or skin sensitizing on developed skin models. In this study tissue engineering methods were used to closely mimic the native ultrastructure of the human skin by combining 3D bioprinting and microfluidics methods. The micro-bioreactor designed in this study included three features: i- air-liquid interface for epidermal keratinocyte layer maturation, ii- soft tissue chamber for the dynamic culture of dermal and hypodermal layers, and iii- sub-reservoir for drug penetration analysis. Percentage of GelMA (15% (v/w) and photoinitiator (IrgaCure, 0.6% (v/w) in bioink, UV crosslinking duration (4 s from 3 cm distance), and co-culture growth medium composition (50-50 % MADM-MSCM) were optimized for dermal and hypodermal layers. Furthermore, the fabrication of each skin layer as building blocks allowed studying the permeability of the skin layers to be evaluated separately. The effect of cell metabolism was included in the penetration assay.

Air-liquid interface opening of the chip provide continuous differentiation to the skin model. All layers protect their shape integrity and cell viability for more than 64 days. Dynamic culture showed no significant difference in cell viability in 4 days compared to static culture. Above 90% viability was obtained on chip experiments at 4 days. These data conclude that this skin-on-a-chip model can be cultured for many weeks and reflect similar morphology to the native skin.

Using different proportions of cells in the bioink better summarizes the difference between dermis and hypodermis. Dermal fibroblast cells were rich in the dermal

layer. Dermal layer was supported with adipose derived stem cells which have proven regulatory and proliferative effect on dermis layer. Wound healing process requires the stem cells therefore this model can be used in defining corrosive effect of chemicals. In most of the skin models, hypodermis is neglected due to its similar appearance. Hypodermis is similar to dermis and include stem cells in its structure. But hypodermis is mostly a fat deposit and made up of adipocytes. Differentiation and dedifferentiation processes are active on native human hypodermis and play an important role on regulating the metabolism of body. Adipose derived stem cells were differentiated for 14 days prior to encapsulation into the hypodermis layer. Together with undifferentiated stem cells, adipocyte rich hypodermis contains 1/3 of the dermal fibroblasts in this skin model.

In this skin model, epidermal thickening was observed on the outermost part of PLC scaffold proving keratinocyte differentiation. Addition of epidermis add barrier property to the model. In the absence of epidermis, skin-on-a-chip model showed shortened penetration time with higher drug penetration. Epidermis layer held the drug for an hour and released during the next hour. Cell uptake mechanisms are also similar to the native human skin.

The difference between static and dynamic cultures was compared to understand the effect of shear on the skin model. Dynamic culture resulted in near to zero shear and low toxicity. Therefore, this skin bioreactor design flow rate of 3.33 μL/min was found efficient for penetration studies, and it is also in between the flow rate that previously reported in the literature (between 3.28 μL/min and 20 μL/min).

In the literature, penetration models mostly focus on substances passing through membranes and often cell metabolism and drug cytotoxicity is neglected. Herein, next to the fluorometric assays, growth rate and cell viability of cocultures were determined in the penetration assaysand more accurate results achieved with a wider perspective.

Second part of the thesis, a GelMA-HAMA-Alginate bioink was developed. Pre- and post- crosslinking methods was combined with photocrosslinking and a IPN bioink was fabricated. Cross-linking conditions were changed, and resultant hydrogels were characterized for mechanical, rheology and viability. Polymer solution was 3D bioprinted with different cell types and different post-modifications were applied. Although the 3D printed hydrogel bioinks were made up of many carbohydrates and polymer nertworks, they retained their originally designed shape after printing and during culture periods. Room temperature printing condition acquires cells, optimum temperature and low cell cytotoxicity was achieved regardless of fabrication procedure of post modification. Optimized bioink was found a beneficial candidate for soft tissue bioprinting by testing with DF and ADSC cells. Post-modifications showed differences between cell morphologies. Increasing stiffness increased the coalesced cells rather than spreading, but such stifness did not alter cell viability. Addition of HAMA to the bioink may have contribute the use of this bioink on prevascularization studies.

This skin model can be a starting point for future skin models. The influence of nervous system components, intravascular circulation, melanocytes, and skin appendages must be included to produce a more biosimilar skin model. The skin model with superior biomimetic properties will eventually replace animal testing, and the accuracy of the drug selection will increase the process in the future.

REFERENCES

Abaci, H. E., Guo, Z., Doucet, Y., Jacków, J., & Christiano, A. (2017). Next generation human skin constructs as advanced tools for drug development. *Experimental Biology and Medicine*, *242*(17), 1657–1668. https://doi.org/10.1177/1535370217712690

Abd, E., Yousef, S. A., Pastore, M. N., Telaprolu, K., Mohammed, Y. H., Namjoshi, S., Grice, J. E., & Roberts, M. S. (2016). Skin models for the testing of transdermal drugs. *Clinical Pharmacology: Advances and Applications*, *8*, 163–176. https://doi.org/10.2147/CPAA.S64788

Aguado, B. A., Mulyasasmita, W., Su, J., Lampe, K. J., & Heilshorn, S. C. (2012). Improving viability of stem cells during syringe needle flow through the design of hydrogel cell carriers. *Tissue Engineering - Part A*, *18*(7–8), 806–815. https://doi.org/10.1089/ten.tea.2011.0391

Ali, N., Hosseini, M., Vainio, S., Taïeb, A., Cario-André, M., & Rezvani, H. R. (2015). Skin equivalents: Skin from reconstructions as models to study skin development and diseases. *British Journal of Dermatology*, *173*(2), 391–403. https://doi.org/10.1111/bjd.13886

Alonso, C., Collini, I., Carrer, V., Barba, C., Martí, M., & Coderch, L. (2020). Permeation kinetics of active drugs through lanolin-based artificial membranes. *Colloids and Surfaces B: Biointerfaces*, *192*(April), 111024. https://doi.org/10.1016/j.colsurfb.2020.111024

Alt, E., Yan, Y., Gehmert, S., Song, Y.-H., Altman, A., Gehmert, S., Vykoukal, D., & Bai, X. (2011). Fibroblasts share mesenchymal phenotypes with stem cells, but lack their differentiation and colony-forming potential. *Biology of the Cell*, *103*(4), 197–208. https://doi.org/10.1042/bc20100117

Aminabhavi, T. M., & Dharupaneedi, S. P. (2017). *12 - Production of chitosan-based hydrogels for biomedical applications* (J. A. Jennings & J. D. B. T.-C. B. B. V. 1 Bumgardner (eds.); pp. 295–319). Woodhead Publishing. https://doi.org/https://doi.org/10.1016/B978-0-08-100230-8.00012-1

Ashammakhi, N., Darabi, M. A., Çelebi-Saltik, B., Tutar, R., Hartel, M. C., Lee, J., Hussein, S. M., Goudie, M. J., Cornelius, M. B., Dokmeci, M. R., & Khademhosseini, A. (2020). Microphysiological Systems: Next Generation Systems for Assessing Toxicity and Therapeutic Effects of Nanomaterials. *Small Methods*, *4*(1), 1–19. https://doi.org/10.1002/smtd.201900589

Attalla, R., Puersten, E., Jain, N., & Selvaganapathy, P. R. (2019). 3D bioprinting of heterogeneous bi- and tri-layered hollow channels within gel scaffolds using scalable multi-axial microfluidic extrusion nozzle. *Biofabrication*, *11*(1), 015012. https://doi.org/10.1088/1758-5090/aaf7c7

Aydin, L., Kucuk, S., & Kenar, H. (2020). A universal self-eroding sacrificial bioink that enables bioprinting at room temperature. *Polymers for Advanced Technologies*, *31*(7), 1634–1647. https://doi.org/10.1002/pat.4892

Bellas, E., Seiberg, M., Garlick, J., & Kaplan, D. L. (2012). In vitro 3D Full-Thickness Skin-Equivalent Tissue Model Using Silk and Collagen Biomaterials. *Macromolecular Bioscience*, *12*(12), 1627–1636. https://doi.org/10.1002/mabi.201200262

Bencherif, S. A., Srinivasan, A., Horkay, F., Hollinger, J. O., Matyjaszewski, K., & Washburn, N. R. (2008). Influence of the degree of methacrylation on hyaluronic acid hydrogels properties. *Biomaterials*, *29*(12), 1739–1749. https://doi.org/10.1016/j.biomaterials.2007.11.047

Bernauer, U., Bodin, L., Chaudry, Q., Coenraads, P. J., Dusinska, M., Ezendam, J., Gaffet, E., Galli, C., Granum, B., Panderi, I., Rogiers, V., Rousselle, C., Stepnik, M., Vanhaecke, T., Wijnhoven, S., Koutsodimou, A., Simmonard, A., Uter, W., & Goetz, N. (2018). *"The SCCS note of Guidance for the testing*

of cosmetic ingredients and their safety evaluation – 10th Revision"SCCS/1602/18 - Final version.

Blaeser, A., Duarte Campos, D. F., Puster, U., Richtering, W., Stevens, M. M., & Fischer, H. (2016). Controlling Shear Stress in 3D Bioprinting is a Key Factor to Balance Printing Resolution and Stem Cell Integrity. *Advanced Healthcare Materials*, *5*(3), 326–333. https://doi.org/10.1002/adhm.201500677

Botham, P. A., Earl, L. K., Fentem, J. H., Roguet, R., & van de Sandt, J. J. M. (1998). Alternative Methods for Skin Irritation Testing: The Current Status: ECVAM Skin Irritation Task Force Report 1. *Alternatives to Laboratory Animals*, *26*(2), 195–211. https://doi.org/10.1177/026119299802600205

Braccini, I., & Pérez, S. (2001). Molecular Basis of Ca2+-Induced Gelation in Alginates and Pectins: The Egg-Box Model Revisited. *Biomacromolecules*, *2*(4), 1089–1096. https://doi.org/10.1021/bm010008g

Briganti, S., Camera, E., & Picardo, M. (2003). Chemical and instrumental approaches to treat hyperpigmentation. *Pigment Cell Research*, *16*(2), 101–110. https://doi.org/10.1034/j.1600-0749.2003.00029.x

Burdick, J. A., Chung, C., Jia, X., Randolph, M. A., & Langer, R. (2005). Controlled degradation and mechanical behavior of photopolymerized hyaluronic acid networks. *Biomacromolecules*, *6*(1), 386–391. https://doi.org/10.1021/bm049508a

Burgdorf, W. H. C. (2004). Fitzpatrick's dermatology in general medicine. 6th edition: Irwin M. Freedberg, MD, Arthur Z. Eisen, MD, Klauss Wolff, MD, K. Frank Austen, MD, Lowell A. Goldsmith, MD, and Stephen I. Katz, MD, PhD, editors, New York, 2003, McGraw-Hill. 2 volumes, 3328 pa. In *Journal of the American Academy of Dermatology* (Vol. 51, Issue 2). Elsevier. https://doi.org/10.1016/j.jaad.2003.12.039

Busatto, C., Labie, H., Lapeyre, V., Auzély-Velty, R., Casis, N., Estenoz, D., Ravaine, V., & Perro, A. (2016). Microfluidic-based preparation of hyaluronic

acid microgels for progesterone delivery. *COLAOB*.

Chandrasekharan, A., Seong, K. Y., Yim, S. G., Kim, S., Seo, S., Yoon, J., & Yang, S. Y. (2019). In situ photocrosslinkable hyaluronic acid-based surgical glue with tunable mechanical properties and high adhesive strength. *Journal of Polymer Science, Part A: Polymer Chemistry*, *57*, 522–530. https://doi.org/10.1002/pola.29290

Chen, Y. C., Lin, R. Z., Qi, H., Yang, Y., Bae, H., Melero-Martin, J. M., & Khademhosseini, A. (2012). Functional human vascular network generated in photocrosslinkable gelatin methacrylate hydrogels. *Advanced Functional Materials*, *22*(10), 2027–2039. https://doi.org/10.1002/adfm.201101662

Chopin-Doroteo, M., Mandujano-Tinoco, E. A., & Krötzsch, E. (2021). Tailoring of the rheological properties of bioinks to improve bioprinting and bioassembly for tissue replacement. *Biochimica et Biophysica Acta - General Subjects*, *1865*(2). https://doi.org/10.1016/j.bbagen.2020.129782

Coates, E. E., Riggin, C. N., & Fisher, J. P. (2013). Photocrosslinked alginate with hyaluronic acid hydrogels as vehicles for mesenchymal stem cell encapsulation and chondrogenesis. *Journal of Biomedical Materials Research - Part A*, *101 A*(7), 1962–1970. https://doi.org/10.1002/jbm.a.34499

Damen, M., Wirtz, L., Soroka, E., Khatif, H., Kukat, C., Simons, B. D., & Bazzi, H. (2021). High proliferation and delamination during skin epidermal stratification. *Nature Communications*, *12*(1), 1–16. https://doi.org/10.1038/s41467-021-23386-4

de Paula, F. J. A., Dick-de-Paula, I., Kawai, M., & Rosen, C. J. (2021). *Chapter 34 - Bone and fat* (D. W. Dempster, J. A. Cauley, M. L. Bouxsein, & F. B. T.-M. and F. O. (Fifth E. Cosman (eds.); pp. 833–846). Academic Press. https://doi.org/https://doi.org/10.1016/B978-0-12-813073-5.00034-4

Derr, K., Zou, J., Luo, K., Song, M. J., Sittampalam, G. S., Zhou, C., Michael, S., Ferrer, M., & Derr, P. (2019). Fully Three-Dimensional Bioprinted Skin

Equivalent Constructs with Validated Morphology and Barrier Function. *Tissue Engineering - Part C: Methods*, *25*(6), 334–343. https://doi.org/10.1089/ten.tec.2018.0318

Dikici, S., Claeyssens, F., & MacNeil, S. (2020). Bioengineering Vascular Networks to Study Angiogenesis and Vascularization of Physiologically Relevant Tissue Models in Vitro. *ACS Biomaterials Science and Engineering*, *6*(6), 3513–3528. https://doi.org/10.1021/acsbiomaterials.0c00191

Doke, S. K., & Dhawale, S. C. (2015). Alternatives to animal testing: A review. *Saudi Pharmaceutical Journal*, *23*(3), 223–229. https://doi.org/10.1016/j.jsps.2013.11.002

Duan, B., Kapetanovic, E., Hockaday, L. A., & Butcher, J. T. (2014). Three-dimensional printed trileaflet valve conduits using biological hydrogels and human valve interstitial cells. *Acta Biomaterialia*, *10*(5), 1836–1846. https://doi.org/https://doi.org/10.1016/j.actbio.2013.12.005

Duval, C., Chagnoleau, C., Pouradier, F., Sextius, P., Condom, E., & Bernerd, F. (2012). Human skin model containing melanocytes: Essential role of keratinocyte growth factor for constitutive pigmentation-functional response to α-melanocyte stimulating hormone and forskolin. *Tissue Engineering - Part C: Methods*, *18*(12), 947–957. https://doi.org/10.1089/ten.tec.2011.0676

Eibel, A., Fast, D. E., & Gescheidt, G. (2018). Choosing the ideal photoinitiator for free radical photopolymerizations: Predictions based on simulations using established data. *Polymer Chemistry*, *9*(41), 5107–5115. https://doi.org/10.1039/c8py01195h

Eke, G., Mangir, N., Hasirci, N., Macneil, S., & Hasirci, V. (2017). Development of a UV crosslinked biodegradable hydrogel containing adipose derived stem cells to promote vascularization for skin wounds and tissue engineering. *Biomaterials*, *129*, 188–198. https://doi.org/10.1016/j.biomaterials.2017.03.021

Eke, G., Mangir, N., Hasirci, N., MacNeil, S., & Hasirci, V. (2017). Development of a UV crosslinked biodegradable hydrogel containing adipose derived stem cells to promote vascularization for skin wounds and tissue engineering. *Biomaterials*, *129*, 188–198. https://doi.org/https://doi.org/10.1016/j.biomaterials.2017.03.021

El-Mohri, H., Wu, Y., Mohanty, S., & Ghosh, G. (2017). Impact of matrix stiffness on fibroblast function. *Materials Science and Engineering C*, *74*, 146–151. https://doi.org/10.1016/j.msec.2017.02.001

Ermis, M. (2020). Photo-crosslinked gelatin methacrylate hydrogels with mesenchymal stem cell and endothelial cell spheroids as soft tissue substitutes. *Journal of Materials Research*, *2017*, 1–15. https://doi.org/10.1557/jmr.2020.323

Escobar, C., Kao, C.-Y., Das, S., & Papoutsakis, E. T. (2020). Human megakaryocytic microparticles induce de novo platelet biogenesis in a wild-type murine model. *Blood Advances*, *4*(5), 804–814. https://doi.org/10.1182/bloodadvances.2019000753

Everett, J. S., & Sommers, M. S. (2013). Skin viscoelasticity: physiologic mechanisms, measurement issues, and application to nursing science. *Biological Research for Nursing*, *15*(3), 338–346. https://doi.org/10.1177/1099800411434151

Fajas, L. (2003). Adipogenesis: A cross-talk between cell proliferation and cell differentiation. *Annals of Medicine*, *35*(2), 79–85. https://doi.org/10.1080/07853890310009999

Feng, S., Mao, S., Zhang, Q., Li, W., & Lin, J. M. (2019). Online analysis of drug toxicity to cells with shear stress on an integrated microfluidic chip [Research-article]. *ACS Sensors*, *4*(2), 521–527. https://doi.org/10.1021/acssensors.8b01696

Fentem, J. H., Briggs, D., Chesné, C., Elliott, G. R., Harbell, J. W., Heylings, J. R.,

Portes, P., Roguet, R., van de Sandt, J. J. M., & Botham, P. A. (2001). A prevalidation study on in vitro tests for acute skin irritation: results and evaluation by the Management Team. *Toxicology in Vitro*, *15*(1), 57–93. https://doi.org/https://doi.org/10.1016/S0887-2333(01)00002-9

Frueh, F. S., Später, T., Körbel, C., Scheuer, C., Simson, A. C., Lindenblatt, N., Giovanoli, P., Menger, M. D., & Laschke, M. W. (2018). Prevascularization of dermal substitutes with adipose tissue-derived microvascular fragments enhances early skin grafting. *Scientific Reports*, *8*(1), 10977. https://doi.org/10.1038/s41598-018-29252-6

Fuertes, L., Santonja, C., Kutzner, H., & Requena, L. (2013). Immunohistochemistry in dermatopathology: a review of the most commonly used antibodies (part I). *Actas Dermo-Sifiliograficas*, *104*(2), 99–127. https://doi.org/10.1016/j.ad.2012.02.015

Gallagher, A. J., Ní Anniadh, A., Bruyere, K., Otténio, M., Xie, H., & Gilchrist, M. D. (2012). Dynamic tensile properties of human skin. *2012 IRCOBI Conference Proceedings - International Research Council on the Biomechanics of Injury*, 494–502.

Gao, T., Gillispie, G. J., Copus, J. S., Kumar, A. P. R., Seol, Y. J., Atala, A., Yoo, J. J., & Lee, S. J. (2018). Optimization of gelatin-alginate composite bioink printability using rheological parameters: A systematic approach. *Biofabrication*, *10*(3). https://doi.org/10.1088/1758-5090/aacdc7

Gao, T., Gillispie, G. J., Copus, J. S., Kumar, A., Rajan, P., Seol, Y., Atala, A., Yoo, J. J., & Lee, S. J. (2019). *Using Rheological Parameters : a Systematic Approach*. *10*(3), 1–17. https://doi.org/10.1088/1758-5090/aacdc7.Optimization

Gao, Y., & Jin, X. (2019). Dual crosslinked methacrylated alginate hydrogel micron fibers and tissue constructs for cell biology. *Marine Drugs*, *17*(10), 557. https://doi.org/10.3390/md17100557

García, J., Ríos, I., & Rico, F. F. (2019). Design and analyses of a transdermal drug delivery device (TD3). *Sensors (Switzerland)*, *19*(23). https://doi.org/10.3390/s19235090

Girard, P., Beraud, A., & Sirvent, A. (2000). Study of three complementary techniques for measuring cutaneous hydration in vivo in human subjects: NMR spectroscopy, transient thermal transfer and corneometry - application to xerotic skin and cosmetics. *Skin Research and Technology : Official Journal of International Society for Bioengineering and the Skin (ISBS) [and] International Society for Digital Imaging of Skin (ISDIS) [and] International Society for Skin Imaging (ISSI)*, *6*(4), 205–213. https://doi.org/10.1034/j.1600-0846.2000.006004205.x

Giuseppe, M. Di, Law, N., Webb, B., A. Macrae, R., Liew, L. J., Sercombe, T. B., Dilley, R. J., & Doyle, B. J. (2018). Mechanical behaviour of alginate-gelatin hydrogels for 3D bioprinting. *Journal of the Mechanical Behavior of Biomedical Materials*, *79*(December 2017), 150–157. https://doi.org/10.1016/j.jmbbm.2017.12.018

Groeber, F., Holeiter, M., Hampel, M., Hinderer, S., & Schenke-Layland, K. (2011). Skin tissue engineering - In vivo and in vitro applications. *Advanced Drug Delivery Reviews*, *63*(4), 352–366. https://doi.org/10.1016/j.addr.2011.01.005

Gwon, K., Kim, E., & Tae, G. (2017). Heparin-hyaluronic acid hydrogel in support of cellular activities of 3D encapsulated adipose derived stem cells. *Acta Biomaterialia*, *49*, 284–295. https://doi.org/10.1016/j.actbio.2016.12.001

Hafezi, F., Shorter, S., Tabriz, A. G., Hurt, A., Elmes, V., Boateng, J., & Douroumis, D. (2020). Bioprinting and preliminary testing of highly reproducible novel bioink for potential skin regeneration. *Pharmaceutics*, *12*(6), 1–21. https://doi.org/10.3390/pharmaceutics12060550

Hazur, J., Detsch, R., Karakaya, E., Kaschta, J., Teßmar, J., Schneidereit, D.,

Friedrich, O., Schubert, D. W., & Boccaccini, A. R. (2020). Improving alginate printability for biofabrication: establishment of a universal and homogeneous pre-crosslinking technique. *Biofabrication*, *12*(4). https://doi.org/10.1088/1758-5090/ab98e5

He, H., Li, D., Lin, Z., Peng, L., Yang, J., Wu, M., Cheng, D., Pan, H., & Ruan, C. (2020). Temperature-programmable and enzymatically solidifiable gelatin-based bioinks enable facile extrusion bioprinting. *Biofabrication*, *12*(4), 45003. https://doi.org/10.1088/1758-5090/ab9906

Herndon, D. N., Barrow, R. E., Rutan, R. L., Rutan, T. C., Desai, M. H., & Abston, S. (1989). A comparison of conservative versus early excision. Therapies in severely burned patients. *Annals of Surgery*, *209*(5), 547–553. https://doi.org/10.1097/00000658-198905000-00006

Hodivala, K. J., & Watt, F. M. (1994). Evidence that cadherins play a role in the downregulation of integrin expression that occurs during keratinocyte terminal differentiation. *Journal of Cell Biology*, *124*(4), 589–600. https://doi.org/10.1083/jcb.124.4.589

Hunter-Featherstone, E., Young, N., Chamberlain, K., Cubillas, P., Hulette, B., Wei, X., Tiesman, J. P., Bascom, C. C., Benham, A. M., Goldberg, M. W., Saretzki, G., & Karakesisoglou, I. (2021). Culturing Keratinocytes on Biomimetic Substrates Facilitates Improved Epidermal Assembly In Vitro. *Cells*, *10*(5), 1–19. https://doi.org/10.3390/cells10051177

Janžekoviĉ, Z. (1970). A new concept in the early excision and immediate grafting of burns. *Journal of Trauma - Injury, Infection and Critical Care*, *10*(12), 1103–1108. https://doi.org/10.1097/00005373-197012000-00001

Jorgensen, A. M., Varkey, M., Gorkun, A., Clouse, C., Xu, L., Chou, Z., Murphy, S. V., Molnar, J., Lee, S. J., Yoo, J. J., Soker, S., & Atala, A. (2020). Bioprinted Skin Recapitulates Normal Collagen Remodeling in Full-Thickness Wounds. *Tissue Engineering - Part A*, *26*(9–10), 512–526.

https://doi.org/10.1089/ten.tea.2019.0319

Jusoh, N., Ko, J., & Jeon, N. L. (2019). Microfluidics-based skin irritation test using in vitro 3D angiogenesis platform. *APL Bioengineering*, *3*(3). https://doi.org/10.1063/1.5093975

Kadri, R., Ben Messaoud, G., Tamayol, A., Aliakbarian, B., Zhang, H. Y., Hasan, M., Sánchez-González, L., & Arab-Tehrany, E. (2016). Preparation and characterization of nanofunctionalized alginate/methacrylated gelatin hybrid hydrogels. *RSC Advances*, *6*(33), 27879–27884. https://doi.org/10.1039/c6ra03699f

Kalra, A., & Lowe, A. (2016). Mechanical Behaviour of Skin: A Review. *Journal of Material Science & Engineering*, *5*. https://doi.org/10.4172/2169-0022.1000254

Kapałczyńska, M., Kolenda, T., Przybyła, W., Zajączkowska, M., Teresiak, A., Filas, V., Ibbs, M., Bliźniak, R., Łuczewski, Ł., & Lamperska, K. (2018). 2D and 3D cell cultures - a comparison of different types of cancer cell cultures. *Archives of Medical Science : AMS*, *14*(4), 910–919. https://doi.org/10.5114/aoms.2016.63743

Khoshfetrat, A. B., Kino-oka, M., Takezawa, Y., Yamamoto, T., Sugawara, K., & Taya, M. (2009). *Seeding Density Modulates Migration and Morphology of Rabbit Chondrocytes Cultured in Collagen Gels*. *102*(1), 294–302. https://doi.org/10.1002/bit.22029

Kilic Bektas, C., & Hasirci, V. (2019). Cell Loaded GelMA:HEMA IPN hydrogels for corneal stroma engineering. *Journal of Materials Science: Materials in Medicine*, *31*(1), 2. https://doi.org/10.1007/s10856-019-6345-4

Kim, W. S., Park, B. S., Sung, J. H., Yang, J. M., Park, S. B., Kwak, S. J., & Park, J. S. (2007). Wound healing effect of adipose-derived stem cells: A critical role of secretory factors on human dermal fibroblasts. *Journal of Dermatological Science*, *48*(1), 15–24.

https://doi.org/10.1016/j.jdermsci.2007.05.018

Klar, A. S., Güven, S., Biedermann, T., Luginbühl, J., Böttcher-Haberzeth, S., Meuli-Simmen, C., Meuli, M., Martin, I., Scherberich, A., & Reichmann, E. (2014). Tissue-engineered dermo-epidermal skin grafts prevascularized with adipose-derived cells. *Biomaterials*, *35*(19), 5065–5078. https://doi.org/10.1016/j.biomaterials.2014.02.049

Klenerman, L. (2015). Human Anatomy. In *Human Anatomy*. https://doi.org/10.1093/actrade/9780198707370.001.0001

Kolarsick, P. A. J., Kolarsick, M. A., & Goodwin, C. (2011). Anatomy and Physiology of the Skin. *Journal of the Dermatology Nurses' Association*, *3*(4), 203–213. https://doi.org/10.1097/jdn.0b013e3182274a98

Kong, J., & Yu, S. (2007). Fourier transform infrared spectroscopic analysis of protein secondary structures. *Acta Biochimica et Biophysica Sinica*, *39*(8), 549–559. https://doi.org/10.1111/j.1745-7270.2007.00320.x

Koria, P., & Andreadis, S. T. (2006). Epidermal morphogenesis: The transcriptional program of human keratinocytes during stratification. *Journal of Investigative Dermatology*, *126*(8), 1834–1841. https://doi.org/10.1038/sj.jid.5700325

Kuss, M., Kim, J., Qi, D., Wu, S., Lei, Y., Chung, S., & Duan, B. (2018). Effects of tunable, 3D-bioprinted hydrogels on human brown adipocyte behavior and metabolic function. *Acta Biomaterialia*, *71*, 486–495. https://doi.org/10.1016/j.actbio.2018.03.021

Langer, R., & Vacanti, J. P. (1993). Tissue engineering. *Science*. https://doi.org/10.1126/science.8493529

Lechler, T., & Fuchs, E. (2005). Asymmetric cell divisions promote stratification and differentiation of mammalian skin. *Nature*, *437*(7056), 275–280. https://doi.org/10.1038/nature03922

Lee, S., Jin, S. P., Kim, Y. K., Sung, G. Y., Chung, J. H., & Sung, J. H. (2017). Construction of 3D multicellular microfluidic chip for an in vitro skin model. *Biomedical Microdevices*, *19*(2). https://doi.org/10.1007/s10544-017-0156-5

Levett, P. A., Hutmacher, D. W., Malda, J., & Klein, T. J. (2014). Hyaluronic acid enhances the mechanical properties of tissue-engineered cartilage constructs. *PLoS ONE*, *9*(12). https://doi.org/10.1371/journal.pone.0113216

Lewis, J. E., Jensen, P. J., & Wheelock, M. J. (1994). *Cadherin Function Is Required for Human Keratinocytes to Assemble Desmosomes and Stratify in Response to Calcium*. 870–877. https://doi.org/10.1111/1523-1747.ep12382690

Li, X., Chen, S., Li, J., Wang, X., Zhang, J., Kawazoe, N., & Chen, G. (2016). 3D culture of chondrocytes in gelatin hydrogels with different stiffness. *Polymers*, *8*(8). https://doi.org/10.3390/polym8080269

Li, X., Zhang, J., Kawazoe, N., & Chen, G. (2017). Fabrication of highly crosslinked gelatin hydrogel and its influence on chondrocyte proliferation and phenotype. *Polymers*, *9*(8). https://doi.org/10.3390/polym9080309

Li, Z., Huang, S., & Fu, X. (2018). 3D bioprinting skin. *3D Bioprinting for Reconstructive Surgery: Techniques and Applications*, 367–376. https://doi.org/10.1016/B978-0-08-101103-4.00017-X

Lin, C. S., Xin, Z. C., Dai, J., & Lue, T. F. (2013). Commonly used mesenchymal stem cell markers and tracking labels: Limitations and challenges. *Histology and Histopathology*, *28*(9), 1109–1116. https://doi.org/10.14670/HH-28.1109

Lin, R. Z., Chen, Y. C., Moreno-Luna, R., Khademhosseini, A., & Melero-Martin, J. M. (2013). Transdermal regulation of vascular network bioengineering using aphotopolymerizable methacrylated gelatin hydrogel. *Biomaterials*, *34*(28), 6785–6796. https://doi.org/10.1016/j.biomaterials.2013.05.060

Lorthois, I., Simard, M., Morin, S., & Pouliot, R. (2019). Infiltration of T cells into

a three-dimensional psoriatic skin model mimics pathological key features. *International Journal of Molecular Sciences*, *20*(7). https://doi.org/10.3390/ijms20071670

MacNeil, S. (2007). Progress and opportunities for tissue-engineered skin. *Nature*, *445*(7130), 874–880. https://doi.org/10.1038/nature05664

Malda, J., Visser, J., Melchels, F. P., Jüngst, T., Hennink, W. E., Dhert, W. J. A., Groll, J., & Hutmacher, D. W. (2013). 25th anniversary article: Engineering hydrogels for biofabrication. *Advanced Materials (Deerfield Beach, Fla.)*, *25*(36), 5011–5028. https://doi.org/10.1002/adma.201302042

Marcon, B. H., Shigunov, P., Spangenberg, L., Pereira, I. T., de Aguiar, A. M., Amorín, R., Rebelatto, C. K., Correa, A., & Dallagiovanna, B. (2019). Cell cycle genes are downregulated after adipogenic triggering in human adipose tissue-derived stem cells by regulation of mRNA abundance. *Scientific Reports*, *9*(1), 1–10. https://doi.org/10.1038/s41598-019-42005-3

Marieb, E. N., & Hoehn, K. (2010). *Essentials of human anatomy & physiology* (9th ed.). Pearson Education. https://search.library.wisc.edu/catalog/9910059601802121

Marquez, M. P., Alencastro, F., Madrigal, A., Jimenez, J. L., Blanco, G., Gureghian, A., Keagy, L., Lee, C., Liu, R., Tan, L., Deignan, K., Armstrong, B., & Zhao, Y. (2017). The Role of Cellular Proliferation in Adipogenic Differentiation of Human Adipose Tissue-Derived Mesenchymal Stem Cells. *Stem Cells and Development*, *26*(21), 1578–1595. https://doi.org/10.1089/scd.2017.0071

Martineau, L., Peng, H., & Pang, S. (2005). Development of a novel biomaterial: Part II. Evaluation of a photo cross-linking method. *Defence R&D Canada - Toronto Technical Report, December*, 11–42.

McCormack, A., Highley, C. B., Leslie, N. R., & Melchels, F. P. W. (2020). 3D Printing in Suspension Baths: Keeping the Promises of Bioprinting Afloat.

Trends in Biotechnology, *38*(6), 584–593. https://doi.org/10.1016/j.tibtech.2019.12.020

McKay, I. A., & Leigh, I. M. (1995). Altered keratinocyte growth and differentiation in psoriasis. *Clinics in Dermatology*, *13*(2), 105–114. https://doi.org/https://doi.org/10.1016/0738-081X(95)93817-8

Mehendale, S. V, Mellor, L. F., Taylor, M. A., Loboa, E. G., & Shirwaiker, R. A. (2017). Effects of 3D-bioplotted polycaprolactone scaffold geometry on human adipose-derived stem cell viability and proliferation. *Rapid Prototyping Journal*, *23*(3), 534–542. https://doi.org/10.1108/RPJ-03-2016-0035

Messager, L., Portecop, N., Hachet, E., Lapeyre, V., Pignot-Paintrand, I., Catargi, B., Auzély-Velty, R., & Ravaine, V. (2013). Photochemical crosslinking of hyaluronic acid confined in nanoemulsions: Towards nanogels with a controlled structure. *Journal of Materials Chemistry B*, *1*(27), 3369–3379. https://doi.org/10.1039/c3tb20300j

Miyazaki, H., Tsunoi, Y., Akagi, T., Sato, S., Akashi, M., & Saitoh, D. (2019). A novel strategy to engineer pre-vascularized 3-dimensional skin substitutes to achieve efficient, functional engraftment. *Scientific Reports*, *9*(1), 1–3. https://doi.org/10.1038/s41598-019-44113-6

Modaresifar, K., Hadjizadeh, A., & Niknejad, H. (2018). Design and fabrication of GelMA/chitosan nanoparticles composite hydrogel for angiogenic growth factor delivery. *Artificial Cells, Nanomedicine, and Biotechnology*, *46*(8), 1799–1808. https://doi.org/10.1080/21691401.2017.1392970

Mohammadi, M. H., Araghi, B. H., Beydaghi, V., Geraili, A., Moradi, F., Jafari, P., Janmaleki, M., & Valente, K. P. (2016). *Skin Diseases Modeling using Combined Tissue Engineering and Microfl uidic Technologies*. 2459–2480. https://doi.org/10.1002/adhm.201600439

Möller, L., Krause, A., Dahlmann, J., Gruh, I., Kirschning, A., & Dräger, G.

(2011). Preparation and evaluation of hydrogel-composites from methacrylated hyaluronic acid, alginate, and gelatin for tissue engineering. *International Journal of Artificial Organs*, *34*(2), 93–102. https://doi.org/10.5301/IJAO.2011.6397

Mondrinos, M. J., Dembzynski, R., Lu, L., Byrapogu, V. K. C., Wootton, D. M., Lelkes, P. I., & Zhou, J. (2006). Porogen-based solid freeform fabrication of polycaprolactone-calcium phosphate scaffolds for tissue engineering. *Biomaterials*, *27*(25), 4399–4408. https://doi.org/10.1016/j.biomaterials.2006.03.049

Monteiro, N., Thrivikraman, G., Athirasala, A., Tahayeri, A., França, C. M., Ferracane, J. L., & Bertassoni, L. E. (2018). Photopolymerization of cell-laden gelatin methacryloyl hydrogels using a dental curing light for regenerative dentistry. *Dental Materials*, *34*(3), 389–399. https://doi.org/10.1016/j.dental.2017.11.020

Murphy, S. V., & Atala, A. (2014a). 3D bioprinting of tissues and organs. *Nature Biotechnology*, *32*(8), 773–785. https://doi.org/10.1038/nbt.2958

Murphy, S. V, & Atala, A. (2014b). 3D bioprinting of tissues and organs. *Nature Biotechnology*, *32*(8), 773–785. https://doi.org/10.1038/nbt.2958

Nakagawa, Y., & Ebara, M. (2020). Polysaccharides for Drug Delivery: The Development of Polysaccharide-Based Materials and Glycopolymer to Improve Drug Delivery Applications. In *Reference Module in Chemistry, Molecular Sciences and Chemical Engineering*. https://doi.org/10.1016/B978-0-12-819475-1.00024-9

Nassiri, F., Cusimano, M. D., Scheithauer, B. W., Rotondo, F., Fazio, A., Yousef, G. M., Syro, L. V, Kovacs, K., & Lloyd, R. V. (2011). Endoglin (CD105): a review of its role in angiogenesis and tumor diagnosis, progression and therapy. *Anticancer Research*, *31*(6), 2283–2290.

Navarro, M., Ruberte, J., & Carretero, A. (2017). Common integument. In

Morphological Mouse Phenotyping: Anatomy, Histology and Imaging (1st ed.). Elsevier Ltd. https://doi.org/10.1016/B978-0-12-812972-2.50016-7

Neil, J. E., Brown, M. B., & Williams, A. C. (2020). Human skin explant model for the investigation of topical therapeutics. *Scientific Reports*, *10*(1), 1–8. https://doi.org/10.1038/s41598-020-78292-4

Ng, W. L., & Yeong, W. Y. (2019). The future of skin toxicology testing - Three-dimensional bioprinting meets microfluidics. *International Journal of Bioprinting*, *5*(2.1 Special Issue), 44–54. https://doi.org/10.18063/ijb.v5i2.1.237

Ní Annaidh, A., Bruyère, K., Destrade, M., Gilchrist, M. D., & Otténio, M. (2012). Characterization of the anisotropic mechanical properties of excised human skin. *Journal of the Mechanical Behavior of Biomedical Materials*, *5*(1), 139–148. https://doi.org/10.1016/j.jmbbm.2011.08.016

Nichol, J.W., & Khademhosseini, A. (2010). Modular tissue engineering: Engineering biological tissues from the bottom up. *Soft Matters*, *5*(7), 1312–1319. https://doi.org/10.1039/b814285h.Modular

Nichol, Jason W., Koshy, S. T., Bae, H., Hwang, C. M., Yamanlar, S., & Khademhosseini, A. (2010). Cell-laden microengineered gelatin methacrylate hydrogels. *Biomaterials*, *31*(21), 5536–5544. https://doi.org/10.1016/j.biomaterials.2010.03.064

Nichol, Jason W, Koshy, S. T., Bae, H., Hwang, C. M., Yamanlar, S., & Khademhosseini, A. (2010). Cell-laden microengineered gelatin methacrylate hydrogels. *Biomaterials*, *31*(21), 5536–5544. https://doi.org/https://doi.org/10.1016/j.biomaterials.2010.03.064

Noshadi, I., Hong, S., Sullivan, K. E., Shirzaei Sani, E., Portillo-Lara, R., Tamayol, A., Shin, S. R., Gao, A. E., Stoppel, W. L., Black, L. D., Khademhosseini, A., & Annabi, N. (2017). In vitro and in vivo analysis of visible light crosslinkable gelatin methacryloyl (GelMA) hydrogels. *Biomaterials Science*,

5(10), 2093–2105. https://doi.org/10.1039/c7bm00110j

Nossol, C., Diesing, A. K., Walk, N., Faber-Zuschratter, H., Hartig, R., Post, A., Kluess, J., Rothkötter, H. J., & Kahlert, S. (2011). Air-liquid interface cultures enhance the oxygen supply and trigger the structural and functional differentiation of intestinal porcine epithelial cells (IPEC). *Histochemistry and Cell Biology*, *136*(1), 103–115. https://doi.org/10.1007/s00418-011-0826-y

OECD. (2013). Test No. 439: In Vitro Skin Irritation - Reconstructed Human Epidermis Test Method. In *Test No. 439: In Vitro Skin Irritation - Reconstructed Human Epidermis Test Method*. OECD. https://doi.org/10.1787/9789264203884-en

Oliveira, H., Médina, C., Stachowicz, M. L., Paiva dos Santos, B., Chagot, L., Dusserre, N., & Fricain, J. C. (2021). Extracellular matrix (ECM)-derived bioinks designed to foster vasculogenesis and neurite outgrowth: Characterization and bioprinting. *Bioprinting*, *22*(October 2020). https://doi.org/10.1016/j.bprint.2021.e00134

Olzmann, J. A., & Carvalho, P. (2019). Dynamics and functions of lipid droplets. *Nature Reviews Molecular Cell Biology*, *20*(3), 137–155. https://doi.org/10.1038/s41580-018-0085-z

Oualla-bachiri, W., Fernández-gonzález, A., Quiñones-vico, M. I., & Arias-santiago, S. (2020). From grafts to human bioengineered vascularized skin substitutes. *International Journal of Molecular Sciences*, *21*(21), 1–27. https://doi.org/10.3390/ijms21218197

Oudshoorn, M. H. M., Rissmann, R., Bouwstra, J. A., & Hennink, W. E. (2007). Synthesis of methacrylated hyaluronic acid with tailored degree of substitution. *Polymer*, *48*(7), 1915–1920. https://doi.org/10.1016/j.polymer.2007.01.068

Pawar, S. N., & Edgar, K. J. (2012). Alginate derivatization: A review of chemistry, properties and applications. *Biomaterials*, *33*(11), 3279–3305.

https://doi.org/10.1016/j.biomaterials.2012.01.007

Pelham, R. J., & Wang, Y. (1997). Cell locomotion and focal adhesions are regulated by substrate flexibility. *Proceedings of the National Academy of Sciences*, *94*(25), 13661 LP – 13665. https://doi.org/10.1073/pnas.94.25.13661

Pereira, B. P., Lucas, P. W., & Swee-Hin, T. (1997). Ranking the fracture toughness of thin mammalian soft tissues using the scissors cutting test. *Journal of Biomechanics*, *30*(1), 91–94. https://doi.org/https://doi.org/10.1016/S0021-9290(96)00101-7

Perez-Valle, A., Del Amo, C., & Andia, I. (2020). Overview of Current Advances in Extrusion Bioprinting for Skin Applications. In *International Journal of Molecular Sciences* (Vol. 21, Issue 18). https://doi.org/10.3390/ijms21186679

Petta, D., Petta, D., D'Amora, U., Ambrosio, L., Grijpma, D. W., Eglin, D., Eglin, D., & D'Este, M. (2020). Hyaluronic acid as a bioink for extrusion-based 3D printing. *Biofabrication*, *12*(3). https://doi.org/10.1088/1758-5090/ab8752

Poldervaart, M. T., Goversen, B., De Ruijter, M., Abbadessa, A., Melchels, F. P. W., Öner, F. C., Dhert, W. J. A., Vermonden, T., & Alblas, J. (2017). 3D bioprinting of methacrylated hyaluronic acid (MeHA) hydrogel with intrinsic osteogenicity. *PLoS ONE*, *12*(6), 1–15. https://doi.org/10.1371/journal.pone.0177628

Ponec, M. (1984). Effects of Glucocorticoids on Cultured Skin Fibroblasts and Keratinocytes. *International Journal of Dermatology*, *23*(1), 11–24. https://doi.org/10.1111/j.1365-4362.1984.tb05657.x

Ponmozhi, J., Dhinakaran, S., Varga-medveczky, Z., Fónagy, K., Bors, L. A., Iván, K., & Erdő, F. (2021). Development of skin-on-a-chip platforms for different utilizations: Factors to be considered. *Micromachines*, *12*(3), 1–25. https://doi.org/10.3390/mi12030294

Potter, C. M. F., Lao, K. H., Zeng, L., & Xu, Q. (2014). Role of biomechanical forces in stem cell vascular lineage differentiation. *Arteriosclerosis, Thrombosis, and Vascular Biology*, *34*(10), 2184–2190. https://doi.org/10.1161/ATVBAHA.114.303423

Quinby, W. C. J., Burke, J. F., & Bondoc, C. C. (1981). Primary excision and immediate wound closure. *Intensive Care Medicine*, *7*(2), 71–76. https://doi.org/10.1007/bf01687263

Rahali, K., Ben Messaoud, G., Kahn, C. J. F., Sanchez-Gonzalez, L., Kaci, M., Cleymand, F., Fleutot, S., Linder, M., Desobry, S., & Arab-Tehrany, E. (2017). Synthesis and characterization of nanofunctionalized gelatin methacrylate hydrogels. *International Journal of Molecular Sciences*, *18*(12). https://doi.org/10.3390/ijms18122675

Ramadan, Q., Chia, F., & Ting, W. (2016). Lab on a Chip. *Lab on a Chip*, *16*, 1899–1908. https://doi.org/10.1039/C6LC00229C

Randall, M. J., Jüngel, A., Rimann, M., & Wuertz-Kozak, K. (2018). Advances in the biofabrication of 3D skin in vitro: Healthy and pathological models. *Frontiers in Bioengineering and Biotechnology*, *6*(OCT). https://doi.org/10.3389/fbioe.2018.00154

Rapalli, V. K., & Singhvi, G. (2021). Dermato-pharmacokinetic: assessment tools for topically applied dosage forms. *Expert Opinion on Drug Delivery*, *18*(4), 423–426. https://doi.org/10.1080/17425247.2021.1856071

Reverdin, J. L., & IVY, R. H. (1968). The classic reprint greffe epidermique—experıence faite dans le service de m. Le docteur guyon, a l'hôpital necker. *Plastic and Reconstructive Surgery*, *41*(1). https://journals.lww.com/plasreconsurg/Fulltext/1968/01000/THE_CLASSIC_REPRINT_GREFFE_EPIDERMIQUE_EXPERIENCE.14.aspx

Rossi, J. (2016). Research: Animals. In *Encyclopedia of Global Bioethics* (pp. 2436–2448). https://doi.org/10.1007/978-3-319-09483-0_373

Rübsam, M., Mertz, A. F., Kubo, A., Marg, S., Jüngst, C., Goranci-Buzhala, G., Schauss, A. C., Horsley, V., Dufresne, E. R., Moser, M., Ziegler, W., Amagai, M., Wickström, S. A., & Niessen, C. M. (2017). E-cadherin integrates mechanotransduction and EGFR signaling to control junctional tissue polarization and tight junction positioning. *Nature Communications*, *8*(1), 1–15. https://doi.org/10.1038/s41467-017-01170-7

Ruffner, H., Graf-Hausner, U., & Mathes, S. (2016). Skin Models for Drug Development and Biopharmaceutical Industry. In *Skin Tissue Engineering and Regenerative Medicine*. Elsevier Inc. https://doi.org/10.1016/B978-0-12-801654-1.00018-8

Russo, B., Brembilla, N. C., & Chizzolini, C. (2020). Interplay between keratinocytes and fibroblasts: A systematic review providing a new angle for understanding skin fibrotic disorders. In *Frontiers in Immunology* (Vol. 11, p. 648). https://doi.org/10.3389/fimmu.2020.00648

Saarai, A., Kasparkova, V., Sedlacek, T., & Saha, P. (2011). A comparative study of crosslinked sodium alginate/gelatin hydrogels for wound dressing. *Recent Researches in Geography, Geology, Energy, Environment and Biomedicine - Proc. of the 4th WSEAS Int. Conf. on EMESEG'11, 2nd Int. Conf. on WORLD-GEO'11, 5th Int. Conf. on EDEB'11*, 384–389.

Sarkiri, M., Fox, S. C., Fratila-Apachitei, L. E., & Zadpoor, A. A. (2019). Bioengineered skin intended for skin disease modeling. *International Journal of Molecular Sciences*, *20*(6), 1407. https://doi.org/10.3390/ijms20061407

Schmidt, F. F., Nowakowski, S., & Kluger, P. J. (2020). Improvement of a Three-Layered in vitro Skin Model for Topical Application of Irritating Substances. *Frontiers in Bioengineering and Biotechnology*, *8*(May), 1–11. https://doi.org/10.3389/fbioe.2020.00388

Schmook, F. P., Meingassner, J. G., & Billich, A. (2001). Comparison of human skin or epidermis models with human and animal skin in in-vitro percutaneous

absorption. *International Journal of Pharmaceutics*, *215*(1), 51–56. https://doi.org/https://doi.org/10.1016/S0378-5173(00)00665-7

Schuurmans, C. C. L., Mihajlovic, M., Hiemstra, C., Ito, K., Hennink, W. E., & Vermonden, T. (2021). Hyaluronic acid and chondroitin sulfate (meth)acrylate-based hydrogels for tissue engineering: Synthesis, characteristics and pre-clinical evaluation. *Biomaterials*, *268*(December 2020), 120602. https://doi.org/10.1016/j.biomaterials.2020.120602

Şeker, Ş., Elçin, A. E., Yumak, T., Sinağ, A., & Elçin, Y. M. (2014). In vitro cytotoxicity of hydrothermally synthesized ZnO nanoparticles on human periodontal ligament fibroblast and mouse dermal fibroblast cells. *Toxicology in Vitro*, *28*(8), 1349–1358. https://doi.org/10.1016/j.tiv.2014.06.016

Sell, S. A., Wolfe, P. S., Garg, K., McCool, J. M., Rodriguez, I. A., & Bowlin, G. L. (2010). The use of natural polymers in tissue engineering: A focus on electrospun extracellular matrix analogues. *Polymers*, *2*(4), 522–553. https://doi.org/10.3390/polym2040522

Shirahama, H., Lee, B. H., Tan, L. P., & Cho, N. J. (2016). Precise tuning of facile one-pot gelatin methacryloyl (GelMA) synthesis. *Scientific Reports*, *6*(May), 1–11. https://doi.org/10.1038/srep31036

Skardal, A., Zhang, J., McCoard, L., Xu, X., Oottamasathien, S., & Prestwich, G. D. (2010). Photocrosslinkable hyaluronan-gelatin hydrogels for two-step bioprinting. *Tissue Engineering - Part A*, *16*(8), 2675–2685. https://doi.org/10.1089/ten.tea.2009.0798

Somuncu, Ö. S., Karahan, C., Somuncu, S., & Şahin, F. (2018). Tissue Engineering for Skin Replacement Methods. In R. Sharma (Ed.), *Stem Cells in Clinical Practice and Tissue Engineering* (May 2nd 18, pp. 315–333). IntechOpen. https://doi.org/10.5772/intechopen.69905

Strålfors, P. (1990). Autolysis of isolated adipocytes by endogenously produced fatty acids. *FEBS Letters*, *263*(1), 153–154.

https://doi.org/https://doi.org/10.1016/0014-5793(90)80726-Y

Suhail, S., Sardashti, N., Jaiswal, D., Rudraiah, S., Misra, M., & Kumbar, S. G. (2019). Engineered Skin Tissue Equivalents for Product Evaluation and Therapeutic Applications. *Biotechnology Journal*, *14*(7). https://doi.org/10.1002/biot.201900022

Sun, M., Sun, X., Wang, Z., Guo, S., Yu, G., & Yang, H. (2018). Synthesis and Properties of Gelatin Methacryloyl (GelMA) Hydrogels and Their Recent Applications in Load-Bearing Tissue. *Polymers*, *10*(11). https://doi.org/10.3390/polym10111290

Sun, Y., Chen, C. S., & Fu, J. (2012). Forcing stem cells to behave: A biophysical perspective of the cellular microenvironment. *Annual Review of Biophysics*, *41*(1), 519–542. https://doi.org/10.1146/annurev-biophys-042910-155306

Sutterby, E., Thurgood, P., Baratchi, S., Khoshmanesh, K., & Pirogova, E. (2020). Microfluidic Skin-on-a-Chip Models: Toward Biomimetic Artificial Skin. *Small*, *16*(39), 1–17. https://doi.org/10.1002/smll.202002515

Szymański, Ł., Jęderka, K., Cios, A., Ciepelak, M., Lewicka, A., Stankiewicz, W., & Lewicki, S. (2020). A simple method for the production of human skin equivalent in 3D, multi-cell culture. *International Journal of Molecular Sciences*, *21*(13), 1–11. https://doi.org/10.3390/ijms21134644

Tabriz, A. G., Hermida, M. A., Leslie, N. R., & Shu, W. (2015). Three-dimensional bioprinting of complex cell laden alginate hydrogel structures. *Biofabrication*, *7*(4). https://doi.org/10.1088/1758-5090/7/4/045012

Tamayol, A., Najafabadi, A. H., Aliakbarian, B., Arab-Tehrany, E., Akbari, M., Annabi, N., Juncker, D., & Khademhosseini, A. (2015). Hydrogel Templates for Rapid Manufacturing of Bioactive Fibers and 3D Constructs. *Advanced Healthcare Materials*, *4*(14), 2146–2153. https://doi.org/10.1002/adhm.201500492

Tan, Y. J., Leong, K. F., An, J., Chian, K. S., Tan, X., & Yeong, W. Y. (2015). Fabrication and in vitro analysis of tubular scaffolds by melt-drawing for esophageal tissue engineering. *Materials Letters*, *159*, 424–427. https://doi.org/10.1016/j.matlet.2015.07.061

Tan, Y. J., Yeong, W. Y., Tan, X., An, J., Chian, K. S., & Leong, K. F. (2016). Characterization, mechanical behavior and in vitro evaluation of a melt-drawn scaffold for esophageal tissue engineering. *Journal of the Mechanical Behavior of Biomedical Materials*, *57*, 246–259. https://doi.org/10.1016/j.jmbbm.2015.12.015

Tarassoli, S. P., Jessop, Z. M., Al-sabah, A., Gao, N., Whitaker, S., Doak, S., & Whitaker, I. S. (2018). Skin tissue engineering using 3D bioprinting : An evolving research field. *Journal of Plastic, Reconstructive & Aesthetic Surgery*, *71*(5), 615–623. https://doi.org/10.1016/j.bjps.2017.12.006

Thankam, F. G., & Muthu, J. (2014). Influence of physical and mechanical properties of amphiphilic biosynthetic hydrogels on long-term cell viability. *Journal of the Mechanical Behavior of Biomedical Materials*, *35*, 111–122. https://doi.org/https://doi.org/10.1016/j.jmbbm.2014.03.010

Thotakura, N., Kumar, P., Wadhwa, S., Raza, K., & Katare, P. (2017). Dermatokinetics as an Important Tool to Assess the Bioavailability of Drugs by Topical Nanocarriers. *Current Drug Metabolism*, *18*(5), 404–411. https://doi.org/10.2174/1389200218666170306104042

Tinkle, C. L., Lechler, T., Pasolli, H. A., & Fuchs, E. (2004). Conditional targeting of E-cadherin in skin: Insights into hyperproliferative and degenerative responses. *Proceedings of the National Academy of Sciences of the United States of America*, *101*(2), 552–557. https://doi.org/10.1073/pnas.0307437100

Tracy, L. E., Minasian, R. A., & Caterson, E. J. (2016). Extracellular Matrix and Dermal Fibroblast Function in the Healing Wound. *Advances in Wound Care*, *5*(3), 119–136. https://doi.org/10.1089/wound.2014.0561

Trompezinski, S., Berthier-Vergnes, O., Denis, A., Schmitt, D., & Viac, J. (2004). Comparative expression of vascular endothelial growth factor family members, VEGF-B, -C and -D, by normal human keratinocytes and fibroblasts. *Experimental Dermatology*, *13*(2), 98–105. https://doi.org/https://doi.org/10.1111/j.0906-6705.2004.00137.x

Trudel, J., & Massia, S. P. (2002). Assessment of the cytotoxicity of photocrosslinked dextran and hyaluronan-based hydrogels to vascular smooth muscle cells. *Biomaterials*, *23*(16), 3299–3307. https://doi.org/10.1016/s0142-9612(02)00009-1

Valencia, L., Canalejas-Tejero, V., Clemente, M., Fernaud, I., Holgado, M., Jorcano, J. L., & Velasco, D. (2021). A new microfluidic method enabling the generation of multi-layered tissues-on-chips using skin cells as a proof of concept. *Scientific Reports*, *11*(1), 1–14. https://doi.org/10.1038/s41598-021-91875-z

Van Den Bulcke, A. I., Bogdanov, B., De Rooze, N., Schacht, E. H., Cornelissen, M., & Berghmans, H. (2000). Structural and rheological properties of methacrylamide modified gelatin hydrogels. *Biomacromolecules*, *1*(1), 31–38. https://doi.org/10.1021/bm990017d

Velasco, D., Quílez, C., Garcia, M., del Cañizo, J. F., & Jorcano, J. L. (2018). 3D human skin bioprinting: a view from the bio side. *Journal of 3D Printing in Medicine*, *2*(3), 141–162. https://doi.org/10.2217/3dp-2018-0008

Venugopal, B., Mogha, P., Dhawan, J., & Majumder, A. (2018). Cell density overrides the effect of substrate stiffness on human mesenchymal stem cells' morphology and proliferation. *Biomaterials Science*, *6*(5), 1109–1119. https://doi.org/10.1039/c7bm00853h

Vidal, S. E. L., Tamamoto, K. A., Nguyen, H., Abbott, R. D., Cairns, D. M., & Kaplan, D. L. (2019). 3D biomaterial matrix to support long term, full thickness, immuno-competent human skin equivalents with nervous system

components. *Biomaterials*, *198*, 194–203. https://doi.org/https://doi.org/10.1016/j.biomaterials.2018.04.044

Vijayavenkataraman, S., Lu, W. F., & Fuh, J. Y. H. (2016). 3D bioprinting of skin: a state-of-the-art review on modelling, materials, and processes. *Biofabrication*, *8*(3), 032001. https://doi.org/10.1088/1758-5090/8/3/032001

Walejewska, E., Idaszek, J., Heljak, M., Chlanda, A., Choinska, E., Hasirci, V., & Swieszkowski, W. (2020). The effect of introduction of filament shift on degradation behaviour of PLGA- and PLCL-based scaffolds fabricated via additive manufacturing. *Polymer Degradation and Stability*, *171*, 109030. https://doi.org/10.1016/j.polymdegradstab.2019.109030

Wilkens, C. A., Rivet, C. J., Akentjew, T. L., Alverio, J., Khoury, M., & Acevedo, J. P. (2016). Layer-by-layer approach for a uniformed fabrication of a cell patterned vessel-like construct. *Biofabrication*, *9*(1), 15001. https://doi.org/10.1088/1758-5090/9/1/015001

Wu, K. S., Van Osdol, W. W., & Dauskardt, R. H. (2006). Mechanical properties of human stratum corneum: Effects of temperature, hydration, and chemical treatment. *Biomaterials*, *27*(5), 785–795. https://doi.org/10.1016/j.biomaterials.2005.06.019

Xu, Z., Chen, X., Tan, R., She, Z., Chen, Z., & Xia, Z. (2019). Preparation and characterization of a gallium-loaded antimicrobial artificial dermal scaffold. *Materials Science and Engineering C*, *105*(August). https://doi.org/10.1016/j.msec.2019.110063

Yang, F., Cohen, R. N., & Brey, E. M. (2020). Optimization of co-culture conditions for a human vascularized adipose tissue model. *Bioengineering*, *7*(3), 1–18. https://doi.org/10.3390/bioengineering7030114

Yao, R., Du, Y., Zhang, R., Lin, F., & Luan, J. (2013). A biomimetic physiological model for human adipose tissue by adipocytes and endothelial cell cocultures with spatially controlled distribution. *Biomedical Materials (Bristol,*

England), *8*, 45005. https://doi.org/10.1088/1748-6041/8/4/045005

Yi, X., Liu, J., Wu, P., Gong, Y., Xu, X., & Li, W. (2020). The key microRNA on lipid droplet formation during adipogenesis from human mesenchymal stem cells. *Journal of Cellular Physiology*, *235*(1), 328–338. https://doi.org/10.1002/jcp.28972

Yoshimura, K., Shigeura, T., Matsumoto, D., Sato, T., Takaki, Y., Aiba-Kojima, E., Sato, K., Inoue, K., Nagase, T., Koshima, I., & Gonda, K. (2006). Characterization of freshly isolated and cultured cells derived from the fatty and fluid portions of liposuction aspirates. *Journal of Cellular Physiology*, *208*(1), 64–76. https://doi.org/10.1002/jcp.20636

Young, P., Boussadia, O., Halfter, H., Grose, R., Berger, P., Leone, D. P., Robenek, H., Charnay, P., Kemler, R., & Suter, U. (2003). E-cadherin controls adherens junctions in the epidermis and the renewal of hair follicles. *EMBO Journal*, *22*(21), 5723–5733. https://doi.org/10.1093/emboj/cdg560

Yue, K., Trujillo-de Santiago, G., Alvarez, M. M., Tamayol, A., Annabi, N., & Khademhosseini, A. (2015). Synthesis, properties, and biomedical applications of gelatin methacryloyl (GelMA) hydrogels. *Biomaterials*, *73*, 254–271. https://doi.org/10.1016/j.biomaterials.2015.08.045

Zhang, K., Fu, Q., Yoo, J., Chen, X., Chandra, P., Mo, X., Song, L., Atala, A., & Zhao, W. (2017). 3D bioprinting of urethra with PCL/PLCL blend and dual autologous cells in fibrin hydrogel: An in vitro evaluation of biomimetic mechanical property and cell growth environment. *Acta Biomaterialia*, *50*, 154–164. https://doi.org/10.1016/j.actbio.2016.12.008

Zhang, T., Lin, S., Shao, X., Shi, S., Zhang, Q., Xue, C., Lin, Y., Zhu, B., & Cai, X. (2018). Regulating osteogenesis and adipogenesis in adipose-derived stem cells by controlling underlying substrate stiffness. *Journal of Cellular Physiology*, *233*(4), 3418–3428. https://doi.org/https://doi.org/10.1002/jcp.26193

Zhang, Y., Enhejirigala, Yao, B., Li, Z., Song, W., Li, J., Zhu, D., Wang, Y., Duan, X., Yuan, X., Huang, S., & Fu, X. (2021). Using bioprinting and spheroid culture to create a skin model with sweat glands and hair follicles. *Burns & Trauma*, *9*, 1–13. https://doi.org/10.1093/burnst/tkab013

Zhu, W., Qu, X., Zhu, J., Ma, X., Patel, S., Liu, J., Wang, P., Lai, C. S. E., Gou, M., Xu, Y., Zhang, K., & Chen, S. (2017). Direct 3D bioprinting of prevascularized tissue constructs with complex microarchitecture. *Biomaterials*, *124*, 106–115. https://doi.org/10.1016/j.biomaterials.2017.01.042

Zsikó, S., Csányi, E., Kovács, A., Budai-Szűcs, M., Gácsi, A., & Berkó, S. (2019). Methods to evaluate skin penetration in vitro. *Scientia Pharmaceutica*, *87*(3). https://doi.org/10.3390/scipharm87030019

APPENDICES

A. Ethical Statement

This study was approved by the Middle East Technical University Human Experiments Local Ethics Committee approval code 2018-FEN-052 (No:28620816/491). Written consent to participate in the study and publication was obtained from the adult female Caucasian patient undergoing elective plastic surgery procedure at Medicana International Hospital Ankara, Turkey, by Prof. Dr. Muharrem Demiroğulları and handled according to the Declaration of Helsinki Principles. Skin samples were obtained from 3 female otherwise healthy donors ages 40-65 who were admitted for elective breast surgery and processed to obtain primary human keratinocytes.

UYGULAMALI ETİK ARAŞTIRMA MERKEZİ
APPLIED ETHICS RESEARCH CENTER

ORTA DOĞU TEKNİK ÜNİVERSİTESİ
MIDDLE EAST TECHNICAL UNIVERSITY

DUMLUPINAR BULVARI 06800
ÇANKAYA ANKARA/TURKEY
T: +90 312 210 22 91
F: +90 312 210 79 59
uegam@metu.edu.tr

Sayı: 28620816 / 491

08 EKİM 2018

Konu: Değerlendirme Sonucu

Gönderen: ODTÜ İnsan Araştırmaları Etik Kurulu (İAEK)

İlgi: İnsan Araştırmaları Etik Kurulu Başvurusu

Sayın Prof.Dr. Ayşen TEZCANER

Danışmanlığını yaptığınız yüksek lisans öğrencisi Funda CAN'ın **"36 Boyutlu Yazıcı ve Mikroakışkan Cihaz Kullanılarak Çok Katlı Deri Modeli Geliştirilmesi"** başlıklı araştırmanız İnsan Araştırmaları Etik Kurulu tarafından uygun görülerek gerekli onay **2018-FEN-052** protokol numarası ile **08.10.2018 - 31.10.2020** tarihleri arasında geçerli olmak üzere verilmiştir.

Bilgilerinize saygılarımla sunarım.

Prof. Dr. Ş. Halil TURAN
Başkan V

Prof. Dr. Ayhan SOL
Üye

Prof. Dr. Ayhan Gürbüz DEMİR
Üye

Doç. Dr. Yaşar KONDAKÇI
Üye

Doç. Dr. Zana ÇITAK
Üye

Doç. Dr. Emre SELÇUK
Üye

Dr. Öğr. Üyesi Pınar KAYGAN
Üye